Investigation into soft body impact on laminated composites

Submitted in partial fulfilment of the
requirements of the degree of

DOCTOR OF PHILOSOPHY

KAVITHA MOL S.

Register No. DTKM18JAN008

Supervisor

Dr. Sadiq A

Professor

Department of Mechanical Engineering

TKM College Of Engineering

APJ ABDUL KALAM TECHNOLOGICAL UNIVERSITY

Thiruvananthapuram (2022)

A DECLARATION OF ACADEMIC HONESTY AND INTEGRITY

I declare that this written submission represents my ideas in my own words and where others' ideas or words have been included, I have adequately cited and referenced the original sources. I also declare that I have adhered to all principles of academic honesty and integrity and have not misrepresented or fabricated or falsified any idea/data/fact/source in my submission. I understand that any violation of the above will be cause for disciplinary action by the University and can also evoke penal action from the sources which have thus not been properly cited or from whom proper permissions have not been taken when needed.

(Signature)

(Dr. Sadiq A.)

KAVITHA MOL S

(Name of the student)

DTKM18JAN008

(Reg No.)

Date: 01/09/2022

CERTIFICATE OF SUPERVISOR

It is certified that the work contained in the thesis titled "Investigation into soft body impact on laminated composites," by "KAVITHA MOL S.," has been carried out under my supervision and that this work has not been submitted elsewhere for a degree.

Signature of the supervisor

Name: Dr. Sadiq A.

Designation: Professor

College: TKM College Of Engineering

Date: 01/09/2022

Place: Karicode

ACKNOWLEDGMENT

I wish to record my indebtedness and thankfulness to all who helped me to prepare this thesis report titled “Investigation into soft body impact on laminated composites” and present it in a satisfactory way.

I am particularly grateful to my research supervisor, Dr. Sadiq A. (Professor, Department of Mechanical Engineering), for his valuable advices and essential inputs throughout the course of the research work.

I am grateful to Dr. V. L. Satheesh (Principal Scientist, National Aerospace Laboratories, Bangalore) and Dr. Mubarak Ali (Asst. Prof, TKMCE) for their wholehearted support during the periodic review of the research work. I am also thankful for Dr. Stanley C Salem, Assistant professor, CMR university, Bangalore for the support and suggestions for the research.

I would also like to thank Prof. Dr. A Salih (Chairman of DC), K.C. Gopalakrishnan, Dr. N.R. Rajesh (External DC Members), Prof. Dr. V.N. Ajukumar and Prof. Dr. K.E. Reby Roy (Internal DC Members), for their encouragement and valuable advices on completing the research.

I am very much thankful to Dr. T. A. Shahul Hameed (The Principal), Dr. P. N. Dileep (Professor & Head of the Department of Mechanical Engineering), and other faculty members of TKMCE for their support in various stages in completing the research work.

I also take this opportunity to acknowledge my gratitude to my family members for encouragement for completing the research work.

I would like to praise and thank God, the Almighty, who has granted countless blessings and knowledge, so that I have been able to accomplish the research.

KAVITHA MOL S

(Reg. No. DTKM18JAN008)

Department of Mechanical Engineering

TKM College Of Engineering

Abstract

The impact of soft bodies such as birds on aircraft structures is a significant threat that leads to serious structural damage and economic loss to the aircraft industry. The leading edges are the foreparts of the aircraft and are always under the possibility of a bird strike. Leading edges are typically fabricated with GLARE laminate, tailored with alternatively arranged aluminium alloy and glass fibre epoxy layers. The approach followed in designing the leading edge is to design it to have a higher energy absorption capacity, thereby transferring less force to the supporting structure. Moreover, the deformation of the leading edge also to be reduced to protect its internal components. The present research aims to improve the bird impact resistance of fibre metal laminates used to fabricate the leading edges. This research is conducted in two parts; the first part is the optimization of the aluminium alloy parameters of the leading edge skin subjected to bird impact. The second part is the analysis of the strength and damage characteristics of different GLARE laminates under soft body impact. For this research, different bird modelling approaches are analysed to establish a soft body model consistent with theoretical and experimental predictions of actual bird strike events. The SPH soft body model with Mie-Grüneisen equation of state parameters exhibited a good correlation with an experimental test based on deformation patterns and pressure distribution characteristics. Then, the soft body impact simulation on the aluminium alloy (AA 2024-T3) wing leading edge is validated with a bird impact experimental test. Soft body impact simulations showed that the material parameters which influence the energy absorbing characterises of aluminium alloys are static yield limit, elastic modulus, strain hardening modulus and hardening exponent. The selected material parameters are optimized and validated with soft body impact analysis on the wing leading edge using Taguchi's L16 design of experiments with grey relational analysis. Quasi-static tension test simulations demonstrate that the mechanical properties of the optimized aluminium alloy are increased 20.84% yield strength, 20% tensile strength, and 25% deformation energy compared to AA 2024-T3. The tension test simulations on different GLARE laminates tailored with optimized aluminium alloy showed an average improvement of 20.87% aluminium alloy yield strength and 20.22% matrix failure strength compared to GLARE laminates tailored with AA 2024-T3. Observations of the soft body impact analysis concluded that the GLARE laminate with the glass/epoxy layers arranged between thinner aluminium alloy layers is most suitable for designing the leading edges.

Table of contents

List of figures

List of tables

Abbreviations

AA	Aluminium alloy
ALE	Arbitrary Lagrangian-Eulerian
DoE	Design of Experiments
EASA	European Aviation Safety Agency
EOS	Equation of State
FAA	Federal Aviation Administration
FAR	Federal Aviation Regulations
FML	Fibre Metal Laminate
GLARE	Glass Aluminium Reinforced Epoxy
GRG	Grey Relational Grade
HT	Horizontal Tail
LAG	Lagrangian
OA	Orthogonal Array
RAE	Royal Aircraft Establishment
RF	Reaction force
SPH	Smooth Particles Hydrodynamics
US	United States
VC	Crucial Velocity

VT	Vertical Tail

Notations

A	Static yield limit of the aluminium alloy
a	First-order volume correction coefficient
B	Strain hardening modulus of the aluminium alloy
C	Strain rate hardening coefficient of aluminium alloy
$[C]$	Elasticity matrix
$[C_d]$	Damaged elasticity matrix
c_0	Velocity of sound in the material
D	Overall damage variable
d_m	Current state of matrix damage
d_f	Current state of fibre damage
d_s	Current state of shear damage
E	Elastic modulus of the aluminium alloy
E_1	Elastic modulus of the composite along fibre axis
E_2	Elastic modulus of the composite transverse to fibre axis
E_H	Internal energy at Hugoniot shock
E_m	Specific internal energy
E_{ref}	Energy level of the reference state represented by P-V curve

G_f Fracture energy of the aluminium alloy

G_{1c} Longitudinal compressive fracture energy for glass fibre epoxy

G_{1t} Longitudinal tensile fracture energy for glass fibre epoxy

G_{2c} Transverse compressive fracture energy for glass fibre epoxy

G_{2t} Transverse tensile fracture energy for glass fibre-epoxy

G_{12} Shear modulus of the glass fibre epoxy in fibre–matrix direction

G_{23} Shear modulus of the glass fibre epoxy in matrix–matrix direction

G_{Ic} Normal fracture energy for the epoxy layer

G_{IIc} First shear fracture energy for the epoxy layer

G_{IIIc} Second shear fracture energy for the epoxy layer

K_{ii} Coefficients of stiffness for the epoxy layer

L_0 Length of the soft body projectile

M Mass of the soft body material

m Temperature softening coefficient of the aluminium alloy

n Hardening exponent of aluminium alloy

P Particle pressure of the soft body material

P_H Hugoniot pressure of the soft body on the target

P_n Non dimensional pressure of the soft body on the target

p_s Stagnation pressure of the soft body on the target

p_{ref} Pressure level reference state represented by P-V curve

P_1 Pressure of the soft body material before shock

P_2 Pressure of the soft body material after shock

r Leading edge nose radius

S^L In plane shear strength at the ply plane

S^T Out of plane shear strength at the ply plane

s Slope of u_s-u_p curve

T Temperature

T_t Test temperature of aluminium alloy

T_0 Time duration for complete impact

T_m Melting temperature of aluminium alloy

T_r Reference temperature of aluminium alloy

$\overset{*}{T}$ Homologous temperature

t Step time

t_i Traction vectors of epoxy layer

t_n Normalised time of soft body impact

t_o Initial time of impact

t_n^0 Quadric traction in normal direction for epoxy layer

t_s^0 Quadric traction in shear direction for epoxy layer

t_t^0 Quadric traction in transverse direction for epoxy layer

$\overline{u}$ Equivalent plastic displacement

$\overline{u}_f$ Equivalent plastic displacement at fracture

u_p Particle velocity

u_s	Shock propagation velocity
u_0	Initial impact velocity of the soft body
V	Volume
V_p	Penetration velocity of the soft body
W	Weight of the soft body
X^t	Strength value parallel to the fibre under tension
X^c	Strength value parallel to the fibre under compression
Y^t	Strength value normal to the fibre under tension
Y^c	Strength value normal to the fiber under compression
z	Amount of porosity of the material
α	Sweep angle / impact angle
β	Benzeggagh and Kenane constant for epoxy layer
Γ	Grüneisen coefficient
Γ_0	Material Constant of soft body.
γ	Ratio of specific heat
γ_i	Grey relational grade
γ_m	Total mean grey relational grade
δ_i	Relative displacements at contact point for the epoxy layer
ε_f	Plastic strain at damage initiation of the aluminium alloy
ε_p	Effective plastic strain of the aluminium alloy
$\dot{\varepsilon}_e$	Effective plastic strain rate of the aluminium alloy

$\dot{\varepsilon}_0$ Reference plastic strain rate of the aluminium alloy

$\xi_i(k)$ Grey relational coefficient

ν Poisson's ratio of aluminium alloy

ν_{12} Poisson's ratio of composite material for the fibre-matrix direction

ρ Particle density of the soft body material

ρ_{air} Density of air

ρ_f Full density of the soft body material (without porosity)

ρ_0 Reference density

ρ_1 Density of the soft body material before shock

ρ_2 Density of the soft body material after shock

$\bar{\sigma}$ Flow stress of aluminium alloy

σ_{y0} Ultimate stress of aluminium alloy

$\hat{\sigma}_{ij}$ Effective stress tensor components

$\hat{\sigma}_{11}$ Component stress of the composite along the fibre direction

$\hat{\sigma}_{22}$ Component stress of the composite transverse to the fibre direction

$\hat{\sigma}_{12}$ Shear stress of the composite along the ply plane

τ Skin thickness of flat panel / curved panel of leading edge

Chapter 1

Introduction

Aircraft always fly with the risk of impacting foreign objects like hailstone, birds, runway debris, and tire fragments. The impact of soft bodies such as birds is a significant threat to aircraft structures, leading to severe structural damage and economic loss to the aircraft industry. The US department of agriculture and Federal Aviation Administration (FAA) jointly compiles a database of all reported wildlife strikes on US aircraft and foreign aircrafts experiencing strikes in the USA. According to a joint report of the Federal Aviation Administration and the US department of agriculture during the period 1990-2020 (FAA 2021), the number of reported wildlife impacts on the US civil aircraft increased from 1816 in 1990 to 11,473 in 2020. The estimated cost per annum of all wildlife impacts is 110,034 hours of aircraft downtime and $ 392 million in economic losses. This report showed that about 97% of all wildlife impacts are due to bird strikes, and 10,911 bird impact events have been recorded in 2020 alone. When analysing each bird strike event separately, the economic loss has been more than 1 million dollars in each case. Time out service takes 15 hours to 5 months based on the service requirements (FAA 2021). The estimated annual damage due to the bird strike cost the aviation industry over the US $1.2 billion each year (Allan 2006). Bird strike incidents occur especially critical during take-off and landing phases. It is observed from the statistical data that 70 % of the bird impacts occur during the take-off and landing of aircraft. Impact with a large bird at very high speeds can destroy an aircraft, and this issue is one reason for limiting maximum aeroplane speeds to 250 knots (464 km/h) at altitudes below 10,000 feet (3048 m) (Eschenfelder 2005). The front facing components wings, empennages, engines, nose/radome, fuselages, and windshields commonly experience significant damage from bird strikes. Thus, resistance to a bird strike is the primary design factor, and an aircraft must satisfy the standard regulations defined by different aviation authorities like FAA and EASA ,before its first service (Liu *et al.* 2019).

Soft body impact is a non-linear transient phenomenon; it is challenging to monitor experimentally, especially damage initiation and propagation in the fibre metal laminates. Significant challenges for bird strike simulation on fibre metal laminates are bird modelling, bird-target interface modelling, and fibre metal laminate failure modelling. Finite element simulations of these impact events help reduce the time and cost to optimize the design before a full-scale certification test. Many researchers use finite element packages such as Pam-Crash, LS-DYNA, Radioss, MSC-Dytran, and ABAQUS/Explicit to simulate bird strikes (Johnson and Holzapfel (2003); McCarthy *et al.* (2004); Airoldi and Cacchione (2006); Chuan (2006); Jenq *et al.* (2007); Mao *et al.*(2008); Lavoie *et al.* (2009); Smojver *et al.* (2011); Smojver and Ivancevic (2011); Nishikawa *et al.* (2011)). The capacity of the packages to predict bird strikes has been well documented in the literature. The ability of ABAQUS/Explicit to excellently handle severely nonlinear behaviour formulates it highly attractive for the simulation of high-speed events. ABAQUS/Explicit is selected for this study because it also has the option to define parametric studies via python scripts. The software also provides efficient damage models for metallic and composite materials.

Fig 1.1 Aircraft leading edge struck by bird
(Picture taken from http://www.birdstrike.it/en/index.php?Archive_2011)

The primary aircraft components need different material properties for the optimum and reliable design based on its particular loading requirements. The leading edges of wing and empennage structures are the foreparts of the aircraft and are always under the possibility of a bird strike. **Fig 1.1** shows image of the aircraft leading edge being struck by

a bird. Leading edges are typically fabricated with Glass Aluminium Reinforced Epoxy (GLARE) laminate, tailored with alternatively arranged Aluminium Alloy (AA) and glass fibre epoxy layers. The load transferred to the supporting structures during bird impact is critical for the safe flight of the aircraft. Hence, the approach followed in the design of the leading edge for bird impacts is to design it to have a higher energy absorption capacity, thereby transferring less forces to the support structure (such as the spar). Moreover, deformation of the leading edge due to bird impact must be reduced to protect internal wing components.

The skin of the leading edge is the most critical part of the wing structure as it has a higher chance of getting affected by the impact. Therefore, the skin material must have the property to absorb a significant portion of the incident impact energy, thereby transferring a lesser load to the supporting structures. The mechanical properties like strength, toughness, fatigue crack initiation resistance, crack growth rate resistance and corrosion resistance are all important for materials considered for leading edge skins. The aluminium–copper (2xxx series) alloys are the primary alloys utilized to fabricate aircraft leading edges where the key design principle is damage tolerance. The 2xxx series alloys including magnesium have advanced strength due to the precipitation of Al2Cu and Al2CuMg phases. It has higher damage tolerance and better fatigue crack growth resistance than other AA series alloys. 2024 -T3 is a good variant of the Al-Cu-Mg alloy commonly used as a skin material for aircraft-leading edges. AA 2024 has moderate yield strength, damage tolerance and tensile toughness in the T3-aged condition. The moderate yield strength and tensile toughness limit the application of this alloy in high-stress areas which anticipate high-speed bird strikes. Therefore, one objective of this research is to develop a 2xxx series aluminium alloy, which outperforms its 2024 counterpart when processed into the leading-edge skins of wings and empennage structures. The intensive research of microstructural effects on the mechanical properties of these alloys continually manufactured new alloys. To develop a new alloy or improve the properties of the present alloy used for a particular aircraft part, it needs to define the property requirements based on the different loading conditions (Dursun and Soutis 2014).

The ultimate load experienced by the wing leading edge is considered to be due to bird strike. Therefore, the design requirements of wing leading edges are as per safety regulations against bird impact loading. The properties required to meet the design requirements can be obtained by optimizing the alloy compositions and processing

conditions (Pantelakis and Alexopoulos 2006). Aircraft designers also aim to reduce the number of parts while increasing the energy absorption capacity of the material (Starke and Staley 1999) Therefore, an aircraft structural designer must work together with a material producer to tailor the mechanical properties of the metallic alloys as per the specific requirements. The chemical composition and mechanical properties of AA 2024-T3 are given in **Table 1.1** and **Table 1.2** respectively

Table 1.1 chemical composition of AA 2024-T3 (Leseur 1999)

Cu (wt.%)	Mg (wt.%)	Mn (wt.%)	Zr (wt.%)	Fe (wt.%)	Si (wt.%)	Ti (wt.%)	Al
3.87	1.3	0.6	0.1	0.02	0.03	0.002	balance

Table 1.2 Mechanical properties of AA 2024-T3 (LeSuer 1999)

Yield strength (MPa)		Ultimate tensile strength		Elongation (%)	
Minimum	Maximum	Minimum	Maximum	Minimum	Maximum
327	330	474	477	16	18.2

For certain load requirements, the researchers investigated ways to improve the material properties through various processing conditions. In the current scenario, the developments in modelling and analysis have transferred from macro to microsystems so as to simulate and analyse the smallest feasible features of real-time problems. The detailed literature review concluded that developing new materials to meet the specific needs of aircraft components is the primary focus of airframe manufacturers and material producers. Defining the desired properties is necessary to create custom alloys for aircraft components that meet their specific loading conditions. In order to achieve this, first, it is required to convert these required mechanical properties into microstructural targets. These microstructural objectives then translated into compositional/process definitions. The current challenge is to develop an AA 2024-T3 alloy variant with improved structural properties for leading-edge applications to prevent bird strikes. The design studies showed that optimising the flow stress parameters efficiently enhances the mechanical properties of the aluminium alloys. Optimized material parameters can be achieved through alloying

and thermomechanical processing conditions. The schematic representation of the three different levels of modelling involved in the design of aerospace alloys is shown in **Fig 1.2.**

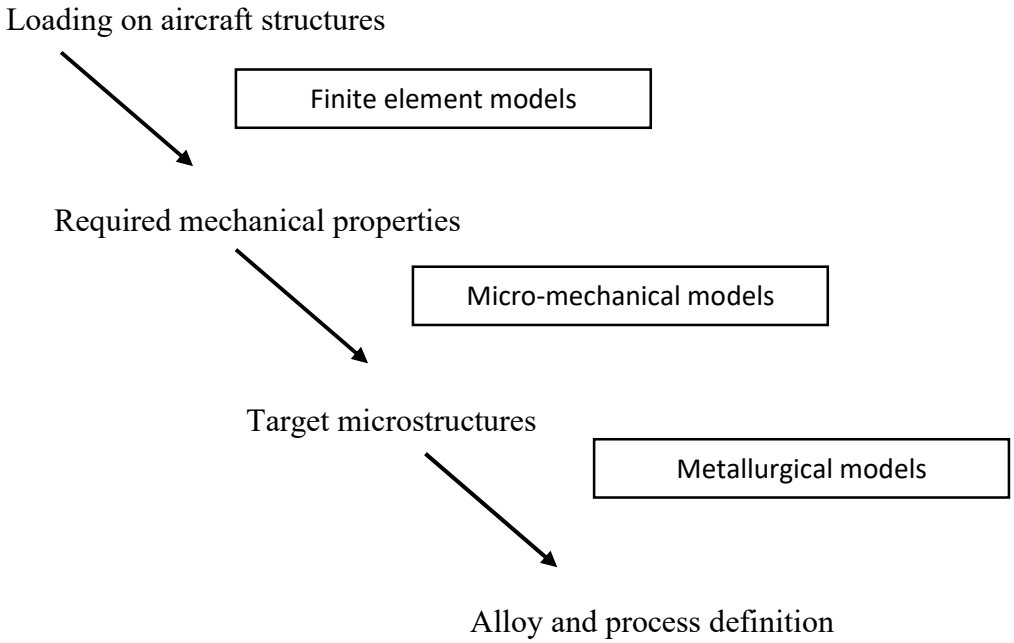

Fig 1.2 Depiction of the three different levels included in the design of aerospace alloys

The present study optimises the material parameters of AA 2xxx used in the wing leading edges with an aim to improve its mechanical properties against soft body impact. The identification of the effect of several target material parameters can be helpful for tailoring a leading edge based on Fibre Metal Laminate (FML) concept. From the detailed literature review of the bird strike studies and considering the future research possibilities, it can be concluded that the response of fibre metal laminates to bird impact involves many parameters like type of metal, metal thickness, fibre properties, matrix properties, stacking sequence, fibre orientation, *etc.* Therefore, optimizing any of these parameters using some Design of Experiment (DoE) methods can help improve the performance of the FML for specific loading requirements such as bird impact.

The current research is carried out to improve the bird impact resistance of GLARE laminates used for the leading edges of aircrafts. This work is conducted in two parts; the first part is the optimization of the aluminium alloy parameters of the wing leading edge

skin subjected to bird impact. The second part is the analysis of the impact response and damage behaviours of different GLARE laminates under soft body impact loading.

1.1 Certification requirements

Bird impact is a severe and destructive event and it must be taken into account when designing flight-critical aircraft components. Therefore, crashworthiness or airworthiness regulations such as the FAA and EASA define bird strike regulations for large civil aircraft in accordance with FAR 25 or CS 25. Jetliners typically cruise at about 35,000 feet (10000m) at speeds over 500 miles per hour (224 m/s). The commercial aircraft operate at speeds above 240 knots and above. The bird impact damage at such a high velocity means that more significant damage occurs to the part which is struck. Such impacts are sometimes catastrophic, resulting in emergency landings, and the loss of aircraft in the worst cases. Hence, the mass of the bird and the velocity defined in the certification clauses for qualifying the part for airworthiness are defined on the statistical data on the bird strike accidents, the mass of the birds flying at higher altitudes, the altitudes corresponding to the strikes, and the extent of damages induced. The certification clauses demand that the aircraft be capable to successfully land after a standard bird impacted on the leading edges at a certain velocity of concern, which is defined based on the cruise velocity of the aircraft. The quality of the bird in certification requirements varies by the site.

Bird strike rules are described in CS-25 and FAR 25, these two certification requirements are almost similar, except that CS-25 uses a 4-pound bird in its section 631. The certification requirements for leading edges of the wing and empennage structures for the airplane under consideration in this research are FAR 25.571 and 25.631, respectively.

The certification requirements for the leading edges of the wing for the aircraft are standing on regulations FAR 25.571 under FAA (FAA 2017). FAR Part Section 25.571 (Damage – tolerance and fatigue evaluation of structure) mentioned that

"*The airplane must be able to successfully complete a flight in case any structural damage takes place as a result of impact with a 4-pound bird when the velocity of the airplane relative to the bird along the flight path of the airplane is equal to VC at sea level or 0.85 VC at 8000 ft, whichever is more critical".*

The FAA Federal Aviation Regulations (FARS, 14 CFR) Section 25.631 (Bird strike damage) states that

‘‘*The empennage structure must be designed to assure capability of continued safe flight and landing of the airplane after impact with an 8-pound bird when the velocity of the airplane (relative to the bird along the airplane’s flight path) is equal to cruise velocity (VC) at sea level*”.

The damaged structure must capable to bear the static loads (ultimate loads) which are fairly anticipated to happen on the flight. Dynamic effects on these static loads do not require to take into consideration. If significant changes in structural stiffness or geometry, or both, follow from structural failure or partial failure, the effect on damage tolerance must be further investigated. (FAA 2017).

1.2 Motivation of the study

The damage to aircraft structures due to bird impacts have attracted the attention of researchers for many years. Therefore, the development of materials with better bird impact resistance is recognized as a relevant field of investigation. Generally, bird is considered as soft bodies in impact kind researches. Soft bodies are highly deformable during impact, and it thus complex to simulate an impact event with a soft body that closely matches the behaviour of the actual bird impact event. The soft body models are usually validated by comparing the pressure distribution characteristics, obtained by simulating the impact of the soft body on a rigid target, with equivalent values from the experiment test. Many researchers (Airoldi and Cacchione 2006; Johnson and Holzapfel 2003; Jenq *et al.* 2007; Mao *et al.* 2008; Lavoie *et al.* 2009; Smojver and Ivancevic 2011; McCarthy *et al.* 2004; Chuan 2006) have modelled soft body and validated it for the impact. However, the numerical values of different studies vary based on the selected material models and modelling approaches. The available soft body models have not exhibited much correlation with the experiment test in the Hugoniot (initial peak) and stagnation (steady-state) pressure values, which is required for validation. Therefore, the present research studies different soft body material models (Mie-Grüneisen equation of state material model, Mie-Grüneisen equation of state for multi material models, user-defined equation of state) and then analyses different bird modelling approaches (Lagrangian (LAG), Arbitrary Lagrangian-Eulerian (ALE), Smooth Particles Hydrodynamics (SPH)) to establish a soft

body model that converges with theoretical and experimental predictions of actual bird impact events.

Many researchers have studied the response and failure of the leading edge of the wing under soft body impact (McCarthy *et al.* 2004; Kermandis *et al.* 2005; Georgiadis *et al.* 2008; Guida *et al.* 2009; Reglero *et al.* 2011; Stanley *et al.* 2011; Pahang and Abolbashari 2016; Yu *et al.* 2020). However, there is no sufficient research report on the design of the materials for wing leading edges based on material parametric studies considering the impact event. The skin of the leading edge is the most critical part of the wing structure as it has a higher chance of getting affected by the impact. Therefore, the skin material must have the property to absorb a significant portion of the incident impact energy, thereby transferring lesser load to the supporting structures. Moreover, the deformation of the leading edge due to bird impact must also be reduced to protect internal components of the wing. The present study optimizes the material parameters of AA 2xxx used in the wing leading edges with an aim to improve its mechanical properties against soft body impact. The identification of the effect of various target material parameters can be helpful for tailoring a leading-edge with fibre metal laminates.

The studies to improve the properties of GLARE laminate have been reported in account of its greater impact and fatigue properties compared to other substitutes of equal areal density (Fatt *et al.* 1970). Research on the effects of high and low-velocity rigid body impact on fibre metal laminates is enormous. However, little research has been reported on the impact of soft bodies on fibre metal laminates. More than that, investigations have not been reported on the impact response and damage behaviour of different GLARE laminates for the soft body impact. The current research intends to analyse the influence of metal thickness and stacking sequences on soft body impact response and damage behaviour of GLARE laminates.

1.3 Objectives of the research

The broad objective of the research is to improve the mechanical properties of the fibre metal laminate considered for the wing leading edges of aircraft structures to effectively resist damage from bird impacts.

The specific objectives of the study are:

1. Analyse the different bird modelling approaches to develop a soft body model considering the reported theoretical and experimental results of actual bird impact events.
2. Simulate the soft body impact on aluminium alloy (AA 2024-T3) wing leading edge. Then, validate the simulation with the results of soft body impact experiment test conducted on the aluminium alloy (AA 2024-T3) wing leading edge specimen.
3. Carry out soft body impact simulations on leading edges (Horizontal Tail (HT), Vertical Tail (VT), wing) by varying selected material parameters. Then, identify the important material parameters that influence the energy absorption properties of the material by analysing the centre displacement and reaction force of the leading edges.
4. Carry out multi-objective optimization with selected material parameters of the 2xxx series aluminium alloy using Taguchi's L16 design of experiments with grey relational analysis. Analyse the results to find the optimum combination of material parameters for simultaneous reduction of reaction force and centre displacement of the wing leading edge.
5. Analyse the performance improvement of the optimized aluminium alloy with a series of quasi-static tension test simulations. Compare the mechanical properties (yield strength, ultimate tensile strength and deformation energy) of the optimized aluminium alloy with simulation and reported experimental test on conventional aluminium alloy, AA 2024-T3.
6. Conduct a failure analysis on the optimized aluminium alloy specimen to determine its damage initiation and evolution parameters.
7. Carry out a series of tension test simulations on different GLARE laminates to compare the mechanical property enhancement of the GLARE laminates tailored with optimized AA over GLARE laminates tailored with AA 2024-T3.
8. Perform soft body impact simulations on different GLARE laminates to evaluate their impact response and damage behaviours.

1.4 Scope of the research

The research aims to improve the mechanical properties of the GLARE laminates used for wing leading edges against soft body impact. As the experiments tests are highly expensive, finite element simulations are considered as a strong tool for this evaluation. To

select a soft body model suitable for a parametric study, analyse different modelling methods (LAG, ALE and SPH) for soft body models using the finite element software ABAQUS/Explicit. Create aluminium alloy (AA 2024-T3) leading edge models (HT, VT and wing) using the finite element software Altair ®Hyper mesh®. Validate the soft body impact simulation on an aluminium alloy (AA 2024-T3) wing leading edge with an experimental test carried out at Gas Turbine Research Establishment (GTRE), Bangalore. After the validation, prepare a parametric study test matrix by varying material parameters: elastic modulus, static yield limit, strain hardening modulus, strain hardening exponent and Poisson's ratio. Develop Python scripting algorithms based on the parametric study test matrix to automate repetitive tasks. Then, perform soft body impact simulations on the leading edges by varying the considered material parameters. Compare the parametric study test results based on the reaction force (***RF***) and the central node displacement (***U***) of the leading edges with varied material combinations. Explore Taguchi's Design of experiments (DoE) combined with grey relational analysis available in statistical software Minitab®. Carry out a multi-objective optimization analysis on the selected material parameter combinations for the simultaneous reduction of reaction force and centre displacement. According to standard E8/E8M-11, create tension specimen models of aluminium alloys of different thicknesses. Then, carry out quasi-static tension test simulations on these specimens (optimized aluminium alloy and AA 2024-T3) of varying thickness (0.2 to 0.6 mm) using the finite element software ABAQUS/Explicit. Analyse the performance improvement of the optimized aluminium alloy by comparing the mechanical properties, *i.e.,* yield strength, ultimate tensile strength, and tensile toughness with aluminium alloy (AA 2024-T3). Carry out the failure analysis on the 2 mm thick optimized aluminium alloy specimen and find out the ductile damage variables (stress triaxiality, strain rate, failure strain and fracture energy) from the results. Conduct tension test simulations on GLARE laminates tailored with optimized aluminium alloy layers and S2 glass/LY 566 epoxy layers. The performance of the GLARE laminates is compared based on the stress point at the onset of damage (aluminium yield, matrix failure, fibre failure) to verify their superiority over GLARE laminates tailored with AA 2024-T3. Then, perform soft-body impact simulations on GLARE laminates with different metal thickness and stacking sequences (GLARE 5-2/1-0.2, GLARE 3-3/2-0.2, GLARE 5-2/1-0.4, GLARE, 5-2/1-0.6). Compare results regarding reaction forces, deflection, damage dissipation energy, matrix failure, fibre failure and delamination.

1.5 Conceptual frame work and methodology

The approach followed to perform this research according to the conceptual framework is shown in **Fig 1.3.** A detailed literature survey helped to study suitable approaches to implement in the current research and to identify the current status of the research about soft body impact on various aircraft structures. And it also helped to identify the research gap and the problem formulation of the work.

The finite element software ABAQUS/Explicit provides efficient methods for bird strike simulation, such as contact interface modelling, bird modelling, fibre metal laminate modelling, and more. This software also has the option to define parametric studies via python scripts. It provides efficient damage models for metallic and composite materials. Since ABAQUS is identified as an efficient tool for bird strike simulation, a study is carried out to get familiarized with the pre-processing and post-processing module of the software.

The first phase of the research is to identify the certification requirements mentioned by various aviation administrations (FAA and EASA) on different aircraft components. The technical reports compiled by Federal Aviation Administration (FAA) has assessed the bird impact damage and its consequences to the aircraft industry. As per certification requirements, the mass of the bird, impact velocity and impact angle, *etc*., are selected for soft body impact on the aircraft component under consideration. This study used the formula introduced by Royal Aircraft Establishment (RAE) to calculate the thickness of the leading edge for the class of aircraft under consideration.

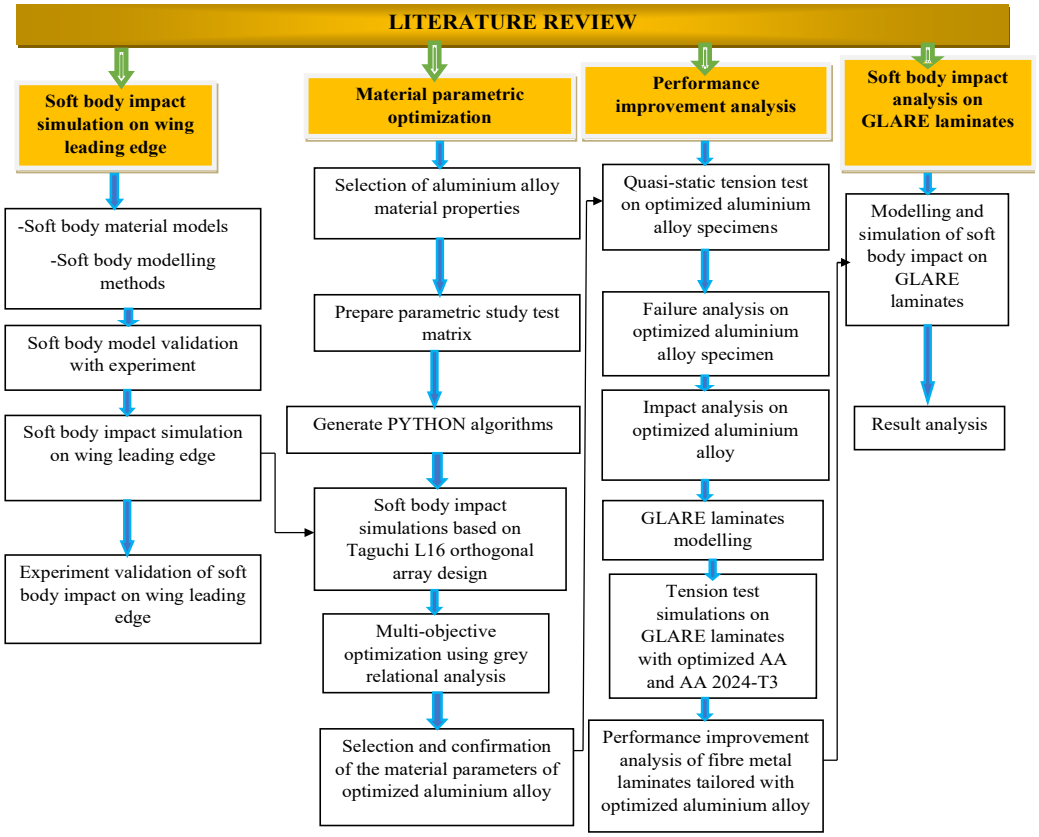

Fig 1.3 Conceptual framework

The following research phase is to establish a soft body model that exhibits actual the bird impact behaviour characteristics. For this, different soft body material models, geometric models, finite element methods, bird interface modelling methods, and experimental tests are studied from published articles, books, research thesis, analysis user manuals, and technical notes. This study has observed that researchers (Airoldi and Cacchione 2006; Johnson and Holzapfel 2003; Jenq *et al.* 2007; Mao *et al.* 2008; Lavoie *et al.* 2009; Smojver and Ivancevic 2011; McCarthy *et al.* 2004; Chuan 2006) have used different geometric models, material models, and finite element approaches for developing the soft body model. They used different geometric models, *i.e.,* cylinder, ellipsoid, sphere, hemispherical cylinder and even an actual mallard bird model, to model the soft body. It is understood that a hemispherical cylinder with a length to diameter ratio of two is universally accepted to model a soft body and selected for the current research. The material models used to define the soft body are different in the studies done by different authors. The researchers consider that soft body motion is similar to elastoplastic or hydrodynamic fluid flow. They used different equation of state material models to define the soft body, whose material behaviour is nearly equal to that of water. The soft body models are usually

validated by the comparison of pressure profile obtained by impacting the soft body on a rigid target, with equivalent values from the experimental test. The literature survey observed that the numerical values obtained in different studies have vast differences based on the selected material models and modelling approaches. The available soft body models have not exhibited much correlation with the experiment test in the Hugoniot (initial peak) and stagnation (steady-state) pressure values. Therefore, the present research has studied different soft body material models (Mie-Grüneisen equation of state, Mie-Grüneisen equation of state for multi-material models, user-defined equation of state). Then analysed different bird modelling approaches (Lagrangian (LAG), Arbitrary Lagrangian-Eulerian (ALE), Smooth Particles Hydrodynamics (SPH)) to establish a soft body model that converges with theoretical and experimental predictions of actual bird impact events. The results are compared based on the set-up time, run time, deformation pattern and pressure distribution characteristics.

The finite element models of leading-edge skin profiles (Wing, HT and VT) are created in finite element software Altair® Hyper Mesh®. Next, the simulation of soft body impact on the aluminium alloy wing leading edge is carried out in finite element software ABAQUS/Explicit. The bird strike test on the wing leading edge specimen has been conducted under actual bird strike conditions. The design and fabrication of the aluminium alloy (AA 2024-T3) wing leading edge has been carried out at NAL, Bangalore. The experimental test has been conducted at GTRE, Bangalore, with impacting a 4-pound (1.814 kg) bird substitute material (gelatine) with velocity 112 m/s on 2 mm aluminium alloy (AA 2024 -T3) wing leading edge. The soft body impact simulation is validated by comparing the deformation characteristics of leading edge with the bird impact experiment test.

Once confidence in the soft body model and the wing leading edge model are obtained, impact analyses are carried out on leading edges of wing and empennage structures by varying the aluminium alloy material parameters. For this, a detailed survey is done with different aluminium alloy material producers to study the different series of aluminium alloys and their properties, the range of values that can change with processing and alloying without compensating its mechanical properties like strength to weight ratio. The investigation found that the 2xxx series of aluminium alloys are typically used in leading edge skins as it has high failure strain than other alloys (Pantelakis and Alexopoulos 2006). It is heat treatable, and copper is its main alloying element. Its optimal strength qualities

are obtained not simply from composition alone but from the procedure by which it is heat treated. The elastic and flow stress parameters of aluminium alloy selected for the study are elastic modulus, Poisson's ratio, strain hardening modulus, static yield limit, and strain hardening exponent. Based on the study, a parametric study test matrix is written with the selected material parameters. Python scripting algorithms are generated to automate repetitive tasks in parametric studies for reducing the required pre-and post-processing time. The soft body impact simulations are conducted on the leading edges with many permutations and combinations of material parameters. Then, the reaction force of the leading edges and wing centre deformation are compared from the parametric study test results. The significant material parameters which affect the energy absorption characteristics of the wing leading edge are selected from the comparison of parametric study results. The range of material parameter values that can control the material properties based on the requirements is also selected from this analysis.

It is essential to reduce the reaction force and displacement of the leading edge together to improve the energy absorption capabilities of the leading edges. It helps support the spars and wing components from damage. Therefore, multi-objective optimization studies are required by changing selected control parameters. Taguchi's design of experiments combined with grey relational analysis is a powerful tool for multi-objective optimization. It is used to study several variables with a small number of experiments. Explored the statistical software Minitab® for creating a design matrix based on Taguchi's design of experiments and to learn grey relational analysis. Then, carried out sixteen soft body impact simulations on leading edges as per Taguchi's L16 Design of Experiments. The grey relational analysis is done for multi-objective optimization of material parameters based on selected control variables (***RF*** and ***U***). Analysis of variance also carried out to find the material parameters that have the greatest influence on the selected variables. Then, the selected parameters are optimized and validated with bird impact analysis on wing leading edges.

The mechanical improvement of the structures with optimized aluminium alloy is validated with a series of quasi-static tension test simulation and its comparison with experimental and simulation tests on conventional aluminium alloy, AA 2024-T3. Specimen geometry used for the tension test is as per the standards E8/E8M-11 and with different thicknesses of 0.2-0.6 mm. The stress-strain response of the optimized aluminium alloy is compared with a stress-strain response of AA 2024-T3 with the same geometry and

testing conditions. The optimized aluminium alloy exhibited the significant improvement in the mechanical properties *i.e.,* yield strength, ultimate tensile strength, and tensile toughness compared to AA 2024-T3. The effect of metal thickness on these mechanical properties also evaluated from the simulation results. The damage initiation and evolution parameters of the optimized aluminium alloy is found out from the failure analysis. An impact analysis also carried out on the aluminium alloy plates to study the behaviour of optimized aluminium alloy during bird impact.

The performance improvement of the different GLARE laminates tailored with optimized aluminium alloy is evaluated by tension test simulations. The finite element software ABAQUS is used to generate numerical simulations to discover the nonlinear tensile response behaviour of GLARE laminates. The finite element model of the GLARE laminates which is tailored with aluminium alloy (AA 2024-T3) and glass/epoxy prepreg layers is created. This GLARE laminate is validated with the experimental test from literature. Three finite element models with different metal thickness, stacking sequences and fibre orientations are correspondingly generated and compared with conventional GLARE laminates to estimate the damage and strength properties of the GLARE with optimized aluminium alloy. The performance of GLARE laminates is compared based on damage variables (*i.e.,* yielding of aluminium, matrix tension failure, fibre tension failure, and delamination).

In the next stage of the research, soft body impact simulations are carried out on GLARE laminates with different metal thickness and stacking sequences (GLARE 5-2/1-0.2, GLARE 3-3/2-0.2, GLARE 5-2/1-0.4, GLARE, 5-2/1-0.6) to evaluate their impact response and damage behaviour. The results are analysed regarding reaction forces, deflection, damage dissipation energy, matrix failure, fibre failure, and delamination.

Chapter 2

Review of literature

2.1 Introduction

The impact behaviour of fibre metal laminates is a relatively fast-growing field, with research papers mushrooming over the past three decades. However, little research has been done on the effect of soft bodies on fibre metal laminates. The survey roughly covers the related studies of bird impact on aircraft structures for the period from 1977 to 2021. These studies aim to reveal gradual changes in cognitive and research parameters in the research community during this developmental period. Of more than 60 papers found to cover soft body impact research, 36 research papers have been shortlisted and discussed here due to their content and relevance to current research.

2.2 Brief literature review

The earliest study of bird impact effects on aircraft structures was done by Wilbeck (1977). He tested various bird substitute materials, namely neoprene, RTV (room temperature vulcanized) rubber, porous RTV, gelatine, porous gelatine, chicken and beef, with normal and inclined impacts at different impacts velocities. It is explained that when the soft body hit the target an initial shock phase created followed with a steady flow phase. From this research, we get a detailed understanding of bird strike behaviour, bird substitute materials, impact force and its duration, pressure distribution characteristics, and more.

Ehrstroem and Warner (2000) explained that defining the required properties is necessary to create customized alloys for aircraft components that meet their specific loading conditions. Their research showed that flow stress parameters significantly influence the mechanical properties of materials. Their research also found that different treatments resulted in different yield stress values in several castings. Their study suggested

that the microstructural goals might be included in finite element simulation codes in the future, bypassing the global material parameters. Then, the behaviour of the structure and the material characteristics are directly correlated

Johnson and Holzapfel (2003) discussed the application of the finite element method in simulating the effect of soft bodies on composite shell structures. They implemented the composite layer damage mechanics model, and the intralayer delamination model. They have detailed different types of failure modes used to model impact on composite structures. The selection of failure criteria depends on the factors like mass, velocity and geometry of the soft body projectile, geometry of the target, type of fibre/ matrix used, and stacking sequence of fibres. They discussed different material modelling methods used in the numerical simulation of soft-body impact on composites. These damage models were then applied to composite materials to numerically simulate soft body impact on a glass fibre/epoxy cylindrical shell. They conducted an impact test on three different composite shell leading edge profiles with bovine hide gelatine (260 bloom) of diameter 30 mm, length 40 mm, mass 30-34 gm and three different velocities (132.5 m/s,142 m/s and 198 m/s). Then analysed the disintegration of the impactor, delamination, and fibre cracking of the target at different velocities.

Ubels *et al.* (2003) conducted an impact test with a 4-pound synthetic bird at velocities ranging from 80 to 100 m/s on three leading edge structures with an energy-absorbing tensor skin concept. The force diagrams showed that leading edge forces during impact do not cross the design limit of 200 kN.

McCarthy *et al.* (2004) described the material modelling method followed for predicting impact characteristics of GLARE using Pam-Crash/Shock. The model can capture the complex strain rate-dependent behaviour exhibited by these materials. The material model chosen to define the aluminium layer is the isotropic elastic-plastic thin shell model. A plastic algorithm defines the flow stress parameters of aluminium alloys. The damage model used to define the composite material is the Continuum Damage Mechanics (CDM) model. Their work demonstrates the importance of test data for high-strength glass composites for fibre-metal laminates at high strain rate conditions.

McCarthy *et al.* (2004) used the material modelling approach defined in their previous article to predict the bird strike properties of the GLARE laminate leading edge. The SPH (Smoothed Particle Hydrodynamics) method is used to simulate bird strikes. There is a good correlation between the finite element simulation and the experimental

results. Fastener failure was incorporated into the above model to accurately predict bird strike behaviour.

Kermandis *et al.* (2005) explored the concept of energy absorption by tensor skin concept in the design of soft body impact resistant leading edges. The tensor skin concept helps protect the leading edge from getting damaged to a great extent compared to normal leading-edge skin. The leading-edge skin based on the tensor skin concept was fabricated from tensor skin panels. When the soft body hits the leading edge, the folded layers unfold. Plies transfer the bird impact load to the ribs. The unfolding of the tensor skin successfully helped prevent penetration of the bird.

Wu and Yang (2005) studied the nonlinear stress-strain and fracture behaviour of fibre metal laminates under uniaxial loading. The material model of the fibre metal laminates is defined with modified classical lamination theory, which incorporates the flow stress behaviour of the aluminium alloy. A numerical simulation-based approach was used to predict the tensile response and deformation behaviour of GLARE laminates. The validated finite element model can be used to optimize the structure of the laminates. Optimization study includes fibre type, metal type, thickness, volume fraction, orientation, and properties of fibre metal laminates. The numerical model predictions are in good agreement with the experimental results.

Airoldi and Cacchione (2006) evaluated the accuracy of soft body finite element models by comparing pressure distribution characteristics with experimental tests. They performed a bird impact analysis on the finite element software Pam-Crash. The Lagrangian method was used to model the soft body impact analysis. They investigate the accuracy of models with various mesh sizes and present numerical results with refined mesh sizes. They recommended a range of modelling parameters for a numerical impact analysis of the aircraft structure.

Bethelo *et al.* (2006) developed a new light weight fibre metal laminate for aircraft components. The developed fibre metal laminate exhibited better damage tolerance than aluminium alloy and composite materials individually.

Chuan (2006) conducted a detailed study on the simulation of bird strike behaviour on aluminium panels and aircraft windshields. The reliability of the simplified Lagrangian soft body model is validated by comparing the pressure distribution characteristics with experimental result values of a real bird of equal mass normally impacting at a velocity of 116 m/s onto a flat rigid surface. The numerical results obtained showed good agreement in terms of pressure distribution and bird trajectories. Numerical Hugoniot and stagnation

pressures were 33% and 20% higher, respectively. The modelling of the bird strike using the LAG and SPH was then investigated by modelling impact on elastic aluminium sheets. Numerical results obtained from various formulations show close agreement, implying their suitability as alternatives in bird strike simulations. The effect of aircraft curvature windscreen on the impact response and the effective stress at the impact centre were also investigated.

Hou *et al.* (2006) tested a group of carbon fibre reinforced epoxy resin composite structures using a soft body impactor made of four parts water and one part bovine hide gelatine and ranked them according to their impact resistance. This research provides excellent information for selecting the optimal fibre and resin combination for better impact resistance.

Jenq *et al.* (2007) evaluated the soft body impact response on rigid plates using three different formulation approaches defined in LS-DYNA, *i.e.,* the Lagrangian, Eulerian and the Arbitrary Lagrangian Eulerian approaches. The material properties of the soft body were modelled to be similar to the properties of real bird characteristics. Based on the experimentally measured pressure distribution curves, the ALE method was found to be more accurate than LAG and EUL.

Georgiadis *et al.* (2008) developed an effective simulation method for the bird strike certification of the movable trailing edge (MTE) of the Boeing 787 Dreamliner. The explicit finite element code Pam-Crash is used for the simulation. Movable trailing edge was made of carbon fibre epoxy composite. The bird was modelled using SPH techniques. The modelling procedure followed in the analysis was validated by comparing with existing test data. They also conducted experimental tests with different speed ranges with a gel pack impactor on the stationary composite structure. They concluded that the composite structure had no appreciable damage at the lower velocities of the projectile, but the impactor material disintegrated. At moderate speeds, range impacts can cause fibre delamination and cracking. At high speed, the impactor penetrates through the composite structures.

Mao *et al.* (2008) investigated the penetration damage of a sandwich panel by a solid, round-shaped impactor with numerical analysis. The main objective is to understand the impact damage mechanism and load distribution of sandwich structures made by bonding CFRP panels to honeycomb, Nomex or foam cores. It was assumed that the impactor and support ring use an elastoplastic model of isotopically hardened constitutive

material. This research facilitates the design of a sandwich-based impact-resistant structure for low velocity impact applications.

Guida *et al.* (2009) carried out a bird impact analysis of FML leading edge of a transport aircraft. Fibre metal laminate samples were fabricated and tested to analyse their energy absorption properties. Three different fibre metal laminate models were designed using advanced finite element software. The soft body models were modelled with the Lagrangian approach to simulate impacts with large deformations correctly. The numerical simulations agreed with the experimental results, which demonstrated the ability of finite element tools in bird impact analysis.

Lavioe *et al.* (2009) conducted bird impact tests on rigid slabs using gelatine as a bird substitute material. They recommend using gelatine as reference material in further bird testing certification procedures. Experimental tests using gelatine as a bird substitute material validated the soft body numerical model. It facilitates numerical analysis compared to expensive experimental tests.

Salehi *et al.* (2010) analysed the effect of bird strikes on different types of aircraft bubble windows with different geometries and materials through numerical and experimental techniques. Bird impacted on a two-layer bubble window with a Polyvinyl Butyral (PVB) Interlayer. Numerical studies were carried out on sandwich and multi-walled stretched acrylic bubble windows. After evaluating different bird modelling techniques for the first case, the ALE method was chosen for the bird models in all cases. Different bubble windows were designed and constructed using stretch and cast acrylic, and their performance was evaluated.

Wang and Yue (2010) proposed a nonlinear viscoelastic model, Zhu-Wang-Tang (ZWT), using the theory of multiple integral nonlinear constitutive relations to solve the bird-aircraft windshield impact problem. The finite element models of the windshield, frame and curved frame were without rivet holes using finite element software ANSYS. Bird strike simulation was done using LS-DYNA. The plastic kinematic model was selected as the bird material model, and surface to surface tied contact was used between the gasket and windshield. The Von-Mises stress of the windshield structure at different speeds were studied, and the position of the maximum stress value of each part of the windshield structure changes. However, the order in which each component reaches the maximum stress value remains unchanged, windshield, spacer, frame, or arc frame. The spacer dissipates energy during the strike.

Smojver and Ivancevic (2011) performed a numerical analysis of soft body impact damage in aircraft structures with finite element software ABAQUS/Explicit. The Lagrangian method was used to model the soft body. They carried out a bird impact simulation on inboard flap of a typical large transport aircraft. Then conducted parametric analysis with different bird sizes, velocity and impact locations. They developed a sub modelling approach to reduce the computational time. The results showed that the bird impact damage depends on bird velocity, deflection, and impact location. The leading and trailing edges of the flaps are designed as a sandwich. The failure and damage modelling of the composite part of the flap structure is achieved through the built-in progressive failure and damage model of ABAQUS/Explicit. The impact site is at the junction of the skin and ribs. The flap structure withstood the impact, although the affected ribs and some lower skin and stringers elements met the specified failure criteria. According to their research, fibre breakage in tension is a crucial failure mode for most CFRP facing elements.

Guida *et al.* (2011) conducted a bird strike test with an 8-pound dead chicken on a leading edge made of aluminium alloy (AA 2024-T3), honeycomb core and GLARE laminate covers. Research revealed the accuracy of bird strike simulations and this study also demonstrated the high-strength impact resistance of GLARE laminate combined with sandwich composite.

Reglero *et al.* (2011) investigated the bird strike performance of leading edges with aluminium foams as a filler material. Bird impact tests were performed on two types of structures, *i.e.,* filled and emptied leading edges. The overall deformation and total loads in the tests were compared. The results showed that the leading edge structure with foam is 13% lighter than the original structure, the overall deformation performance is improved by a factor of 4, and the emitter loading is improved by a factor of 2.

Stanley *et al.* (2011) conducted bird-strike tests on the aluminium leading edge of a light transport aircraft. They have carried out a structural parametric optimization study on the wing leading edges with ribs and baffle plates subjected to bird impact. The parametric study showed that there is optimal rib spacing is required for controlling the deformation and the tearing of the skin. During the bird impact test on leading edges, the baffle plate was subjected to pull through tensile forces due to buckling of the skin. Therefore, the connection of the skin to the baffle is important, and its pull-through strength needs to be evaluated. Rivet selection was made based on the pull-through test on Monel and aluminium rivets of 3.2 mm and 4 mm in diameter. Alternative designs for a 4-pound bird strike were tested, and numerical simulations of these tests were performed. The

leading edge, segment assembly with the aluminium skin, aluminium baffle and CFRP rib configuration resisted the bird impact at the velocities of 112 – 118 m/s without penetration of the bird, and the final design was arrived based on the test results. The correlation of deformation modes between experimental and numerical solutions validated the finite element model.

Majzoobi *et al.* (2011) used the quasi-static tensile test results to calibrate the stress triaxiality fracture constant. This study explains the method for calculating the fracture constants for a new alloy.

Borvik *et al.* (2011) used the Johnson-Cook damage model to express the effects of the stress triaxiality, the strain rate, and the temperature on the strain to fracture, respectively, in three brackets. Damage constants with respect to different influencing parameters are generally calibrated individually.

Tho and Smith (2011) studied a bird strike simulation method based on multi-material ALE and SPH approaches in LS-DYNA. The parameters of the soft body model were calibrated to correlate hydrodynamic pressure with standard problems. Validated bird models were used to simulate bird strikes on BA609 Tiltrotor structures, which are rotor spinners, cockpit nose, wing leading edge and tail, for the most critical load test conditions. Hashin and Chang-Chang failure criteria were used to model fibres and matrices, respectively.

Liu *et al.* (2014) performed numerical simulations of bird strikes against honeycomb-based sandwich panels. These panels were made of honeycomb and 2024-T3 aluminium skin. The displacement of the panel's rear skin during soft body impact loading was recorded using strain gauges, and the strain was measured using a laser sensor. The finite element software was used to simulate the soft impact of the sandwich panel. The numerical simulation results were in good agreement with the experimental test results, and the finite element model was verified.

Vilamosa *et al.* (2015) describe how the flow stress properties of the material can be altered by heat treatment. This research also explained the temperature sensitivity of the elastic modulus. The experimentally found flow stress versus plastic strain curves up to large strains for all combinations of strain rate and temperature were used to identify the parameters controlling the evolution of the work-hardening variable.

Pahange and Abolbashari (2016) conducted a structural optimization study with varying wing components, *i.e.,* spar, rib, and skin. They summarized that the skin thickness

is the most critical design attribute for energy absorption characteristics of the wing leading edges.

Ijaz *et al*. (2017) proposed a modified Johnson-Cook model that includes the effect of grain size on the material model. This study explained that the heat treatment processes increase the mechanical properties by re-crystallizing the atomic structure and modifying the grain size. This study also described that the mechanical properties required to meet particular loading requirements could obtain by optimizing the material parameters of the particular alloy.

Orlando *et al.* (2017) carried out a bird strike analysis to demonstrate the CFRP flap capability in compliance with the crashworthiness regulations against soft body impact. They performed bird strike analysis on full-scale aircraft components using a 4-pound smooth particle hydrodynamic bird model at 100 m/s. The finite element model of the soft body was validated with an experiment test by striking a bird model on the rigid target with a velocity of 100 m/s. These bird models were then impinged into a composite plate to find their pressure distribution properties. Numerical analysis of the flap structure was performed using the material properties of the validated soft body impactor and composite plate target. It was observed that finite element simulations were able to analyse bird strike characteristics prior to full certification testing.

Khadyko *et al.* (2019) introduced a nanostructure model (NaMo), which forecasts the size distribution of hardening particles, the yield strength, the solute content, and the work hardening, then used to model the microstructure evolution of materials. The data from the quasi static tension tests were utilized to validate the predictions of NaMo and to analyse the relationships between the stress-strain behaviour, heat treatment, and microstructure of the various materials.

Di Caprio *et al.* (2019) studied the ability of the leading edge of the vertical tail to resist bird strikes. Taking into account mass savings and performance improvements, they analysed the structural properties of different material systems. They used unidirectional fibre-reinforced materials for the outer and inner face of the leading edge skins and other materials for the core.

Hou and Liu (2019) carried out a soft body impact simulation on a rotary engine fan assembly fixed hollow blade. The soft body model was established with smooth particles hydrodynamic formulation in the finite element software Pam-Crash and validated with an experiment test. Then, this bird model was impacted on the hollow blades of the rotary engine fan assembly to analyse its dynamic response against bird impact under

different operating loads. The results showed that bird impact velocity, impactor mass, impact position of the soft body and rotating speed of the fan are the relevant parameters that influence the deformation of the fan blade.

Yu *et al.* (2020) proposed a wing leading edge that satisfies the requirements of crashworthiness regulations. This bird strike resistance design was called Locally Strengthened Variable Thickness Skin (LSVTS). An experimentally validated finite element model was used to demonstrate the effectiveness of the wing leading edge design for soft body impacts. Numerical simulation results demonstrate that the new leading edge design can protect the wing skin from bird intrusion while maintaining the strength-to-weight ratio.

Sinha (2021) presented a semi-closed-form physics-based rotodynamic analysis that estimates transient soft body shock loads at the root of the blade and at the support bearings of the rotating fan shaft. In the numerical analysis, the soft body and the fan blade were considered cylindrical impactor and target, respectively. The high impulsive force created by the soft body impact was transferred to the entire engine support structure through the aerofoil, fan disk, rotor shaft, and rolling element bearings. The numerical results showed that the dynamic magnification factor for the transient vibratory reaction of the fan rotor struck by a soft body could be as high as three times that of the normal steady-state response of an equivalent unbalance.

Li *et al.* (2021) carried out a bird impact analysis on the fan blades to analyse impact damage and the influence of fan rotor unbalancing on the jet engine. The finite element model of the soft body was established by the smooth particle hydrodynamics method and verified by experiments. The key intake parameters were calculated from finite element simulations of validated soft bodies impacting the fan blades under the considered soft body intake conditions. This study revealed that it is important to incorporate bird impact resistance requirements in the modelling of turbine engine designs.

2.3 Problem identified from literature review

An extensive literature survey assessed the progress of soft body impact analysis on aircraft structures over the past 45 years. From the literature, it is concluded that there is no homogeneity or uniformity in soft body modelling approaches based on material modelling, geometric modelling and discretization methods. Depends on the different finite element software and available modelling methods, researchers use different approaches for

selecting material models, discretization methods, contact formulation, impactor geometry, and size. This fact makes each piece of literature about this subject have its value. Researchers around the world use different bird modelling techniques to simulate bird strikes. The advantages of finite element soft wares *i.e*., ABAQUS/Explicit, Msc-Dytran, Pam-Crash, LS-DYNA *etc.*, for predicting bird strike damage are well documented in the literature. The use of the suitable bird model and its validation with an experimental test is essential for relying on the results of bird strike simulation. The accuracy of the bird model with the experimental study, ease of bird modelling approaches, numerical instability issues in the approaches followed, time consumption *etc.,* are some of the criteria for the selection of a bird modelling technique. The major challenge of finite element modelling is that the soft body flows in a fluid-like manner and spreads over the target with high deformations during impact. The soft body models are usually validated by comparing the pressure distribution characteristics obtained by impacting the soft body on a rigid target with equivalent values from the experiment test. The numerical values of different studies vary based on the selected material models and modelling approaches. The available soft body models have not exhibited much correlation with the experiment test in the Hugoniot (initial peak) and stagnation (steady-state) pressure values. All researchers depend on Wilbeck's 45-year-old test data for validation, which has many limitations. The curves generated from the experimental test conducted by Wilbeck were measured from the centre pressure transducer with a sampling frequency of 300 kHz. These piezoelectric quartz pressure sensors used by Wilbeck were not designed for transient shock loads as they do not have adequate acceleration compensation and noise will appear in the results. The distance between the gun and target was also not mentioned. Lavoie *et al.* (2009) reminded us that the experimental pressure data by Wilbeck should only be seen as a reference for the general behaviour rather than as a tool of evaluation. Some research laboratories have conducted experimental tests later, but it is not available to the public. Hence, it is recommended to conduct a physical test by considering the factors developed by worldwide researchers, and it should be available to the researchers for future soft body impact analysis validations. The literature helped to learn different soft body projectile models in the finite element software ABAQUS/Explicit. A comparison study among these bird modelling approaches is very much required to select a suitable bird model for the parametric study.

The detailed literature review concluded that developing new materials to meet the specific needs of aircraft components is the primary focus of airframe manufacturers and material producers. The study concluded that defining the desired properties is necessary

to create custom alloys for aircraft components that meet their specific loading conditions. In order to achieve this, first, it is required to convert these specifications into microstructural objectives. These microstructural targets are then converted into compositional/process definitions. Therefore, one current challenge is to develop materials with improved structural performance for applications in leading edges against bird impact. The design studies showed that enhancing or optimising the flow stress parameters efficiently increases the material's capacity to absorb energy. The interdependence of material parameters makes it difficult to obtain a material with optimal properties suitable for a particular loading requirement. Therefore, finding factors through some Design of Experiments (DoE) methods may help to develop ideal materials for specific loading requirements such as bird strikes. A parametric study facilitates the identification of material parameters that control reaction forces and leading-edge deformation during bird impact. This understanding helps to tailor aluminium alloy with improved energy-absorbing characteristics and better resistance to bird impact damage.

Failure modelling of targets is also essential for accurate prediction of bird strike simulations. The literature helped to find suitable aluminium alloy and composite material models as well as various experimental tests performed by the researchers to validate the results. It is also understood that the research on the effects of high and low velocity rigid body impact on fibre metal laminates is enormous. But little research has been reported on the impact of soft bodies on fibre metal laminates. Comparison studies on different FML configurations is essential to select the FML configuration suitable to resist soft body impact.

The detailed literature review of the bird strike studies and future research possibilities concluded that the response of FML to bird impact involves many parameters such as a type of metal, fibre, matrix, stacking sequence, metal volume fraction, impactor geometry, target shape *etc.* This huge interdependence makes it difficult to obtain optimal FML. It is important to analyse the effect of metal thickness, and stacking sequence on the impact response and damage behaviour of GLARE laminates during soft body impact loading. Hence, failures due to soft bodies impacting aircraft structures require more observation, and the development of better impact-resistant materials to gain acceptance.

Chapter 3

Soft body modelling and validation

3.1 Introduction

Soft body impact can be defined as an impact in which the stress generated during impact significantly exceeds the strength of the material (Wilbek 1977). During impact, the soft body normally has the tendency to move as a fluid at high velocity. A soft body impact is an event characterized by the generation of a considerable impact force within a short period of time. Soft body impact modelling is a complex problem as it is an interaction of various complex numerical problems such as soft body modelling, contact definition, damage initiation and evolution models, removal of failed elements, *etc.* The high velocity impact results in highly nonlinear behaviour in terms of material and geometry. This aspect is more complicated because the soft body itself behaves more like a fluid that undergoes large deformations, eventually resulting in breakage into smaller particles. Hence, the exact determination of the impact forces becomes difficult at these high velocities. When a highly deformable soft body is impacted on a deformable target the loads couple due to the response of the target (Wilbeck 1977). Hence, to validate the behaviour of the soft body researchers neglected the target response to the impact pressures by considering target to be rigid.

The first step in bird impact simulation to develop an authentic bird material model to accurately predict the bird impact behaviour on various structures. Even though, the bird possesses a non-homogeneous and anisotropic internal structure, the bird tends to show hydrodynamic characteristics at higher velocities. Hence, the bird is assumed to be a soft body with minimal non- homogenous and anisotropic effects. The soft body impact is thus similar to a fluid impact. The soft body or bird has represented as projectile and the part of the aircraft that is subjected to impact has taken as target. Soft bodies exhibit highly

nonlinear behaviour during impact and it is difficult to model soft body which closely matches the behaviour of real impact event. The soft body models are usually validated by the comparison of pressure profile obtained by impacting the soft body on a rigid target, with equivalent values from experiment test (Wilbeck 1977). Wilbeck have conducted experiment test with impacting different soft body replacement material *i.e.,* porous gelatine, Room Temperature Vulcanized (RTV) rubber, Porous RTV rubber, dead chicken, beef. *etc.* on rigid target with different velocities and impact angles. The Wilbeck experiment tests concluded that a bird (chickens) can best be defined as a low strength material with the equation of state of water, with an average density of 950 kg/m^3 and 10% porosity. Later the researchers find that the porosity effects are highly negligible when considering soft body impact in simulation. A material with equation of state of water with density of 950 kg/m^3 is suitable to define a soft body. The researchers typically select the experiment test by Wilbeck when a porous gelatine normally impacting at a velocity of 117 m/s on rigid target for validation. And in this condition, the normalised Hugoniot and steady-state pressure imparted on the target was recorded as 5.7 and 1.02 respectively. The literature illustrated in **Table 3.1** explained that the pressure distribution values obtained in different numerical simulations have vast difference based on the selected material models and modelling approaches. The available bird models have not exhibited much correlation in the initial peak pressure and steady-state pressure values in validation with experiment test.

Table 3.1. The soft body model validation data collected from different literature

References	Velocity (m/s)	Soft body mass (kg)	Normalised Hugoniot pressure	Normalised stagnation pressure	Material model	Geometric model	Finite element formulation	Software
Johnson and Holzapfel (2003)	116	1.8	7.2	1.4	polynomial EOS	Hem. Cyl.	SPH	Pam-Shock
McCarthy *et al.* (2004)	200	1.8	16	2.2	Murnaghan EOS	Hem. Cyl.	SPH	LS-DYNA
Airoldi and Cacchione (2006)	200	0.6	6	1.4	Hydrodynamic (Type 7)	Cyl.	LAG	Pam-Crash
Chuan (2006)	116	1.82	17.4	1.01	Polynomial EOS	Hem. Cyl.	SPH LAG	LS-DYNA
Jenq *et al.* (2007)	116	1.8	6.5	1.4	Polynomial EOS	Hem. Cyl.	LAG EUL ALE	LS-DYNA
Mao *et al.* (2008)	225	1.82	2.61	0.34	Polynomial EOS	Hem. Cyl.	LAG	LS-DYNA
Lavoie *et al.* (2009)	116	1	14	0.9	Polynomial EOS	Hem. Cyl.	SPH LAG EUL	LS-DYNA
Smojver *et al.* (2011)	116	1.8	12.6	1.8	Mie-Gru. EOS	Hem. Cyl.	EUL	ABA. /Exp.
Smojver and Ivancevic (2011)	100	1.8	9	1.58	Mie-Gru. EOS	cube	CEL	ABA. /Exp.
Nishikawa *et al.* (2011)	100	1.54	16	2.13	Mie-Gru. EOS	cube	LAG	ABA. /Exp.

Note: Hem. Cyl. – Hemispherical ended cylinder, Cyl. - Cylinder, ABA. /Exp - ABAQUS/Explicit, Mie-Gru. EOS- Mie-Grunesian equation of state.

The main objective of the present chapter is to propose a finite element soft body model which exhibit more correlation with experiment test data. The specific objectives of the chapter are to (1) study the different bird material models *i.e.,* Mie-Grunesian equation of state, Mie-Grunesian equation of state for a multi-material model and user-defined equation of state (2) analyse and compare three soft body models (Lagrangian (LAG), Arbitrary Lagrangian-Eulerian (ALE) and Smooth Particle Hydrodynamics (SPH)) based on the set-up time, run time, deformation pattern and pressure distribution characteristics.

This chapter discusses the theoretical background of bird strikes, different material models, geometric modelling, different finite element modelling approaches, and a comparison of different soft body impact modelling approaches and their experimental validation.

3.2 Theoretical back ground

Hydrodynamic impact theory is best suited to study the soft body impact. Even though the soft body is non-homogeneous and anisotropic, at higher velocities, this non-uniformity and non-homogeneity are considered negligible and the soft body can easily be represented as a fluid flow impacting on the target. When a highly deformable soft body is impacted on a deformable target the loads couple due to the response of the target. Therefore, to validate the behaviour of the soft body researchers neglected the target response to the impact pressures by considering target to be rigid.

Soft body impact behaviour on rigid targets is classified into four phases *viz.* (a) the initial shock stage, (b) shock decay stage, (c) steady flow stage and (d) the pressure termination stage as shown in **Fig 3.1**. Initially, during the impact with velocity $\boldsymbol{u_0}$**,** the front face of the soft body projectile is immediately brought to rest, and hence as a result, shock wave (called Hugoniot shock) is established when the body impacts the target. The initial peak pressure created at this time is called the Hugoniot pressure, $\boldsymbol{P_H}$. Cassenti (1977) has been developed the governing equation for Hugoniot pressure, which is explained in **equation (3.4).** At shock decay stage, pressure decreases at the impact point due to the interaction between shock wave and release wave. At this time soft body begins to flow steadily after many interactions between shock wave and release wave. The end phase of the bird strike is distinguished by the decay of the impact forces and pressure exerted on the target. The contact pressure gradually decreases as the release waves meet

with shock waves. The soft body flows entirely radial at the point where steady flow is obtained, successively a steady stagnation point is reached.

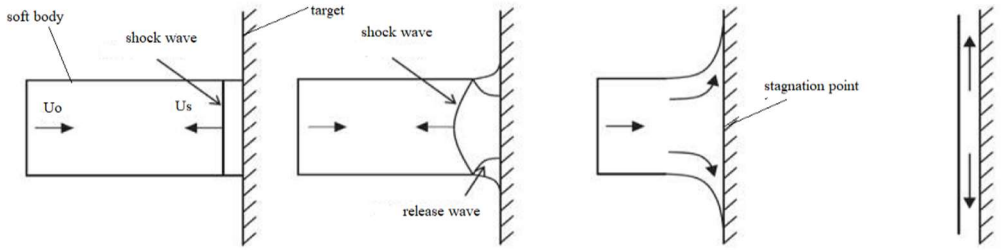

(a) Initial Shock b) Shock decay c) Steady flow d) Termination

Fig 3.1 The different phases of soft body during impact

(Wilbeck 1977)

The study on the impact forces and the impact duration of the soft body impact described in the following equations. The time duration of complete impact is ($\boldsymbol{T_0}$) is

$$\boldsymbol{T_0 = \frac{L_0}{u_0}} \qquad \textbf{(3.1)}$$

Where, ($\boldsymbol{L_0}$) length of the soft body projectile and ($\boldsymbol{u_0}$) is the impact velocity.

The pressure behind the shock can be inferred according to the conservation law. The equations for conservation of mass and balance of linear momentum can be written as **equation (3.2)** and **equation (3.3).** This is based on the assumption the flow is one-dimensional.

$$\boldsymbol{\rho_1 u_s = (u_s - u_p)} \qquad \textbf{(3.2)}$$

$$\boldsymbol{P_1 + \rho_1 u_s^2 = P_2 (u_s - u_p)} \qquad \textbf{(3.3)}$$

where, $\boldsymbol{\rho_1}$ and $\boldsymbol{\rho_2}$ are the density of soft body material, $\boldsymbol{P_1}$ and $\boldsymbol{P_2}$ are the pressure before and after the shock front and $\boldsymbol{u_s}$ and $\boldsymbol{u_p}$ are the shock propagation velocity and particle velocity, respectively. The Hugoniot pressure $\boldsymbol{P_H}$ (Cassenti 1977) is defined in **equation (3.4)** below

$$P_H = P_2 - P_1 = \rho_1 u_s u_p \quad (3.4)$$

When the steady state is obtained, the flow pressure p_s can be calculated using the Bernoulli relationship (Wilbeck 1977). Bernoulli's equation can be written as

$$\int \frac{dP}{\rho} + \int u du = K \quad (3.5)$$

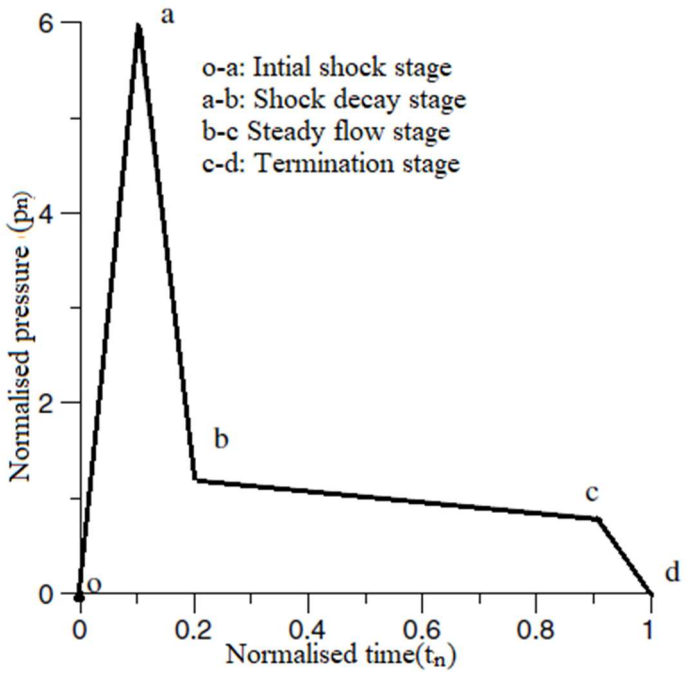

Fig 3.2 Contact pressure variation during soft body impact

(Wilbeck 1977)

The variables P, ρ and u stand for pressure, density and particle velocity of soft body material and K is a constant. The pressure at any point along the impact surface can obtained from the **equation (3.5)** by integrating from initial time t_0 to t. For the normal impact of a uniform cylindrical projectile on a rigid target specifies that the central point of the target is the stagnation pressure, P_s and the velocity at the central point is zero. Therefore, at the centre of the target plate, the **equation (3.5)** takes the form

$$\int_{p_0}^{(p_s+p_0)} \frac{dP}{\rho} = \frac{u_0^2}{2} \quad (3.6)$$

where, p_0 and u_0 are the pressure and velocity of the uniform projectile before impact. To find pressure at any point along the impact surface from **equation (3.6),** the velocity at that point and the equation of state of the projectile material, $\rho = \rho(P)$, must be known. Assuming that the fluid behaves as an incompressible material, stagnation pressure p_s ,becomes,

$$P_s = \frac{1}{2}\rho u_0^2 \quad \textbf{(3.7)}$$

For most materials, the density has a tendency to increase as the applied pressure increases. Therefore,

$$p_s \geq \frac{1}{2}\rho u_0^2 \quad \textbf{(3.8)}$$

From linear Hugoniot equation, the shock velocity, u_s in water and the particle velocity, u_p, is related as follows:

$$u_s = c_0 + s u_p \quad \textbf{(3.9)}$$

Where, c_0 is the speed of sound in the material and s is a material constant.

3.2.1 Wilbeck experiment

Wilbeck (1977) studied the impact behaviour of low strength projectiles to develop a hydrodynamic bird model and synthetic substitute material that shows the approximate characteristics of the bird. They conducted tests with various materials such as neoprene, Room Temperature Vulcanized (RTV) rubber, Porous RTV, gelatine, porous gelatine, chicken, and beef with normal and oblique impact for different impact velocities. Wilbeck also studied the response of gelatine mixtures with and without porosity to find a suitable replacement material for the bird strike test. These tests were characterized by shock and steady state pressures that occurred during the time of impact.

The Wilbeck experiment utilized Hopkinson bar with strain gages to measure impulse directed to the rigid plate during the soft body impact. The soft body was kept in a sabot built of high-density polyethylene. This heavy sabot was required to hold out the high acceleration forces produced by the exploding gas. As the sabot went down the gun barrel, the high-pressure gases at the rear of the sabot were emitted in the blast chamber. The high-pressure gas must be fully released to generate a constant velocity in the soft body before

impact. When the sabot and soft body touched the end of the blast tank, the sabot was confined by the sabot stopper. The stopper was so fabricated to permit the soft body to maintain its movement without the loss of velocity. A flat plate with pressure transducers was utilized to calculate pressure distribution characteristics at various points on the plate surface. The behaviour of the target material to the high-velocity impact pressures can be neglected by considering the target to be rigid. This fact makes the problem simpler and permits the researcher to focus on the behaviour of the soft body. For normal impacts, this implies that the impulse conveyed to the target must be equal to the initial momentum of the soft body, assuming the target is rigid. Soft body impact pressure is recorded with piezoelectric transducers quickly mounted on rigid steel plates. As the soft body is impacted on the surface with constant velocity the kinetic energy loss due to change in velocity is assumed to be zero. **Fig 3.3** shows the pressure distribution characteristics recorded when the bird substitute material hits a rigid target at a typical velocity of 117 m/s. Experimental studies were carried out on birds ranging in body weight from 60 g to 4 kg and with velocities ranging from 50 to 300 m/s. The Hugoniot pressures measured at different velocities and masses are shown in **Fig 3.4.**

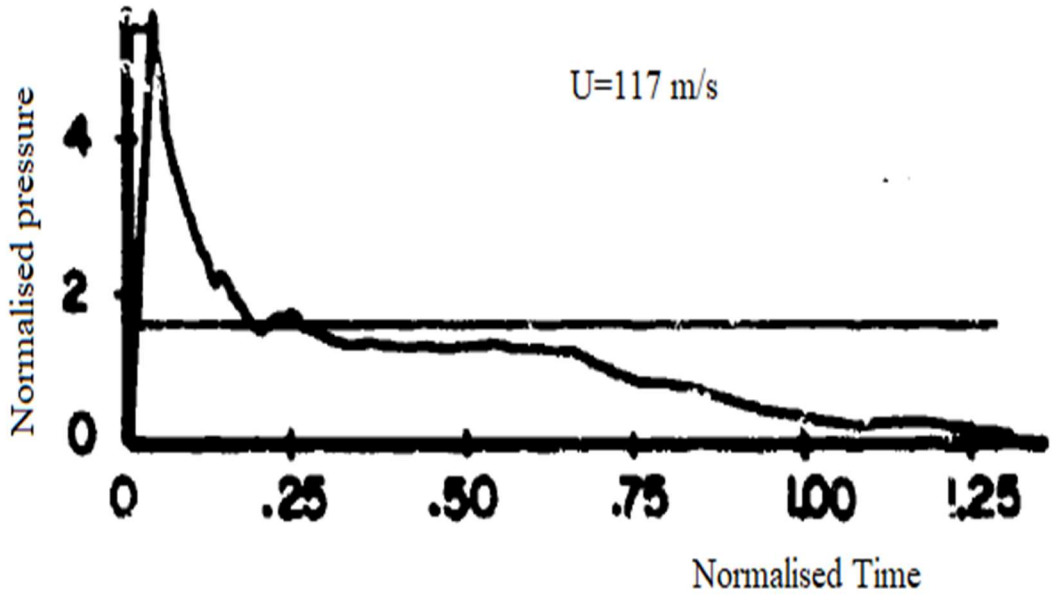

Fig 3.3 Pressure distribution characteristics of the soft body replacement material (porous gelatine) impacting normally on the rigid target with a velocity of 117 m/s

(Wilbeck 1977)

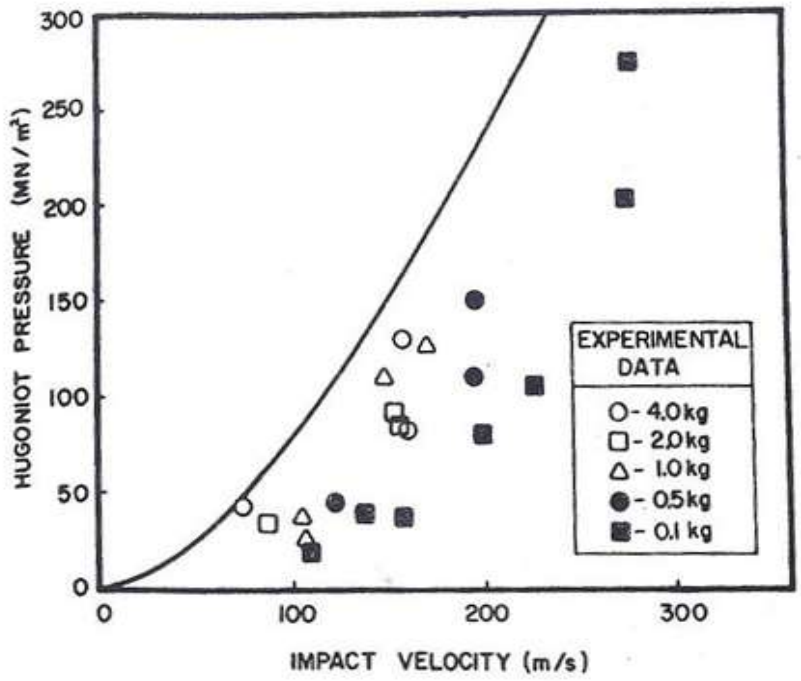

Fig 3.4 Hugoniot pressure recorded when porous gelatine impacted on rigid target, measured from different velocities and masses

(Wilbeck 1977)

3.3 Material modelling of the soft body

The material models used to define the soft body are different in the studies done by different authors. The researchers consider that soft body motion is similar to elastoplastic or hydrodynamic fluid flow. While modelling, the elastic-plastic behaviour of the material is ignored and reduced to equation of state by describing the hydrodynamic pressure-volume behaviour at high pressures (Johnson and Holzapfel 2003). Wilbeck finalized that a soft body can be accurately modelled by a mixture of 85-90% volume of water and 10-15% of air, which means material porosity is taken into account due to trapped air in the lungs and bones. Air content reduces density, bulk modulus and speed of sound. Porosity in the material results in a reduction in impact velocity and impact pressure. The decrease in density results in a decrease in stagnant pressure during steady flow. The resulting reduction in stagnation pressure is relatively small due to the counter-effect of compressibility.

Wilbeck proposed two independent equations of state to describe the behaviour of the soft body during the shock phase and the steady-state phase. An equation of state is a

thermodynamic relationship between the density ($\boldsymbol{\rho}$) or volume ($\boldsymbol{V}$), internal energy ($\boldsymbol{E}$) or temperature ($\boldsymbol{T}$), and pressure ($\boldsymbol{P}$).

The pressure **($\boldsymbol{P}$)** can be expressed as

$$\boldsymbol{P = P(V, E) = P(V, T)} \tag{3.10}$$

Wilbeck has derived an independent equation of state models to define the shock phase and the steady-state of the soft body model, based on the one-dimensional hydrodynamic theory. As per this study, a porous material is basically a mixture in which one of the constituents is air. The amount of porosity of the material (z), is described as the volume fraction of the air in the mixture. $\boldsymbol{\rho_{air}}$ represents the density of the air. The full density (without porosity) of the soft body material is represented as $\boldsymbol{\rho_f}$ and average density of the soft body material with porosity is characterised as $\boldsymbol{\rho}$ and can be defined by the expression

$$\boldsymbol{\rho = z\rho_{air} + (1 - z)\rho_f} \tag{3.11}$$

The equation of state for shock compression of the porous material is given by

$$\boldsymbol{\frac{\rho_1}{\rho_2} = (1 - z)\left(\frac{P_2}{A_f} + 1\right)^{-1/B_f} + z(1 - q)} \tag{3.12}$$

where, $\boldsymbol{A_f = \frac{\rho_1 C_{0water}^2}{(4s_{water} - 1)}}$, $\boldsymbol{B_f = (4s_{water} - 1)}$ and

$$\boldsymbol{q = \left(\frac{2\bar{P}s_{air} + \frac{\rho_1 C_{0,air}^2}{P_1}}{2\bar{P}s_{air}^2}\right) - \frac{\sqrt{\left(2\bar{P}s_{air} + \frac{\rho_1 C_{0,air}^2}{P_1}\right)^2 - 4\bar{P}^2 s_{air}^2}}{2\bar{P}s_{air}^2}} \tag{3.13}$$

where, $\boldsymbol{c_0}$ is the velocity of sound (velocity of propagation of an infinitesimal disturbance) in the material, $\boldsymbol{s}$ is a constant and $\boldsymbol{\bar{P} = \frac{P_2}{P_1} = \frac{\rho_1 C_{0,air}^2}{P_1} \frac{q}{(1 - s_{air} q)^2}}$

The equation of state for isentropic compression phase is given by

$$\boldsymbol{\frac{\rho_1}{\rho_2} = (1 - z)\left(\frac{P_2}{A_f} + 1\right)^{-1/B_f} + z\left(\frac{P_2}{P_1} + 1\right)^{-1/\gamma}} \tag{3.14}$$

where, γ is the ratio of specific heats.

Steady-state stagnation pressure of one-dimensional compressible flow is related to the velocity with Bernoulli equation is given by

$$\int_{P_1}^{P_2} \frac{dP}{\rho} = \frac{u_p^2}{2} \quad \textbf{(3.15)}$$

For a linear Hugoniot, shock velocity, $\boldsymbol{u_s}$ in water and the particle velocity, $\boldsymbol{u_p}$, is related as follows:

$$\boldsymbol{u_s = c_0 + s u_p} \quad \textbf{(3.16)}$$

where, $\boldsymbol{c_0}$ is the velocity of sound (velocity of propagation of an infinitesimal disturbance) in the material and $\boldsymbol{s}$ is the slope of the $\boldsymbol{u_s}$–$\boldsymbol{u_p}$ curve.

3.3.1 Material models

The material models available in ABAQUS/Explicit which is suitable to define soft body impact behaviour are described below

Mie–Grüneisen equation of state

The hydrodynamic behaviour of soft body can effectively represent with Mie-Grüneisen equation of state (EOS) material model, which define volumetric strength and pressure to density ratio of the material. Soft body can be modelled as incompressible or compressible fluid flow using Mie–Grüneisen equation of state.

The equation of state of the Mie– Grüneisen material introduced by Cochran and Chan

$$\boldsymbol{p(\rho, e) = p_{ref}(\rho) + \Gamma\rho(e - e_{ref}(\rho))} \quad \textbf{(3.17)}$$

Where, $\boldsymbol{p_{ref}}$ and $\boldsymbol{e_{ref}}$ are pressure and energy of the reference state. The reference state is always represented by ***P-V*** curve (Wu *et al.* 2014). Here Hugoniot curve is considered for reference state as a function of the density, $\boldsymbol{\rho}$ and the specific internal energy, $\boldsymbol{E_m}$ and the **equation (3.17)** becomes

$$\boldsymbol{P - P_H = \Gamma\rho(E_m - E_H)} \quad \textbf{(3.18)}$$

Where, $\boldsymbol{P_H}$ and $\boldsymbol{E_H}$ are the Hugoniot pressure and specific internal energy at shock which are functions of density only, and $\boldsymbol{\Gamma}$ is the Grüneisen coefficient which is defined as

$$\boldsymbol{\Gamma = \Gamma_0 \times \rho_0/\rho} \quad \textbf{(3.19)}$$

Where, $\boldsymbol{\Gamma_0}$ is a material constant and $\boldsymbol{\rho_0}$ is the reference density.

The Hugoniot energy, $\boldsymbol{E_H}$ is related to the Hugoniot pressure by

$$\boldsymbol{E_H = P_H \eta / 2\rho_0} \quad \textbf{(3.20)}$$

where, $\boldsymbol{\eta = 1 - \frac{\rho_0}{\rho}}$ is the nominal volumetric compressive strain. $\boldsymbol{\rho_0}$ and $\boldsymbol{\rho}$ represent the density in initial and stressed condition respectively. Combining **equation (3.17), equation (3.18)** and **equation (3.19),** while eliminating $\boldsymbol{\Gamma}$ and $\boldsymbol{E_H}$ from the above equations, the equation changes to:

$$\boldsymbol{P = P_H(1 - \Gamma_0 \eta/2) + \Gamma_0 \rho_0 E_m} \quad \textbf{(3.21)}$$

From linear Hugoniot, a common fit to the Hugoniot data is given by

$$\boldsymbol{P_H = \rho_0 c_0^2 \eta / (1 - s\eta)^2} \quad \textbf{(3.22)}$$

Combing **equation (3.20)** and **equation (3.21)** linear $\boldsymbol{u_s}$–$\boldsymbol{u_p}$ Hugoniot form is written as

$$\boldsymbol{P = \frac{\rho_0 c_0^2 \eta}{(1-s\eta)^2}\left(1 - \frac{\Gamma_0 \eta}{2}\right) + \Gamma_0 \rho_0 E_m} \quad \textbf{(3.23)}$$

where $\boldsymbol{\rho_0\ c_0^2}$ is equivalent to the elastic bulk modulus at small nominal strains. The above expressions derived by considering the soft body as simple hydrodynamic and incompressible material with zero shear strength (Chizari *et al.* 2009).

Table 3.2. Mie-Grüneisen equation of state material parameters of soft body (Smojver and Ivancevic 2011; Wilbeck 1977).

Density ($\boldsymbol{\rho}$)	Speed of sound ($\boldsymbol{c_0}$)	Material Constant ($\boldsymbol{s}$)	Grüneisen coefficient ($\boldsymbol{\Gamma_0}$)
950 kg/ m^3	1482.9 m/s	2	0

User defined equation of state

The user-defined equation of state gives the opportunity to create the volumetric response behaviour of the soft body replacement material along with user subroutine VUEOS. It can define pressure as a function of density and specific internal energy through user-defined equation of state. The finite element software resolves the energy equation

along with EOS utilizing the iterative method. The VUEOS subroutine can include the material properties as specified in **Table 3.3.**

Table 3.3 User defined equation of state material parameters of soft body

(Wang *et al.* 2009; Smojver and Ivancevic 2011)

Density ($\boldsymbol{\rho_0}$)	Speed of sound ($\boldsymbol{c_0}$)	Material Constant ($\boldsymbol{s}$)			Specific internal energy ($\boldsymbol{E_m}$)	Volume correction coefficient ($\boldsymbol{a}$)	Grüneisen coefficient ($\boldsymbol{\Gamma_0}$)
		$\boldsymbol{S_1}$	$\boldsymbol{S_2}$	$\boldsymbol{S_3}$			
950 kg/m^3	1482.9 m/s	1.92	-0.096	0	0	0	0.35

Mie-Grüneisen equation of state -multi material model

The Mie-Grüneisen equation of state can efficiently model most materials but the linear ($\boldsymbol{u_s}$–$\boldsymbol{u_p}$) correlation **(equation 3.16)** is not effective for the highly compressed states (Steinberg 1987). Hence, when the porosity increases this equation of state becomes invalid. The modified Mie-Grüneisen mixture model can expeditiously manipulate compressible states in multi-phase flow. Water- air mixture can effectively model as a compressible fluid flow with the Mie–Grüneisen equation of state (Wu *et al.* 2014). The soft body can be modelled as compressible fluid with material parameters for water and air and it is illustrated in **Table 3.4** and **Table 3.5**. The Mie-Grüneisen equation of state for compression of water is described in **equation (3.24)** (Miller and Puckett 1996; Wu *et al.* 2014)

In compression state $\boldsymbol{\mu > 0}$ and $\boldsymbol{\mu = \eta - 1}$

$$\boldsymbol{P = \frac{\rho_0 c_0^2 \mu\left[1+\left(1-\frac{\Gamma_0}{2}\right)\mu-\frac{a}{2}\mu^2\right]}{\left[1-(S_1-1)\mu-S_2\frac{\mu^2}{(1+\mu)}-S_3\frac{\mu^3}{(1+\mu)^2}\right]^2} + (\Gamma_0 + a\mu)E_m} \qquad \textbf{(3.24)}$$

Here $\boldsymbol{S_1, S_2, S_3}$ are constants and $\boldsymbol{a}$ is the first-order volume correction coefficient

For expanded material (air) Mie-Grüneisen equation of state can be expressed as (Miller and Puckett 1996; Shyue 2001)

$$\boldsymbol{P = \rho_0 c_0^2 \mu + (\Gamma_0 + a\mu)\, E_m} \qquad \textbf{(3.25)}$$

Where, $\boldsymbol{\rho_0}$ is the initial density and $\boldsymbol{E_m}$ is the specific internal energy. Hence, air is a gaseous material and not able to withstand either shear stresses or negative pressures, no strength or failure relations are needed for air.

Table 3.4 Mie-Grüneisen equation of state material parameters of water

(Wang *et al.* 2009)

Density ($\boldsymbol{\rho_0}$)	Speed of sound ($\boldsymbol{c_0}$)	Material Constant ($\boldsymbol{s}$)			Specific internal energy ($\boldsymbol{E_m}$)	Volume correction coefficient($\boldsymbol{a}$)	Grüneisen coefficient ($\boldsymbol{\Gamma_0}$)
		$\boldsymbol{S_1}$	$\boldsymbol{S_2}$	$\boldsymbol{S_3}$			
1000 kg/m^3	1482.9 m/s	1.92	-0.096	0	0	0	0.35

Table 3.5 Mie-Grüneisen equation of state material parameters of air

(Wang *et al.* 2009)

Density ($\boldsymbol{\rho}$)	Speed of sound ($\boldsymbol{c_0}$)	Material Constant ($\boldsymbol{s}$)	Grüneisen coefficient ($\boldsymbol{\Gamma_0}$)
1.25 kg/ m^3	340.9 m/s	1.4	0

The three equation of state material models *i.e.,* Mie-Grüneisen equation of state, Mie-Grüneisen equation of state for multi-material model and user-defined equation of state have studied detailly to select a material model to apply in the soft body used for further studies. The current research mainly based on material parametric analysis so the number of simulations to be conducted is high. The computational time and set up time are major factors to be considered other than accuracy. The material modelling with a user defined equation of state requires high computational time. While studying the impact problem with the multi-material bird model, it has been understood that the effect of porosity is very much negligible and the porosity effect are not required to be considered. From the comparison study results, it has been concluded that the Mie-Grüneisen equation of state material model with parameters mentioned in **Table 3.2** can effectively use to model the soft body material behaviour.

3.4 Geometric modelling of the soft body

The artificial replacements for birds with simplified geometries such as cylinders, cylinders with hemispherical ends, ellipsoids, or spheres are considered to analyse bird impact behaviour. Meguid *et al.* (2008) studied the effect of geometry on soft body impact with three models and different aspect ratios. This study showed that the initial contact area between the soft body and the target has a considerable effect on the initial impact pressure during the first phase of impact. They also concluded that the aspect ratio does not affect the peak impact pressure. From the literature (Airoldi and Cacchione 2006; McCarthy *et al.* 2004; Meguid *et al.*2008), soft body projectile geometry has been idealized as a cylinder with hemispherical ends due to the fact that this geometry showed the best correlation with real birds in experimental tests.

The cylinder with hemispherical ends and with length to diameter ratio of 2 is selected as geometric model of the soft body. The cylinder has length and diameter of 114 mm each with end caps having a 57 mm radius and a square plate of length a 500 mm is considered as the rigid target, as shown in **Fig 3.5.**

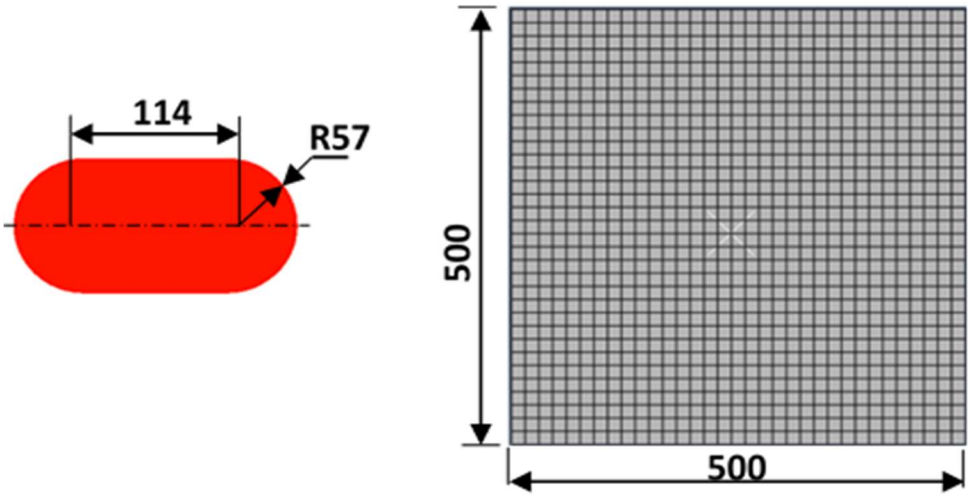

Fig 3.5 Model of soft body projectile and rigid target (All dimensions in mm)

3.5 Finite element procedure

The soft body model is created as per the dimensions shown in **Fig 3.5** and material properties are applied as given in **Table 3.2**. The target plate was modelled as per the dimensions, shown in **Fig. 3.5**. Then, the material properties of steel: density (***ρ***) =7800

kg/m^3, elastic modulus (***E***) =207,000 MPa and Poisson's ratio (***ν***) =0.33 is given to the target. The 500 x 500 mm target plate meshed with 1155 shell elements. These elements are applied with the rigid body constraint command available in ABAQUS/Explicit. A reference point is created on the centre node of the rigid plate, and then displacement/rotation of the point is fixed to zero as shown in **Fig. 3.6**. Then, an initial velocity of 117 m/s was given to the soft body. The contact algorithm obtains the interaction between the soft body and the rigid body target. ABAQUS/Explicit has two built-in algorithms for defining contact and interaction behaviour: the contact pair algorithm and the general contact algorithm in ABAQUS analysis user's manual (2007). This study used a general contact algorithm to define forces and pressures on rigid targets. General contact algorithms use complex contact conditions, and the contact between the soft body and the rigid target is considered to be less frictional. Since friction does not play a significant role in high-speed impact, it is assumed to be frictionless, thus avoiding convergence problems. Mesh convergence analysis is carried out on the soft body models to verify the accuracy of the model with the experimental test results. Based on this, the soft body is meshed with 60625 solid elements and converted into a set of particles. Thus, the total number of elements for soft body and target are 61780.

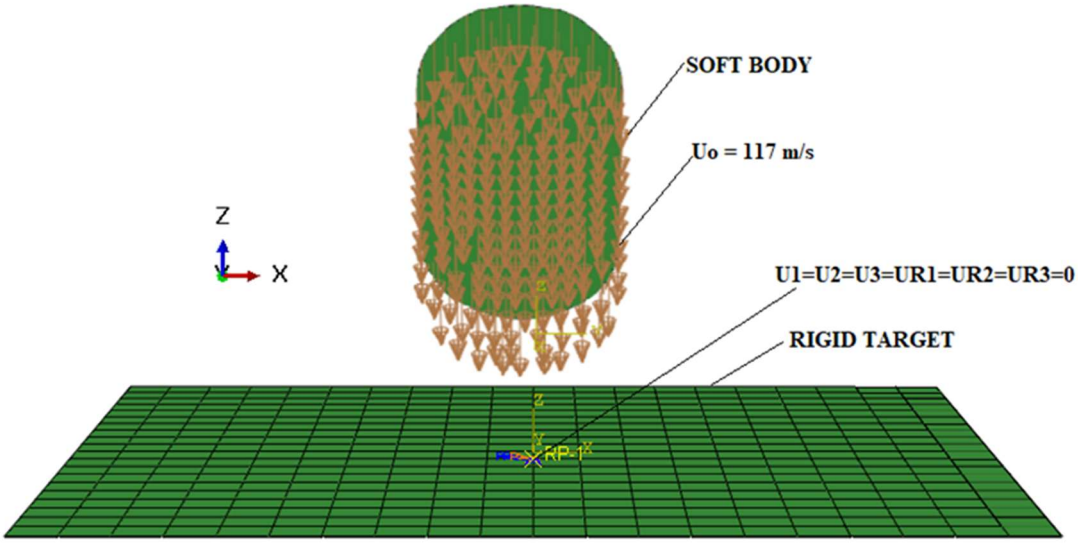

Fig 3.6 Loading and boundary conditions of soft body and rigid target

3.6 Soft body projectile modelling approaches

Three different finite element approaches, such as Lagrangian (LAG), Arbitrary Lagrangian-Eulerian (ALE), and Smooth Particle Hydrodynamics (SPH) formulations,

have been used to model the soft body impact (projectile) behaviour. A comparative study of three different available analytical methods helps find the suitable methods for soft body modelling. This study helps the researchers to choose the suitable method that suits the right purpose with the constraints of resources, time and the need for accuracy.

3.6.1 Lagrangian (LAG) approach

The Lagrangian approach is a finite element modelling method used in solid mechanics. It divides a domain into small geometries called elements, and the state of the solid can be analysed through the simulation using mathematical relations. The various formulations of finite element modelling differ in the reference coordinates used to define the motion and governing equations. Lagrangian methods use material coordinates as a reference. The nodes of the Lagrangian mesh are connected with particles in the material under consideration. The nodes of each mesh pursue a single particle in motion. Boundary nodes always exist in material boundaries. Therefore, the application of boundary conditions is simplified. Both the material interfaces and the free surfaces move with the mesh. The mesh is embedded in the structure; the material properties can be easily tracked at any point in the structure. This method is mainly used to describe the behaviour of solid materials under load. Although the soft body material behaves like a fluid during impact, it can be successfully modelled using Lagrangian finite element methods (Airoldi and Cacchione 2006; Iannucci 2000; Stoll and Brockman 1997). The main disadvantage of the Lagrangian method is getting inaccurate results, and the requirement for remeshing due to excessive mesh deformations. If mesh distortion is too large, excessively distorted elements will decrease explicit integration algorithms stable time increment to an unacceptable level or even lead to numerical problems and premature analysis termination—severe mesh tangling results in negative volumes in the numerical solver due to the elements folding over themselves. Artificial oscillations in the contact forces on the target due to the discretised nature of the simulated contact (Stoll and Brockman 1997). Adaptive remeshing/rezoning, and "small-strain" simplification are the different methods used to prevent such numerical instabilities. But these methods also have inherent disadvantages like removing mass and strain energy from the structure and increasing solution time *etc*.

3.6.2 Arbitrary Lagrangian-Eulerian (ALE) approach

The ALE formulation presented by stocker (1999) combines the Lagrangian and Eulerian formulations, which are successfully used to model fluid-structure interaction problems. Considering the soft body behaviour of the fluid during impact, the ALE method is a powerful tool to describe the soft-body impact behaviour (Tho and Smith 2011). In this approach, the user sets the reference arbitrarily to use the advantages of Lagrangian and Eulerian formulations while also reducing the disadvantages. In the Eulerian approach, the mesh and the associated nodes are normally fixed in space, and the material moves through the mesh. Element deformation is not possible since the mesh is fixed. The main application of Euler method is fluid modelling. It is hard to keep track of material interfaces and material history. Based on the ALE method, the arrangement of the grid is independent of fluid motion. The mesh can be moved to follow boundary motion, resolving complex flow properties and preventing mesh tangling. The computational mesh nodes may be moved with the continuum in a usual Lagrangian manner or held fixed in a Eulerian manner. The background void grid can move and stretch if needed, rather than being fixed in space. In the ALE method, the bird material flows relative to the Euler mesh, thus avoiding significant mesh deformation. The impacting loads are transferred to the Lagrangian mesh of the impacted structure through an ALE coupling algorithm. The disadvantage of this method is that it can only handle a single material in an element (Nizampatnam and Horn 2008).

3.6.3 Smoothed Particles Hydrodynamic (SPH) approach

The SPH formulation is a meshless Lagrangian technique introduced by Lucy (1977). The basis of SPH is interpolation theory and smoothing kernel functions. In this formulation, the state of a system is defined by a set of particles that attains individual material properties and flows according to the governing conservation equations. The equations conservation of mass, momentum, and energy of continuum mechanics are converted from partial differential equations into integral equations using a smoothing kernel function. (Monaghan 1992). The smoothing kernel function gives the kernel rank of the considered field variable at the spatial location. Beyond a radius proportional to the smoothing length ($\boldsymbol{h}$), these normalization kernels must disappear or become negligible. In the limit, the smoothing kernel must be close to the delta function as $\boldsymbol{h} \rightarrow 0$. The kernel function provides the class of influence of a point in the continuum. Smooth length finds

the number of neighbouring particles contained within the sphere of influence. Integration by parts grants the spatial derivatives of the unknown field variables to be reintegrated by the (known) derivatives of the smoothing kernel. The resulting integral equations are reintegrated by sums over discrete points in space that may be considered the centroids of the "smoothed particles" for numerical evaluation. Each particle has an included mass, velocity, and stress state developed according to discrete conservation equations.

At first, this method was used by Lucy (1977). Gingold and Monaghan (1992) used the SPH method for the numerical analysis of astrophysical phenomena. This method also used to resolve other physical problems in continuum mechanics, bird impact problems (McCarthy *et al.* 2004; Tho and Smith 2011), hypervelocity space debris impact problems (Groenenboom 1997; Kamoulakos and Groenenboom 1998), and ductile and brittle damage in solids (Gouskov 2018). Owing to the absence of a grid, this formulation permits finding a solution for many problems that are hardly reproducible in other classical methods to avoid the problem of large mesh deformations or tangling. The problem of irregular mesh geometries can be solved with meshless SPH methods.

3.7 Finite element modelling and analysis of the soft body

The behaviour of the soft body impact on a rigid target is simulated as described by the experimental study conducted by Wilbeck (1977) and is used for the validation of the bird model used for further studies. The impact simulation is carried out by impacting the soft body model on a rigid target with an impact velocity of 117 m/s. The impact velocity ($\boldsymbol{u_o}$) have been selected as 117 m/s based on FAA standard requirements for the class of aircraft under consideration. Three different finite element approaches have generally used to model the soft body impact behaviour. Three alternative soft body modelling approaches are provided in FE software ABAQUS/Explicit; *i.e.,* LAG, ALE and SPH. With the defined material and geometric parameters, a comparison study has been conducted between the finite element modelling approaches for the accurate formulation of the soft body projectile. These three finite element models are validated with the comparison of the pressure profile generated at the rigid target when the soft body impacted normally at a velocity of 117 m/s with experimental test data. The normalized time is calculated with **equation (3.26)**

$$\boldsymbol{t_n = \frac{t}{T_0}} \qquad \textbf{(3.26)}$$

Where, t is step time and T_0 is the time desired for complete impact is calculated with **equation (3.1)** is 1.94 ms.

The normalized pressure is calculated from **equation (3.27)**

$$P_n = \frac{p}{P_s} \tag{3.27}$$

Where, p and P_s are the pressure and stagnation pressure of the soft body model. The stagnation pressure is calculated with **equation (3.7)** is 6.5 M Pa.

3.8 Results and discussion

3.8.1 Modelling and analysis with Lagrangian approach

Lagrangian soft body projectile is meshed with three-dimensional solid elements as shown in **Fig 3.7**. The element straining or distortion is the main problems encountered in Lagrangian bird impact analysis. The soft body and rigid target material parameters and impact conditions are selected to be the same as those of experiment test conditions presented by Wilbeck (1977). These impact conditions are selected based on FAA standard requirements for the class of aircraft under consideration. An initial velocity of 117 m/s was assigned to the soft body while keeping it a little away from the rigid plate to notice its initial impact behaviour.

The mesh convergence analysis is conducted to verify the accuracy of the elements in this specific case where the soft body model impacted the rigid target with a velocity of 117 m/s. The finite element models are meshed by systematically reducing the size of the elements. The soft body models are discretized with 7829, 10321,20429 and 60625 solid elements. These soft body models are numerically analysed to verify the accuracy of the model with the experiment test. It is observed that the simulated peak pressure came close to a particular value reported by Wilbeck when the total number of elements of the soft body is selected to be 60625.

The rigid plate is meshed with 1155 shell elements and is provided with the rigid body constraint command available in the ABAQUS/Explicit. The boundary of the rigid plate is fully fixed with zero degrees of freedom, as shown in **Fig 3.7**. The soft body moving with an initial velocity of 117 m/s impacted on a target is analysed numerically with finite element software ABAQUS/Explicit. The impact simulation is carried out by impacting the

Lagrangian soft body model on the rigid target as shown in **Fig 3.7**. The CPU time taken to complete the simulation was 360 sec. After the complete impact of the soft body on the rigid target, compared the pressure distribution characteristics predicted numerically with the experimental test data reported by Wilbeck under the same bird impact conditions

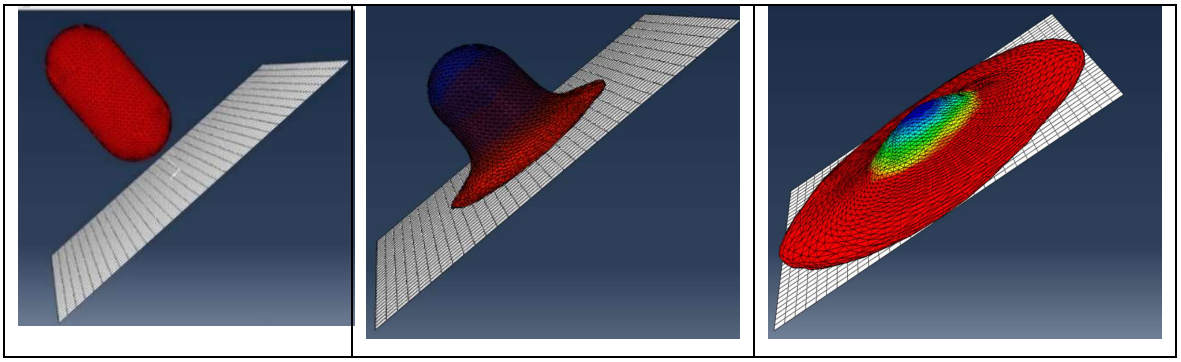

Fig 3.7 Lagrangian soft body impacting on the rigid target

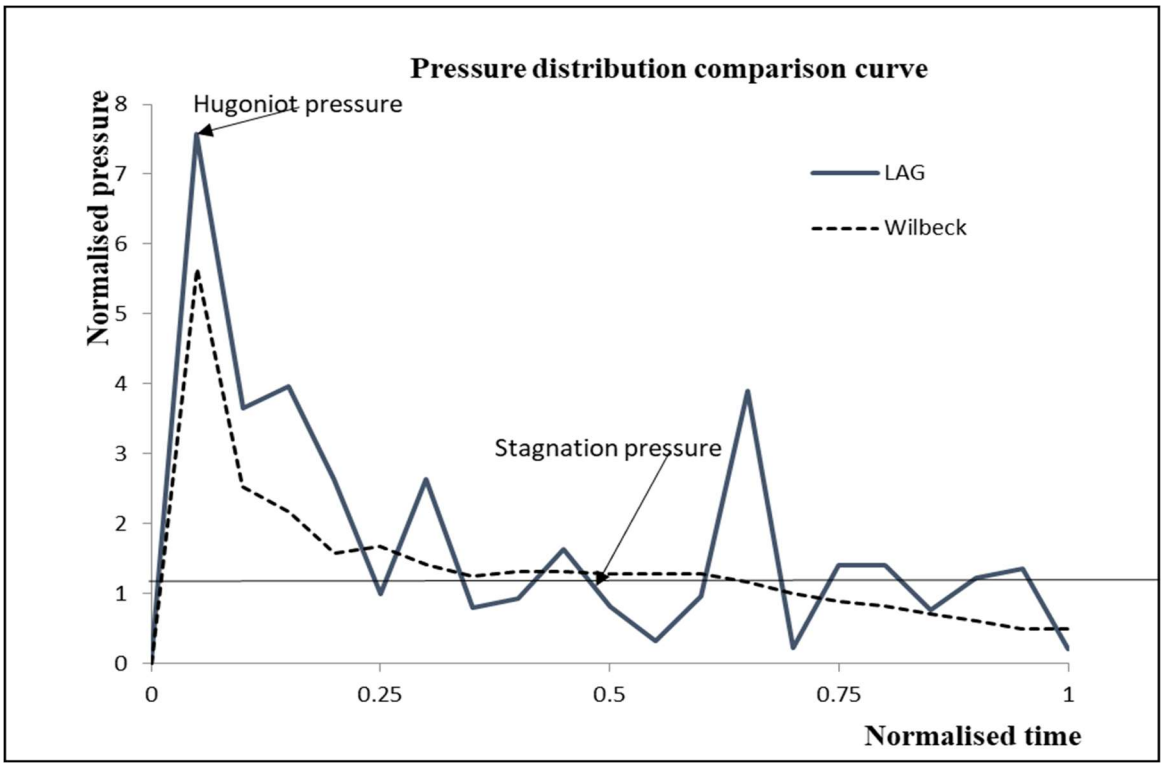

Fig 3.8 Comparison of the pressure profile of Lagrangian soft body model with Wilbeck experiment

The comparison of the average pressure distribution at the rigid target of the Lagrangian simulation analysis and the Wilbeck (1977) experiment test is shown in **Fig 3.8.** The **Fig 3.9** shows the deformation pattern of the Lagrangian model at different times. The soft body model showed the same deformation pattern observed from the experimental studies. But it is observed from the results that some of the elements are heavily strained. The initial peak pressure is reported at about t_n=0.05 and its value is recorded as 49.27 MPa. When comparing the generated pressure distribution curves in **Fig 3.8**, at the steady flow stage there are some shoot ups and downs are reported at different times. These pressure fluctuations occurred at times 0.485 ms and 1.94 ms This error in results has occurred due to element straining of the finite element body. This can be controlled by the removal of strained elements, but the removal of elements causes mass erosion. The finite element model can re-mesh to contradict the problem but it increases solution time. Therefore, the Lagrangian bird model is not much preferred to model a soft body except certain conditions where high accuracy does not matter and consider the reduced computational time and set up time.

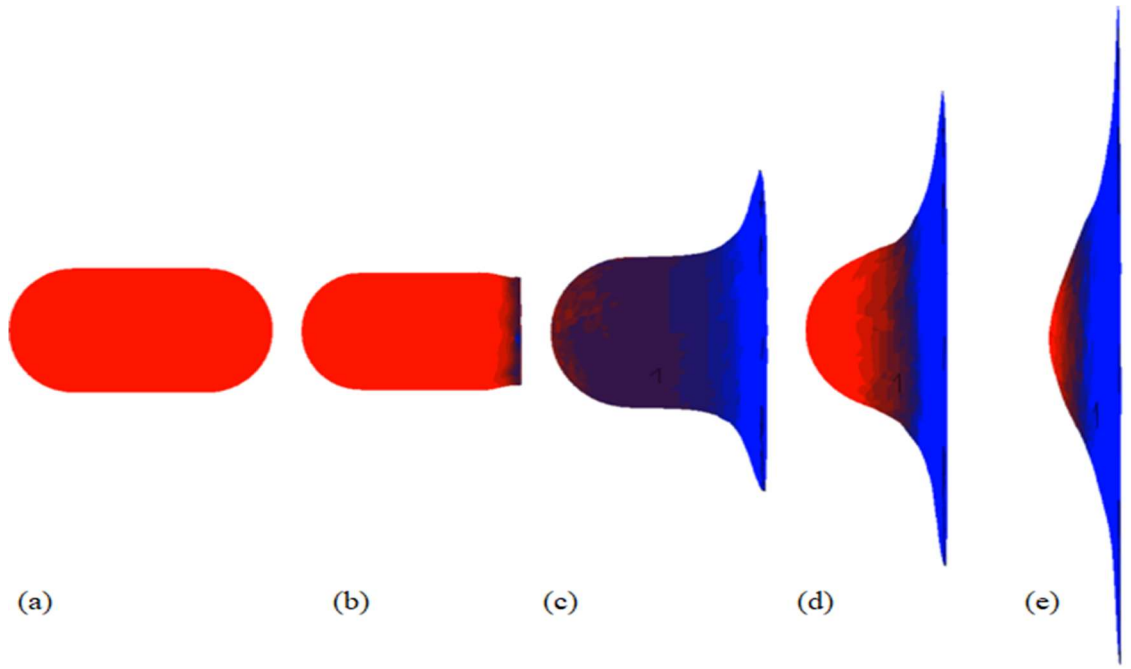

Fig 3.9 Deformation pattern of the Lagrangian soft body at times (a) t=0 ms (b) t=0.5 ms (c) t=1 ms (d) t=1.5 ms (e) t=1.94 ms

3.8.2 Modelling and analysis with Arbitrary Lagrangian-Eulerian (ALE) approach

In ALE modelling the soft body is enclosed in a Eulerian air domain (stationary cube) where the soft body moves freely without distorting the mesh and interacts with the rigid target as shown in **Fig 3.10**. The Eulerian domain filled with air is meshed with very fine size EC3D8R volume elements. The computational time required for the analysis is very high and large computer memory is required store the result data. In the ALE approach, the forces and pressures expended at the time of impact are transferred to the rigid target using general contact algorithms.

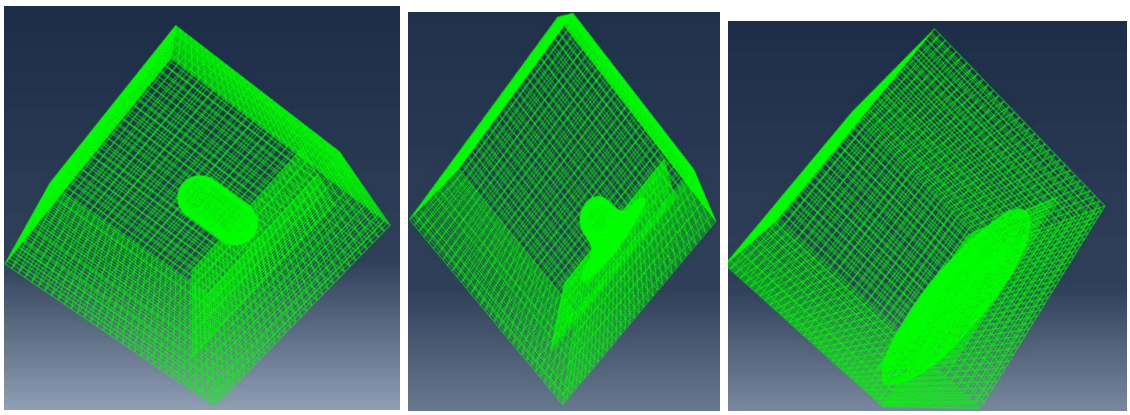

Fig 3.10 Arbitrary Lagrangian-Eulerian soft body impacting on the rigid target

From the comparison of pressure distribution curves in **Fig 3.11**, it is observed that the initial peak pressure curve correlates well with the Wilbeck experiment with an increased Hugoniot pressure. The Hugoniot pressure is noted as 45.37 MPa. It is also observed that the stagnation pressure condition agrees well with the Wilbeck experiment. However, at a normalized time between 0.5 to 1 the contact pressure condition shows leaps and bounds at the stagnated condition. It can be improved by approximating the elements at the end tips of the projectile to fine mesh or using smooth particle hydrodynamic analysis. **Fig 3.12** shows the deformation pattern of the ALE soft body. It has been observed that the material flows without any distortion through the Eulerian domain.

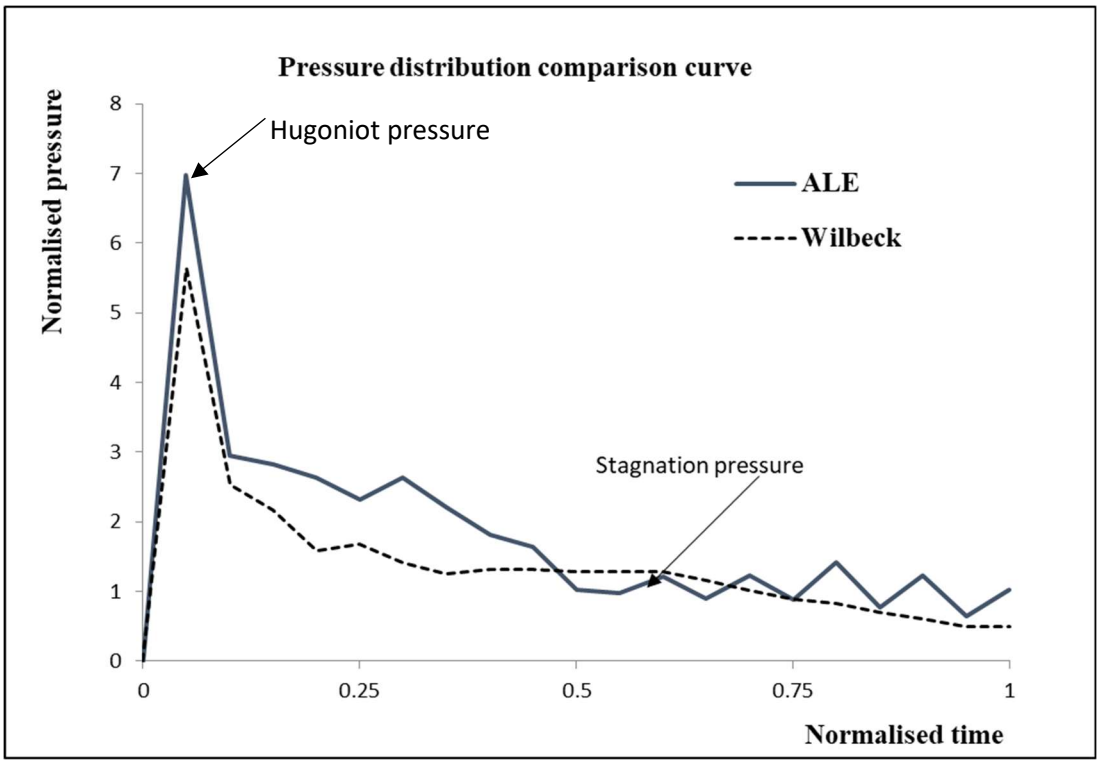

Fig 3.11 Comparison of the pressure profile of ALE soft body model with Wilbeck experiment

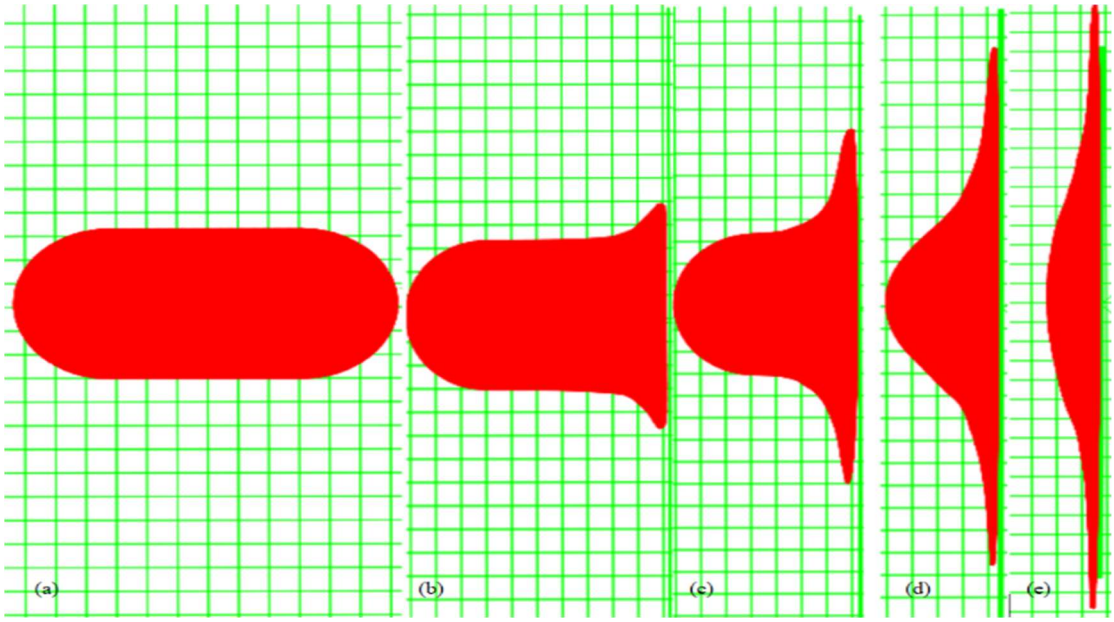

Fig 3.12 Deformation pattern of the ALE soft body at times (a) t=0 ms (b) t=0.5 ms (c) t=1 ms (d) t=1.5 ms (e) t=1.94 ms

3.8.3 Modelling and analysis with Smooth Particles Hydrodynamic (SPH) approach

The Smooth Particles Hydrodynamic method (SPH) is considered as the most efficient and accurate method for modelling of the soft body. The numerical convergence test verified the accuracy of the elements in this specific case where the soft body model impacted the rigid target with a velocity of 117 m/s. For the numerical convergence analysis, the soft body models are discretized with 7829, 10321, 20429 and 60625 solid elements. Then the solid elements are converted into a group of particles that possessed individual material properties. These soft body models are numerically analysed to verify the accuracy of the model with the experiment test. It is observed that the simulated peak pressure came close to a particular value reported by Wilbeck when the total number of elements of the soft body is selected to be 60625. Also, the difference between the predicted peak pressure value and theoretical peak pressure value was less than 1 %. Therefore, the soft body model discretized with 60625 solid elements and then converted into a set of particles. The soft body interaction with the rigid target is governed by the general contact algorithm with the penalty approach. The rigid plate is meshed with 1155 shell elements and is provided with the rigid body constraint command available in the ABAQUS /Explicit. The soft body moving with an initial velocity of 117 m/s impacted on a target is analysed numerically with finite element software ABAQUS /Explicit. The splashing behaviour of the SPH soft body is reduced by scaling down the linear and quadratic bulk viscosity factors. The impact simulation is carried out by impacting the SPH bird model on the rigid target. The CPU time taken to complete the simulation was 7200 sec.

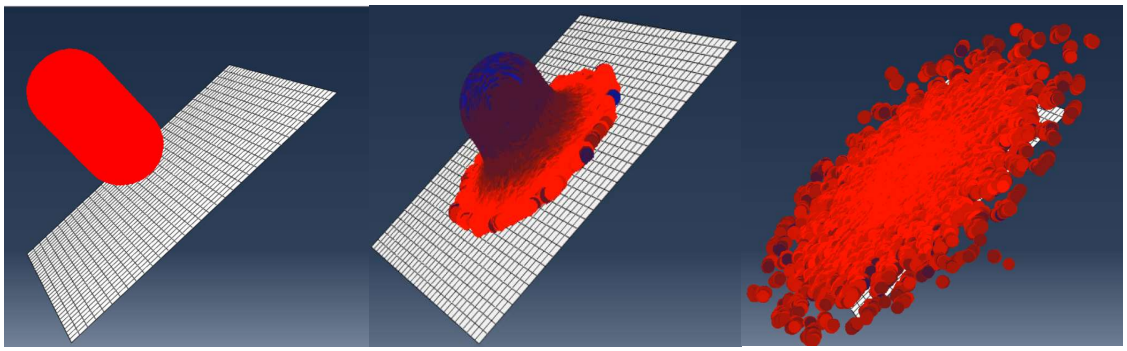

Fig 3.13 Smooth Particles Hydrodynamic (SPH) soft body impacting on the rigid target

After the complete impact of the soft body on the rigid target, the pressure distribution characteristics are predicted numerically to compare with the experimental test data

reported by Wilbeck under the same bird impact conditions. The **Fig 3.13** shows the deformation pattern of the SPH soft body during impact on a rigid target. The results from the analysis of SPH formulation are shown in the normalized pressure versus normalized time using a solid curve in **Fig 3.14.** A dotted curve represents the actual bird strike test results reported by Wilbeck in **Fig 3.14.** The shape of the pressure distribution characteristics in **Fig 3.14** on the soft body model agreed well with experimental test data from Wilbeck at the same impact conditions. The results proved that the projectile pulse predicted by the finite element simulation has a short duration peak pressure at Hugoniot shock. The Hugoniot shock took place at about t_n=0.05, and the values are 44.07 MPa and 37.05 MPa in the simulation and Wilbeck experiment, respectively. After the Hugoniot pressure, the simulated curve closely matches with the Wilbeck experiment result curve. But in simulation, some leaps and bounds are noticed in the curves at normalized times 0.4, 0.5 and 0.7. This is considered to be due to the cluttering of some particles in one location on the rigid target. With **equations (3.4)** and **(3.7),** the theoretical predicted Hugoniot pressure and stagnation pressure are calculated to be 44.57 MPa and 6.5 MPa, respectively. The Hugoniot and stagnation pressure determined from the SPH simulation is observed to be 44.07 MPa and 6.63 MPa (with error ± 4%), respectively. It is concluded that the present SPH simulation using ABAQUS/Explicit is considered to be quantitatively similar with experiment test and able to accurately predict the dynamic contact pressure of a 4 -pound (1.814 kg) real bird normally striking on a rigid target (**Table 3.6**). The deformation behavior at different time steps during transient dynamic contact of the smooth particles hydrodynamic soft body with a rigid plate (**Fig 3.16**) observed qualitatively similar with experiment test (**Fig 3.17**) conducted by Lavoie *et al.* (2009). The outer boundary of the soft body in simulation is not clearly defined as shown in experiment test. Notice that, cluttering of some particles in the outer boundary is shown in **Fig 3.16**. This is a disadvantage of smooth particles hydrodynamics method. The finite element model of the soft body has been validated and strongly recommended to be used for further bird impact studies on aircraft leading edge structures.

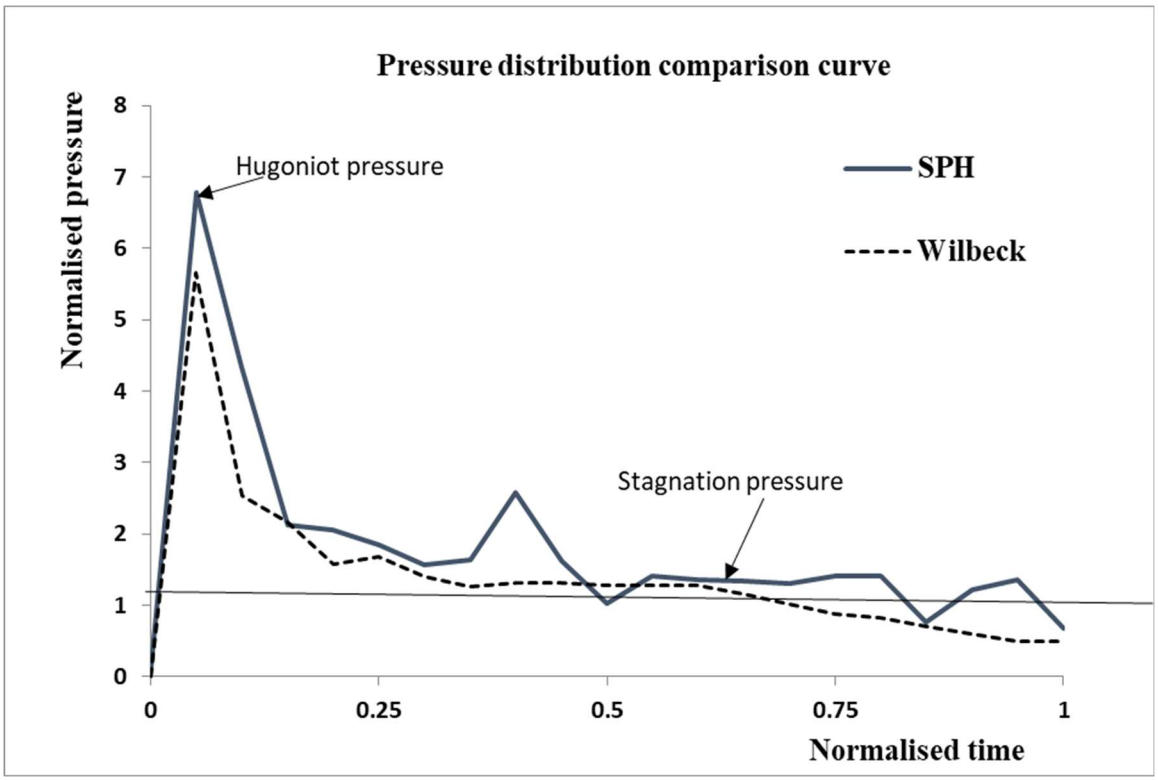

Fig 3.14 Comparison of the pressure profile of SPH soft body model with Wilbeck experiment

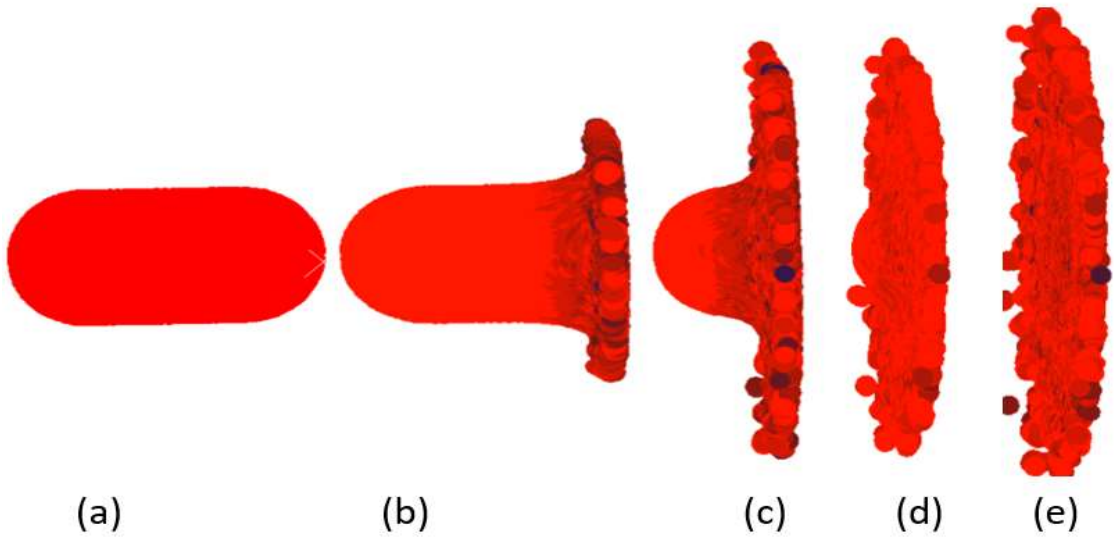

Fig 3.15 Deformation pattern of the SPH soft body at times (a) t=0 ms (b) t=0.5 ms (c) t=1 ms (d) t=1.5 ms (e) t=1.94 ms

Table 3.6 Comparison of pressure distribution data of SPH simulation with experiment and theoretical results

Method	Hugoniot pressure	Stagnation pressure
Simulation	44.07 MPa	6.63 MPa (with error ± 4%)
Experiment	37.05 MPa	6.3 MPa
Theoretical	44.57 MPa	6.5 MPa

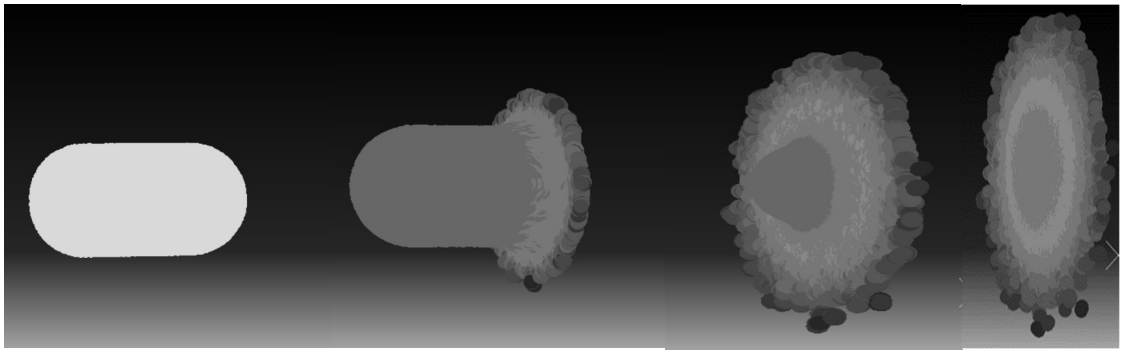

(a) t=0 ms (b) t=0.66 ms (c) t=1.32 ms (d) t=1.98 ms

Fig 3.16 The deformation pattern of the smooth particles hydrodynamic soft body

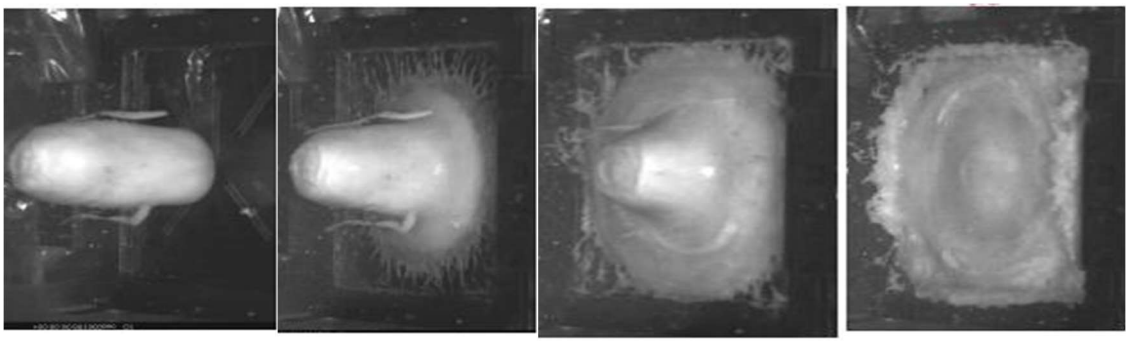

(a) t=0 ms (b) t=0.66 ms (c) t=1.32 ms (d) t=1.98 ms

Fig 3.17 The deformation pattern soft body replacement material impacted on rigid target

[Reprinted from International Journal of Impact Engineering, Vol. 36 (10–11), M. A. Lavoie, A. Gakwaya, M. N. Ensan,D. G. Zimcik, and D. Nandlall, "Bird's substitute tests results and evaluation of available numerical methods," pp. 1276–1287, © 2009, with permission from Elsevier.]

Table 3.7 Relative features of three soft body modelling approaches

Approaches	Advantages	Disadvantages
LAG	• Low FEM formulation time and run time • Low memory requirement • Projectile boundary clearly defined	• High element distortion • Low accuracy • Element erosion reduce mass from simulation
ALE	• Actual fluid like behaviour which correlate well with experiment • Low element distortion • High accuracy	• Very high computational time • Large memory requirement
SPH	• No mesh distortion, • Constant time step • Very high accuracy • Solution time low • Numerically stable • Well represented splashing behaviour	• Difficult in contact formulations and have no clear outer boundary, • Instability in tensile behaviour due to cluttering many particles in one location

Table 3.8 Comparision of three finite element modelling approaches

Method	Set up time (min)	Run time (min)	Normalised Hugoniot pressure	Normalized Stagnation pressure
SPH	100	120	6.78	1.16
ALE	180	540	6.98	1.02
LAG	90	30	7.58	1.64

This chapter studied three equation of state material models and then analysed three different soft body modelling approaches using finite element code ABAQUS/Explicit. The comparison study of the three equation of state material models *i.e.,* Mie-Grüneisen equation of state, Mie-Grüneisen equation of state for multi-material model and user-

defined equation of state have been done. It is found that the Mie-Grüneisen equation of state material model with the given parameters can effectively use to model the soft body material behaviour. The three finite element approaches *viz*, Lagrangian, Arbitrary Lagrangian-Eulerian and Smooth particles hydrodynamics are analysed and compared based on the set-up time, run time, deformation pattern and pressure distribution characteristics. The relative features of the three modelling approaches are explained in **Table 3.7**. The concluded remarks from the finite element modelling and analysis of the soft body impact event with the three approaches explained in this chapter are listed in **Table 3.8**. It is understood that each method has its own advantages and none of these methods are free of disadvantages. However, it is concluded that the SPH method with given equation of state parameters provides the best correlation with the experimental test based on pressure distribution characteristics and deformation pattern. The Hugoniot and stagnation pressure determined from the SPH simulation was observed to be approximately 44.07 MPa and 6.63 MPa (with error ± 4%), respectively**.** Thus, finite element model of the soft body is validated and strongly recommended to be used for further bird impact studies on aircraft leading edge structures.

Chapter 4

Numerical simulation of soft body impact on aluminium alloy wing leading edge

4.1 Introduction

The leading edge of an airplane is the front nose-shaped structure of the wing, vertical or horizontal stabilizer. An aircraft wing is a hollow structure internally reinforced with ribs which are positioned in a perpendicular plane to the wing axis. It generates a lift force and enables the airplane to fly. The leading edge is the front part of the wing and it is particularly designed to redirect the incoming air flux to the bottom of the wing structure. It must be capable to protect the internal wing components from bird strike, hailstone impact, *etc.* The leading edges are required to protect the fuel tank, the control devices and the torsion box from any damage whose performance is required for safe flight. Therefore, any new design of leading edges must satisfy bird strike regulations mentioned by the respective aviation authorities.

The present study is carried out to find the critical material parameters which influence the energy absorbing characteristics of the aluminium alloy used in wing leading edges. The numerical simulation of the soft body impact on wing leading edge utilized the validated soft body projectile model described in chapter 3. The non-penetration of the target has been the criteria to grade impact resistance and energy absorption. For the proper analysis of the results of material parametric study the soft body did not penetrate to the leading edges. Hence, the thickness of the skin was calculated based on the Royal Aircraft Establishment (RAE) (McNaughtan 1972) empirical formulae for penetration velocity. This formula for leading edge skin made in aluminium alloy is given in **equation 4.1.**

$$V_p = 98\tau W^{\frac{-1}{3}} cos^{\frac{-2}{3}} \alpha exp\,[1234(r^2 + 30r + 1000)^{-1}] \quad (4.1)$$

- V_p = Penetration velocity in m/s
- τ = Flat panel / curved panel / leading edge skin thickness in mm
- W = Bird weight in kg
- α = Sweep angle / impact angle in degrees
- r = Leading edge nose radius in mm

The skin thickness is selected of 2 mm based on RAE formula for 1.814 kg bird impacting normally on a leading edge with nose radius 21mm.

4.2 Failure modelling of aluminium alloy

There are lot of material models that can be used to define material behaviour metallic materials. A benchmark study is done by Dede and Altan (2015) on different metallic failure models. The reason for this comparison is to investigate the behaviour of elasto-visco-plastic and elasto-plastic constitutive models on the metallic material. From the view of comparison between different material failure models and available information in the literature, the material behaviour of aluminium alloy is defined with the Johnson-Cook material model (Johnson and Cook 1983). It is a particular type of Mises plasticity model with analytical forms of the hardening law and rate dependence which is suitable for high strain rate deformation of many materials. It is usually used in adiabatic transient dynamic simulations and can be used in conjunction with the Johnson-Cook dynamic failure model in ABAQUS/Explicit. This also can be used in conjunction with the progressive damage and failure model to specify different damage initiation criteria. The damage evolution laws that take into account the progressive degradation of the material stiffness and the removal of elements from the mesh. Johnson-Cook constitutive model combines the material responses that are strain hardening, strain rate effects, and thermal softening. It defines the equivalent von Mises stress ($\bar{\sigma}$) as a function of equivalent plastic strain, equivalent plastic strain rate, and temperature (Iqbal *et al.* 2015; Johnson and Cook 1983).

$$\bar{\sigma} = \left(A + B\varepsilon_p^n\right)\left(1 + Cln\left(\frac{\dot{\varepsilon}_e}{\dot{\varepsilon}_0}\right)\right)\left(1 - \left(\overset{*}{T}\right)^m\right) \quad (4.2)$$

Where A is the static yield limit at the reference temperature, B is the strain hardening modulus, n is the strain hardening exponent, C is the dimensionless strain rate hardening coefficient, and m is the coefficient of temperature softening of the material can be attained from different tensile tests. ε_p is the effective plastic strain, $\dot{\varepsilon}_e$ is the effective plastic strain rate, $\dot{\varepsilon}_0$ is the reference plastic strain rate, and $\overset{*}{T}$ is the homologos temperature which is represented as

$$\begin{cases} 0 & for \;\; T_t < T_r \\ \overset{*}{T} = \frac{T_t - T_r}{T_m - T_r} & for\; T_r \le T_t \le T_m \\ 1 & for \;\; T_t > T_m \end{cases} \qquad (4.3)$$

Where, T_m is the melting temperature, T_r is the reference temperature, and T_t is the test temperature. From the literature (Seidt and Gilat 2013), it has been observed that the rate effects (C, $\dot{\varepsilon}_e$) did not indicate a considerable effect in the ultimate strength and yield strength of the material.

Johnson-Cook failure model for plastic deformation based on the plastic rate and the temperature. Failure criteria defined with three terms combined in a multiplicative manner to include the effects of stress triaxiality, strain rate, and local heating respectively (Ijaz *et al.*2017; Iqbal *et al.* 2015; Johnson and Cook 1985).

This failure criteria shown as

$$D = \sum \frac{d\dot{\varepsilon}_e}{\varepsilon_f} \qquad (4.4)$$

Where, ε_f is the plastic strain at damage initiation.

$$\varepsilon_f = \left[d_1 + d_2 exp\,(d_3 \frac{\sigma_m}{\bar{\sigma}})\right]\left[1 + d_4\, ln\left(\frac{\dot{\varepsilon}_e}{\dot{\varepsilon}_0}\right)\left[1 + d_5 \overset{*}{T}\right]\right] \qquad (4.5)$$

Hillerborg *(*1983) suggested a fracture energy approach to represent damage evolution. If G_f is the failure energy needed to initiation and propagation of a crack then G_f is described as

$$Gf = \int_0^{\bar{u}_f} \sigma_{y\bar{d}u} \qquad (4.6)$$

Where σ_y is the yield strength of the material and $\bar{u}_f$ is the equivalent plastic displacement at fracture

$$\bar{u}_f = \frac{2Gf}{\sigma_f} \quad (4.7)$$

The ductile materials once, the damage initiated for the given loading conditions, the linear or exponential laws can be selected for the damage evolution. The equivalent plastic displacement at fracture ($\bar{u}_f$) and the fracture energy (G_f) are related to the damage variable (D) with following relations (Ijaz *et al.*2017; Zakir *et al.* 2012)

$$D = \frac{\bar{u}}{\bar{u}_f} \quad (4.8)$$

$$D = 1 - exp\left(\frac{\bar{\sigma}}{G_f} d\,\bar{u}\right)$$

The strength parameters used for representing aluminium alloy (AA 2024-T3) are shown in **Table 4.1**. The Johnson-Cook and ductile damage parameters of aluminium alloy (AA 2024-T3) are given in **Table 4.2** and **Table 4.3,** respectively.

Table 4.1 Strength parameters of the aluminium alloy (AA 2024-T3)

(Johnson and Cook 1983)

Strength parameters	Not.	Value	Strength parameters	Not.	Value
Density	ρ	2770 Kg/m^3	Hardening exponent	n	0.34
Poisson's ratio	v	0.33	Thermal softening exponent	m	1
Modulus of elasticity	E	73.1 GPa	Strain rate coefficient	C	0.018
Static yield limit	A	265 MPa	Reference temperature	T_r	293 K
Stain hardening modulus	B	426 MPa	Melting temperature	T_m	775 K

Table 4.2 The Johnson-Cook damage parameters of aluminium alloy (AA 2024-T3)

(Johnson and Cook 1985)

Damage initiation				
d_1	d_2	d_3	d_4	d_5
0.13	0.13	-1.5	0.0011	0

The ductile damage model incorporated in ABAQUS/Explicit is used to define damage initiation criteria (Seidt and Gilat 2013). This failure model for plastic deformation includes the product of failure strain, stress triaxiality and strain rate.

Table 4.3 The ductile damage parameters of aluminium alloy (AA 2024-T3)

(Johnson and Cook 1985)

Damage initiation		
Fracture strain	Stress triaxiality	Strain rate
0.13	-1.5	0.0011/s

This study has compared the efficiency of Johnson-Cook damage model and ductile damage model and found that ductile damage model is easier to implement to study the damage and failure of aluminium alloys.

4.3 Soft body impact simulation on wing leading edge

The numerical simulation of soft body impact on aluminium alloy (AA 2024-T3) wing leading edge is validated with an experimental test under same impact conditions. As per FAR regulation, a soft body model with a mass 1.814 kg striking at velocity 112 m/s has been considered for the testing of 2 mm thick aluminium alloy leading edge (Kavitha and Stanley 2011). The velocity of the bird impact for testing is estimated as per FAR regulations based on leading edge thickness, and other parameters under consideration. Non-penetration of the leading edge skin by the soft body is considered as the criterion of resistance.

For simulation, the aluminium wing leading edge is modelled and meshed with 4800 S4R shell elements using finite element software Altair ® Hyper mesh®. Then, this leading edge model is imported to ABAQUS/Explicit for soft body impact simulation. The contact definition between the soft body and wing leading edge is selected as general contact with the pure master-slave approach. The soft body is considered as a slave surface as the bird surface is smaller than leading edge surfaces. The damping coefficient of 0.02 is used for contact damping. The time required for full impact is calculated by dividing the total length of the soft body by the initial impact velocity. The calculated time for complete impact for the velocity 112 m/s was 2.035 seconds.

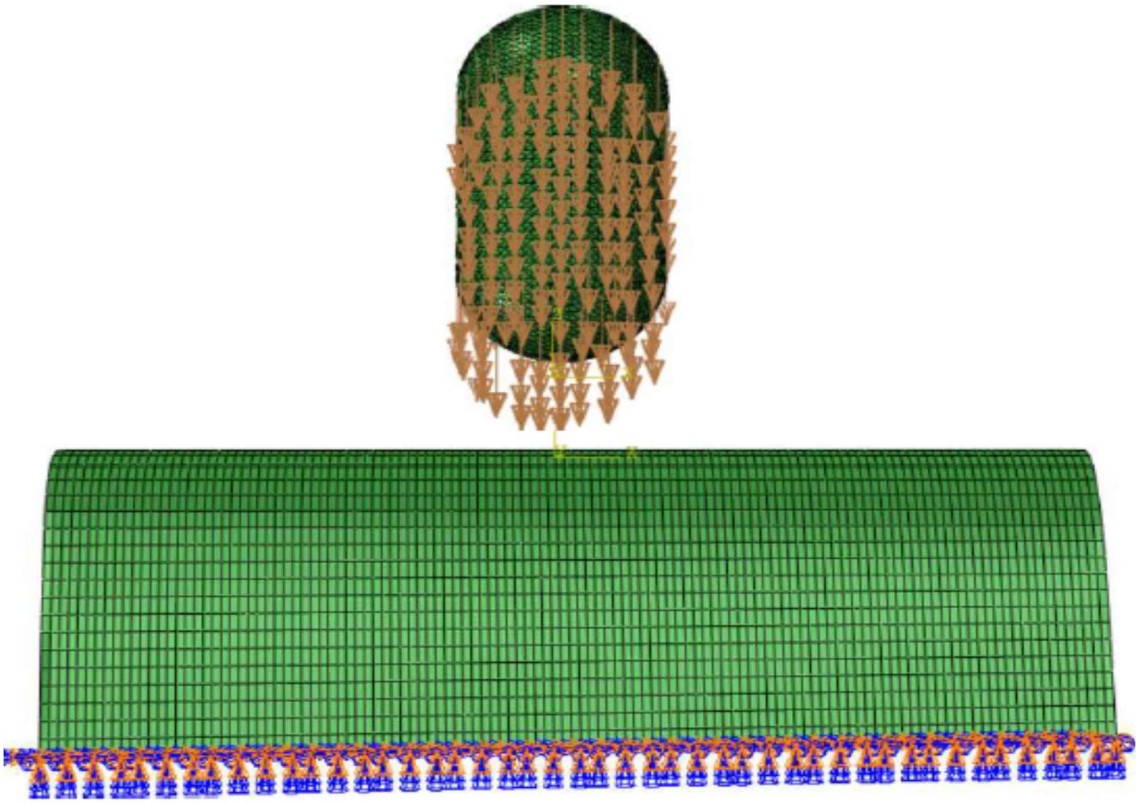

Fig 4.1 Finite element model of soft body impact on wing leading edge which explain mesh pattern, loading and boundary conditions

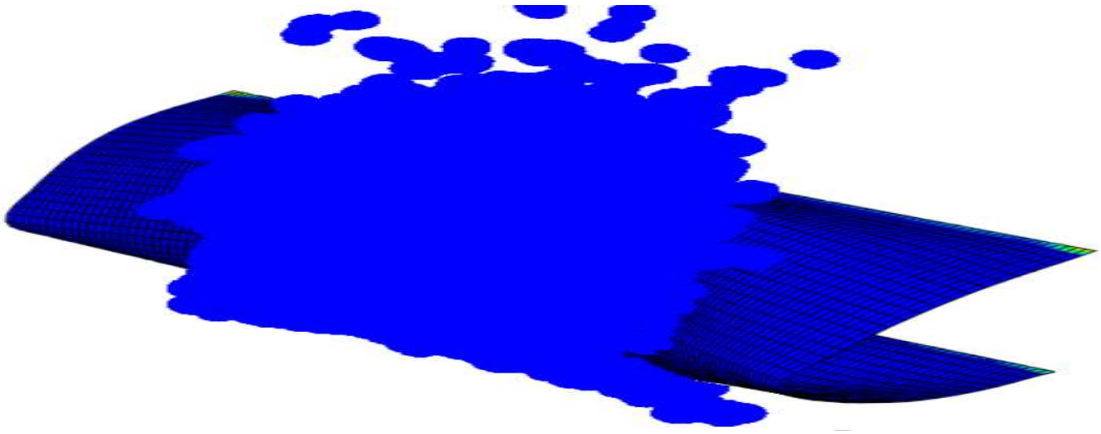

Fig 4.2 The deformation pattern of the soft body and wing leading edge after complete impact

As per FAR requirements, the damaged structure must capable to bear the static loads (ultimate loads) which are fairly anticipated to occur on the flight. Dynamic effects on these static loads need not be considered. Therefore, the boundary is rigidly supported

both in the experiment test and in the analysis. Such geometric constraints reduce the number of degrees of freedom which can significantly reduce the computational time for analysis. The finite element model explaining loading and boundary conditions explained in **Fig 4.1.**

The validated SPH soft body model is made to impact in a normal direction on to the wing leading edge model with a velocity of 112 m/s. The deformation pattern soft body and wing leading edge after impact is shown in **Fig 4.2.** The displacement contour plots of the wing leading edge at different times of soft body impact are shown in **Fig 4.3**. The centre tip deformation of the leading edge over this time duration was recorded 109.2 mm in numerical simulation.

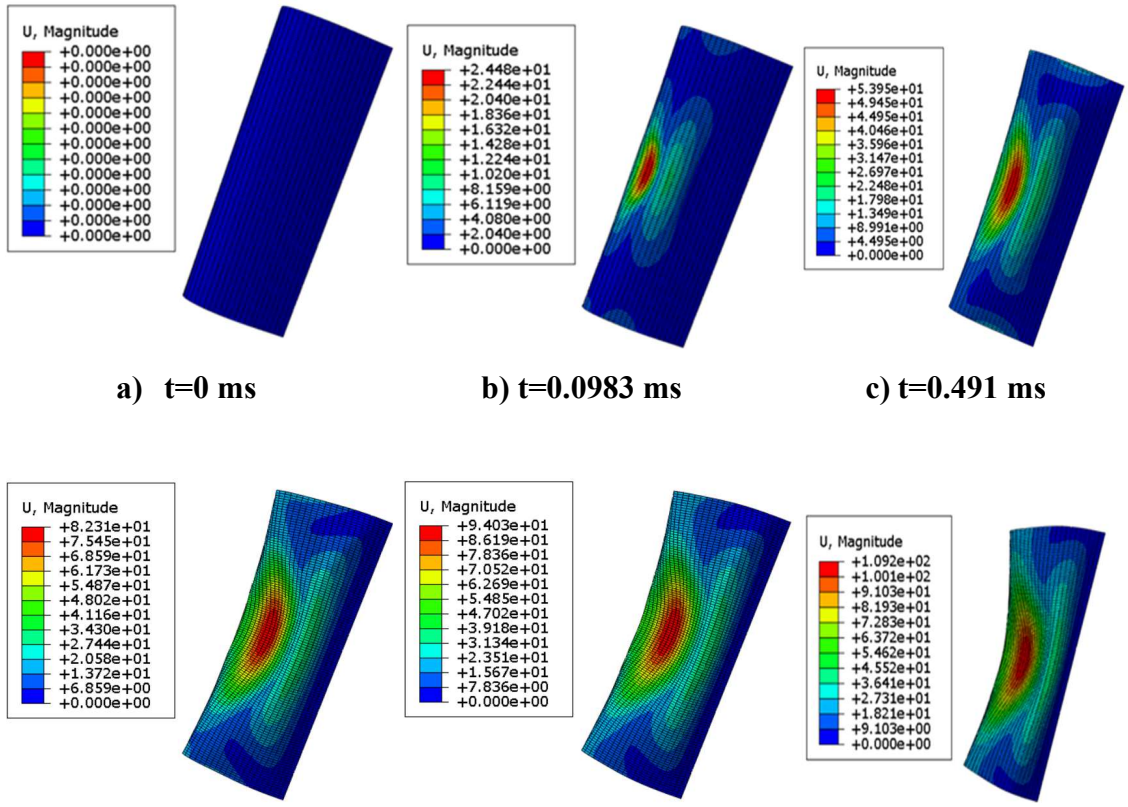

a) t=0 ms **b) t=0.0983 ms** **c) t=0.491 ms**

d) t=1.47 ms **e) t=1.82 ms** **f) t=2.035 ms**

Fig 4.3 Displacement contour plot of wing leading edge at different times of soft body impact

4.4 Experimental validation of soft body impact on wing leading edge

The experimental test has been conducted under real bird strike conditions by impacting a 4-pound (1.814 kg) gelatine pack with a velocity of 112 m/s on an aluminium alloy (AA 2024-T3) wing leading edge specimen. The wing leading edge skin has been fabricated at National Aerospace Laboratories, Bangalore and an experiment test has been conducted at Gas Turbine Research Establishment, Bangalore (Kavitha and Stanley 2011). **Fig 4.4** shows the profile of the leading-edge specimen fabricated at National Aerospace Laboratories. **Fig 4.5** shows the profile of the leading edge when subjected to impact with 4-pound (1.814 kg) gelatine with a velocity of 112 m/s.

Fig 4.4 The profile of aluminium alloy (AA 2024-T3) wing leading edge before soft body impact experimental test

[Reprinted from Journal of Aerospace Engineering, Vol. 35 (4), Kavitha mol, S., Stanley C. Salem and Sadiq, A. "Crashworthiness enhancement of aluminium alloy used for leading edges of wing and empennage structures," pp. 04022079, © 2022, with permission from American Society of Civil Engineers]

Fig 4.5 The profile of aluminium alloy (AA 2024-T3) wing leading edge after soft body impact experimental test

[Reprinted from Journal of Aerospace Engineering, Vol. 35 (4), Kavitha mol, S., Stanley C. Salem and Sadiq, A. "Crashworthiness enhancement of aluminium alloy used for leading edges of wing and empennage structures," pp. 04022079, © 2022, with permission from American Society of Civil Engineers.]

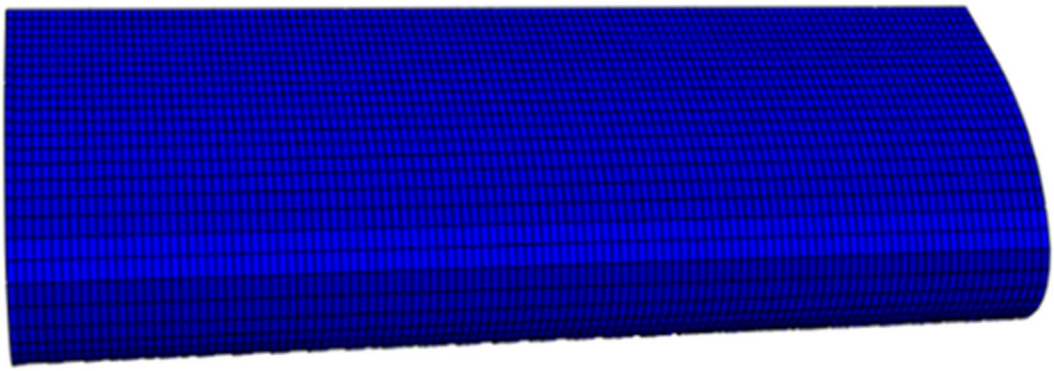

Fig 4.6 The profile of aluminium alloy (AA 2024-T3) wing leading edge before soft body impact simulation

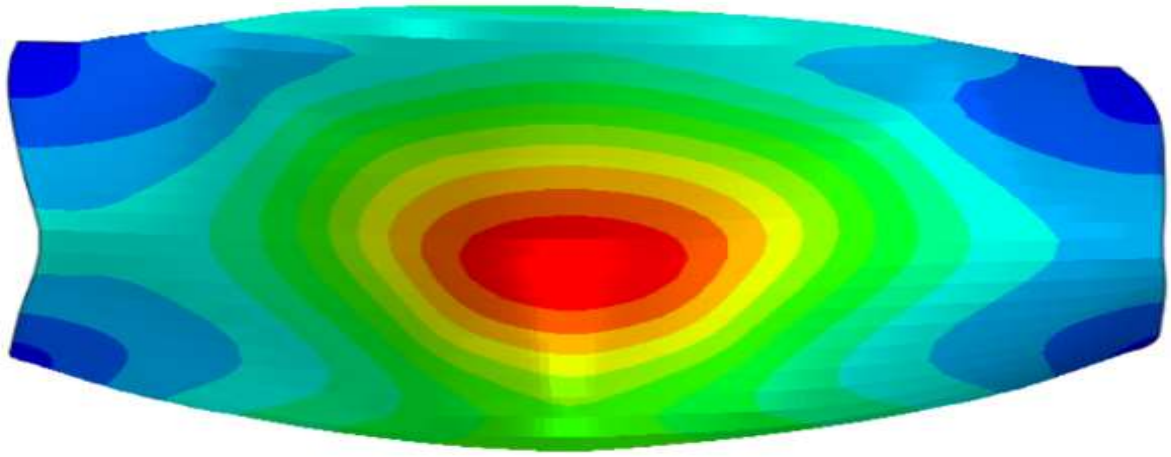

Fig 4.7 The profile of aluminium alloy (AA 2024-T3) wing leading edge after soft body impact simulation

No failure is observed, when the leading edge specimen is impacted with a 4-pound (1.814 kg) gelatine pack at a velocity of 112 m/s. The permanent plastic deformation of the wing leading edge specimen in experiment (**Fig 4.5)** is observed as seen in the simulation (**Fig 4.7)**. When impacted at velocity 112 m/s, the soft body broke up into particles and has not experienced any stability problem. The deformed profile of the leading edge after complete impact showed good agreement in experimental test and simulation, as shown in **Fig 4.5** and **Fig 4.7**, respectively. Thus, the finite element model of the soft body impact on the wing leading edge is validated. The smooth particles hydrodynamic soft body model is demonstrated to be very effective for modelling soft body impact on wing leading edges. The experiment test validated the soft body impact behaviour of the aluminium alloy wing leading edge predicted by finite element analysis. In the next chapter, a material parametric study is carried out by varying the target parameters, with the validated soft body model and wing leading edge model to find the most influenced parameters and range of values that can control the energy absorbing characterisitcs of aluminum alloy.

Chapter 5

Soft body impact simulations on leading edges for material parametric analysis

5.1 Introduction

The leading edges of wing and empennage structures are the foreparts of the aircraft and are always under the possibility of a bird strike. The foreign object impact leads to serious damages to the front-facing components such as the wing, horizontal stabilizer, and vertical stabilizer and affects its components, *viz*. control rods, control surfaces like the elevator, and rudder respectively. Consequently, besides to the aerodynamic functions, a leading edge should safeguard the supporting spars and control surfaces from such impact damages. Therefore, careful design is vital that minimize centre displacement and maximize the energy absorption that must ensure the protection of internal sensitive components during an impact. An impact event can be structurally analysed built on two aspects. One is the behaviour of the material/structure at the time of impact and the other is their residual properties. The behaviour of a structure in the impact and its post impact performance reliant on both the impactor and the target characteristics. The leading edge parameters which affect the impact characteristics include the boundary conditions, the structural configuration, the materials, and its properties. The leading edge structural parameters that generally affect are the rib spacing, skin thickness, leading edge skin material/configuration, position of the baffle, the baffle properties, rib properties, boundary condition between the skin and spar, *etc.* (Stanley *et al.* 2011).

The leading edge skin is the most critical part of the wing structure as it has a higher probability of affecting the impact first. Therefore, the skin material must have the property to absorb a significant portion of the incident impact energy, thereby transferring lesser load to the supporting structures. Moreover, deformation of the leading edge also must be

reduced to safeguard the internal wing components. Optimization of the material parameters of the skin help improve the mechanical properties of the leading edges against soft body impact. Finite element simulations of these impact events help reduce the time and cost to optimize the design before a full-scale certification test.

The 2xxx series aluminium alloys are considered as candidate material for leading edge skin as it has high failure strain compared to other aluminium alloys. The parametric study on material parameters is required to identify the important parameters which influences the energy absorption capability and load transferability during bird strike. The elastic and flow stress parameters show great importance in the mechanical property optimization of aluminium alloy used in wing leading edges. Therefore, its study and optimization help to adjust the strength and toughness of the material with various process conditions. In this aspect, a parametric study can help in identifying the material parameters which influence the impact behaviour of the leading edges. Parametric analysis can be performed using different target material parameters and understanding its influence can be useful to tailor the type of metal to improve its mechanical properties. The parametric study has been carried out on leading edges of wing and empennage structures.

To develop a new alloy or to improve the properties of the present alloy used for a particular aircraft component, it needs to define the property requirements based on the different loading conditions (Dursun and Soutis 2014). The critical loading condition of the wing leading edge is considered due to bird strike and its design requirements as per regulations against bird strike loading conditions. The properties required to meet the design requirements can be obtained by optimizing the alloy compositions and processing conditions (Pantelakis and Alexopoulos 2006). Hence, an aircraft structural designer must work together with a material producer to tailor the mechanical properties of the metallic alloys as per the specific requirements. The improvement of finite element packages and optimization software introduces a new era in the design of alloys based on the requirements and the ways to find the optimized property balance. The aircraft designers also aim to decrease the number of parts while improving the energy absorption capabilities of the material (Starke and Staley 1999).

This chapter aims to find the influence material parameters on energy absorbing characteristics of aircraft wing leading edges. A material combination parametric study is undertaken to understand the role of the target parameters (material parameters of skin only) which influences the bird impact. The significant material parameters which

influence the bird impact behaviour of leading edges is selected from the elastic and flow stress parameters which define the material. The range of which each parameter values are varied depending on the properties of the fibre metal laminate which can develop for a leading edge. Based on the literature review and detailed survey with material producers, a range of material parameters are selected that can vary without compensating the mechanical property requirements of the particular aircraft component.

5.2 Material parametric analysis

The material parametric analysis is carried out on the leading edges of wing and empennage structures. The model of the selected leading edges *i.e.,* HT VT and wing are shown in **Fig 5.1**.

Table 5.1 Parametric study test matrix

Variable Parameter	Constant parameter
Elastic modulus (40 GPa, 50 GPa,60 GPa, 70 GPa, 80 GPa)	Strain hardening modulus (426 MPa), Hardening exponent (0.34), Static yield limit (265 M Pa), Poisson's ratio (0.33).
Strain hardening modulus (300 MPa, 350 MPa, 426 MPa, 457 MPa, 460 MPa, 480 MPa, 500 MPa)	Hardening exponent (0.34), Static yield limit (265 MPa), Poisson's ratio (0.33), Elastic modulus (70 GPa).
Hardening exponent (0.34,0.45,0.5,0.6)	Static yield limit (265 MPa), Poisson's ratio (0.33), Elastic modulus (70 GPa), Strain hardening modulus (426 MPa).
Static yield limit (180 MPa, 265 MPa, 313 MPa, 338 MPa, 359 MPa)	Poisson's ratio (0.33), Elastic modulus (70 GPa), Strain hardening modulus (426 MPa), Hardening exponent (0.34).
Poisson's ratio (0.2, 0.22, 0.24, 0.26, 0.28, 0.3. 0.33)	Elastic modulus (70 GPa), Strain hardening modulus (457 MPa), Hardening exponent (0.34), Static yield limit (265 MPa).

The models of the leading edges are created and meshed in finite element software Altair ® Hyper Mesh ®. The S4R shell elements are used to mesh the leading edge models. The parameters and the values selected for the study is detailed in the **Table 5.1.** The values are selected in a wide range to specifically analyse the interdependence of parameters. Python

scripting algorithms is explored to effectively carry out the parametric studies which helped for analysis with varying parameters in a single run command. These algorithms are generated to automize the repeated tasks in a parametric study and to reduce the required pre and post processing time. The scripting algorithms are written as per the parametric study test matrix in **Table 5.1.** The scripting algorithm also helped a great extent is reducing the time required for analysis. Then soft body impact simulations are carried out on the leading edges (HT, VT and wing) by impacting the soft body model with a velocity of 116 m/s. 190 cross-correlation analysis studies between the parameters carried out to understand the interdependence on the other parameters.

5.3 Results and discussion

The results are analyzed based on the average reaction force at constrained nodes and wing centre nose tip deformation recorded after the soft body impacted on the leading edges with a velocity of 116 m/s. **Fig 5.2** shows the reaction force and time curve of the leading edges of the wing, HT and VT, respectively. **Fig 5.1, Fig 5.2,** and **Fig 5.3** displayed the reaction force contour plots of the leading edges of wing, HT and VT, respectively. From this contour plots, it could understood that at intial impact the reaction force occurred in all the constrained nodes. When the time increased the reaction force concentrated at the end nodes and after full impact it has been completely localized at the end nodes.

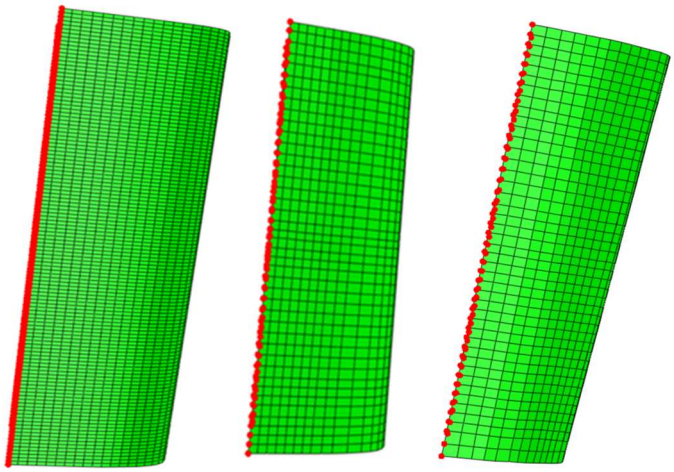

Fig 5.1 Undeformed mesh overlaid plot of Wing, VT and HT which explains the location of constrianed nodes

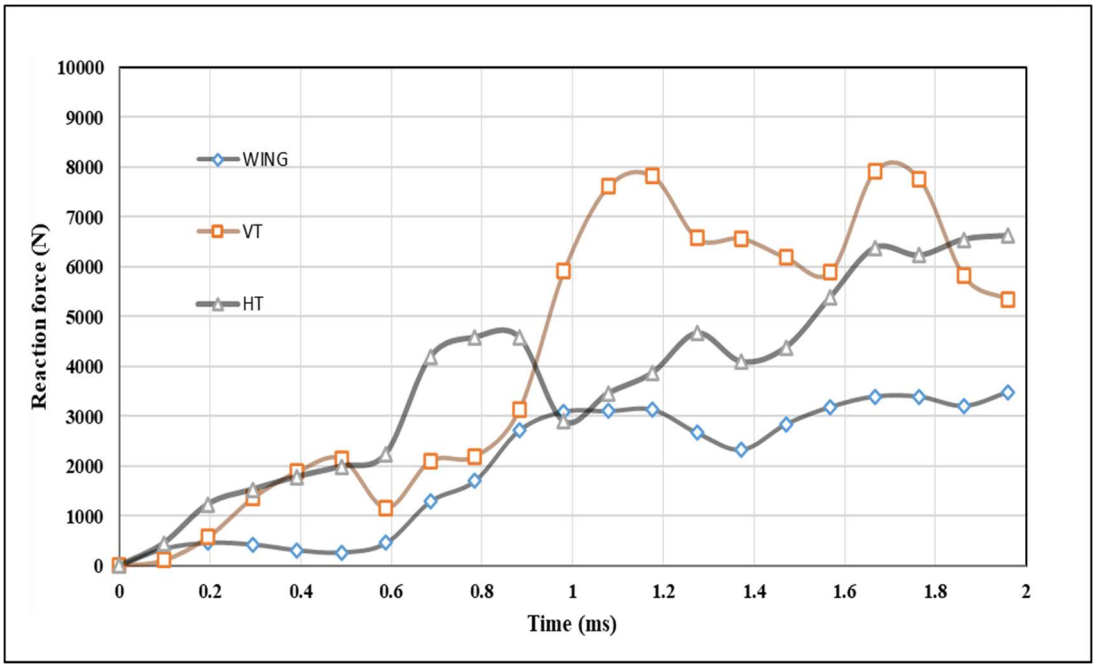

Fig 5.2 The reaction force versus time plot of wing, VT and HT

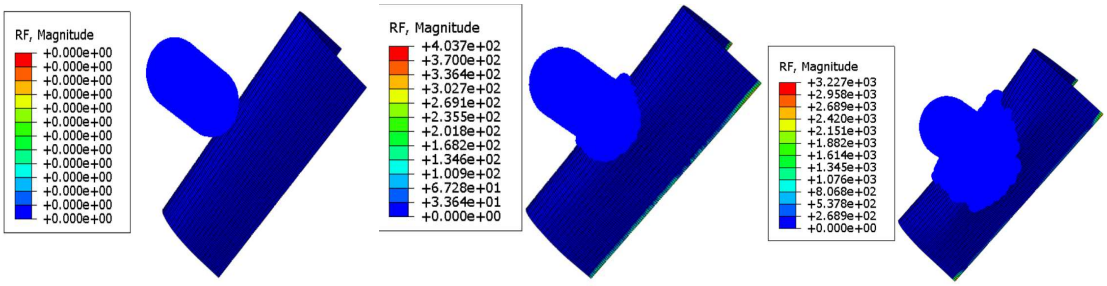

a) t = 0 ms **b) t = 0.49 ms** **c) t = 0.98 ms**

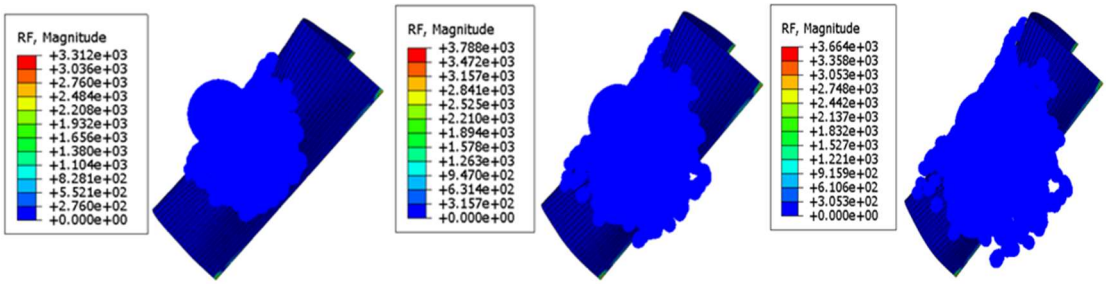

d) t = 1.27 ms **e) t = 1.66 ms** **f) t = 1.96 ms**

Fig 5.3 The reaction force contour plot of wing leading edge profile at different times

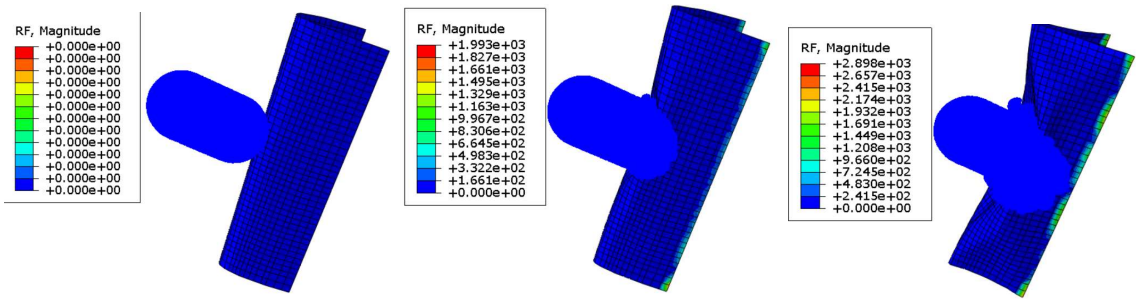

a) t = 0 ms **b) t = 0.49 ms** **c) t = 0.98 ms**

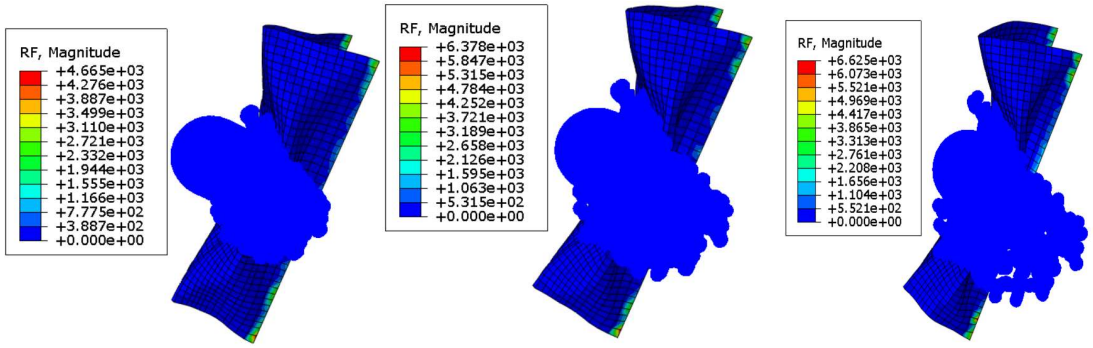

d) t = 1.27 ms **e) t = 1.66 ms** **f) t = 1.96 ms**

Fig 5.4 The reaction force contour plot of HT profile at different times.

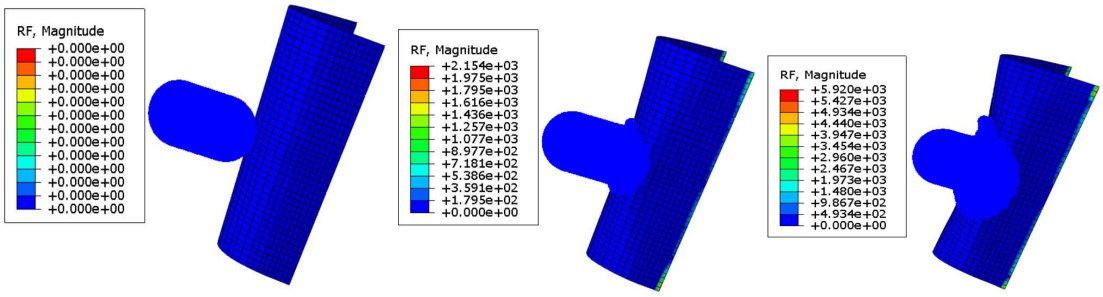

a) t = 0 ms **b) t = 0.49 ms** **c) t = 0.98 ms**

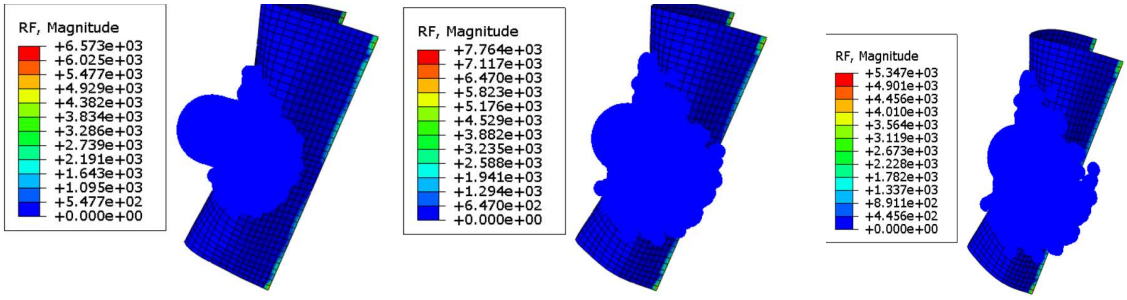

d) t = 1.27 ms **e) t = 1.66 ms** **f) t = 1.96 ms**

Fig 5.5 The reaction force contour plot of VT profile at different times

The parametric study results at different material combinations and profiles are described below.

5.3.1 Elastic modulus

The effect of the reaction force and centre tip deformation is investigated for different leading edge profiles, *i.e.,* HT, VT and wing. The fluctuations of the average reaction force at support (***RF***) and centre node deflection (***U***) are investigated with distinct readings of strain hardening modulus, hardening exponent and static yield limit. The various studies of the reaction force and centre node deflection with elastic modulus are shown in **Fig 5.6** and **Fig 5.7**, respectively. The deviation of the selected variables (reaction force and center displacement) with the variation of its elastic modulus are consequent with change in strain hardening modulus, hardening exponent and static yield limit. The variables showed good influence when static yield limit and strain hardening modulus are changed. In the case of HT and VT profile, at standard bird impacting velocity (116 m/s), when the elastic modulus increased, the reaction force has also been increased. But at the same time, centre node deflection has gradually decreased. In the wing leading edge with an increase of elastic modulus, the reaction force also increased up to a point after that it got decreased. A cross-correlation study is carried out on leading edge wing profile with other material parameters, *i.e.,* varying the elastic modulus value (40 GPa, 50 GPa,60 GPa, 70 GPa, 80 GPa) with constant values of strain hardening modulus (426 MPa), hardening exponent (0.34), static yield limit (265 MPa), Poisson's ratio (0.33) in one correlation. In the next correlation, one parameter changed with keeping all other parameter values constant, *i.e.,* strain hardening modulus is changed from 426 MPa to 457 MPa while keeping all other parameter values constant. The results summarized that the elastic modulus value of 70 GPa provided a variation in selected variables than other values.

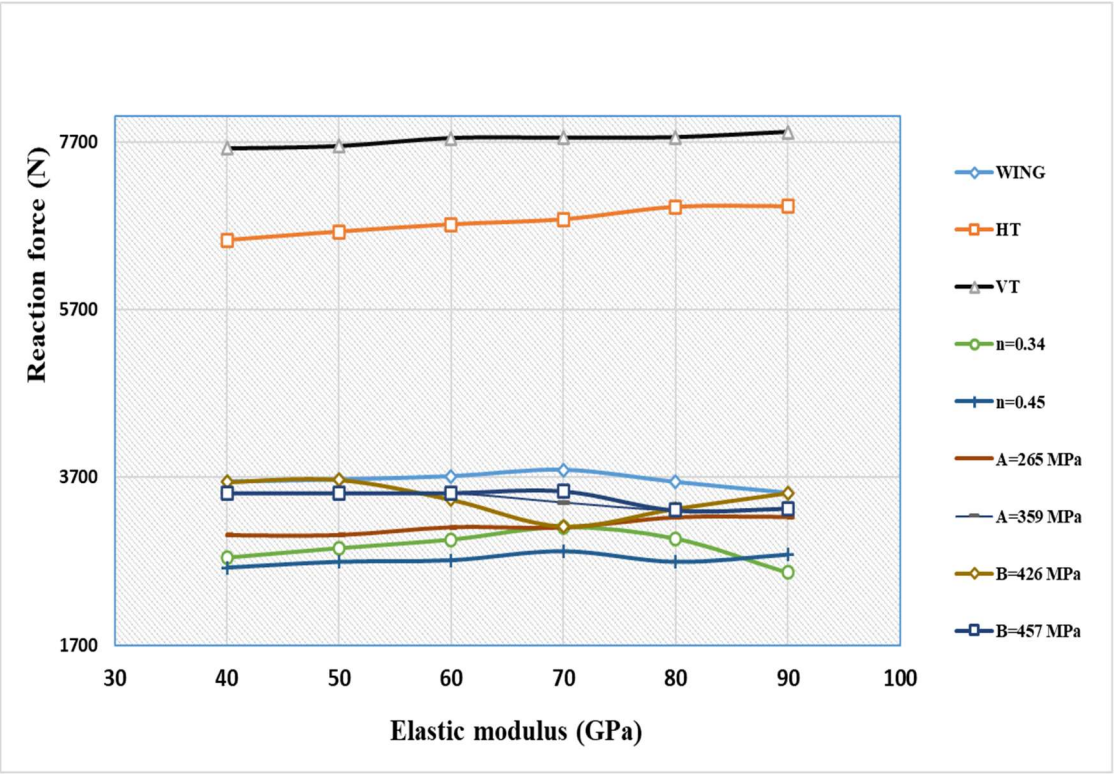

Fig 5.6 Variation of the reaction force with elastic modulus for different leading edge profiles and material parameters

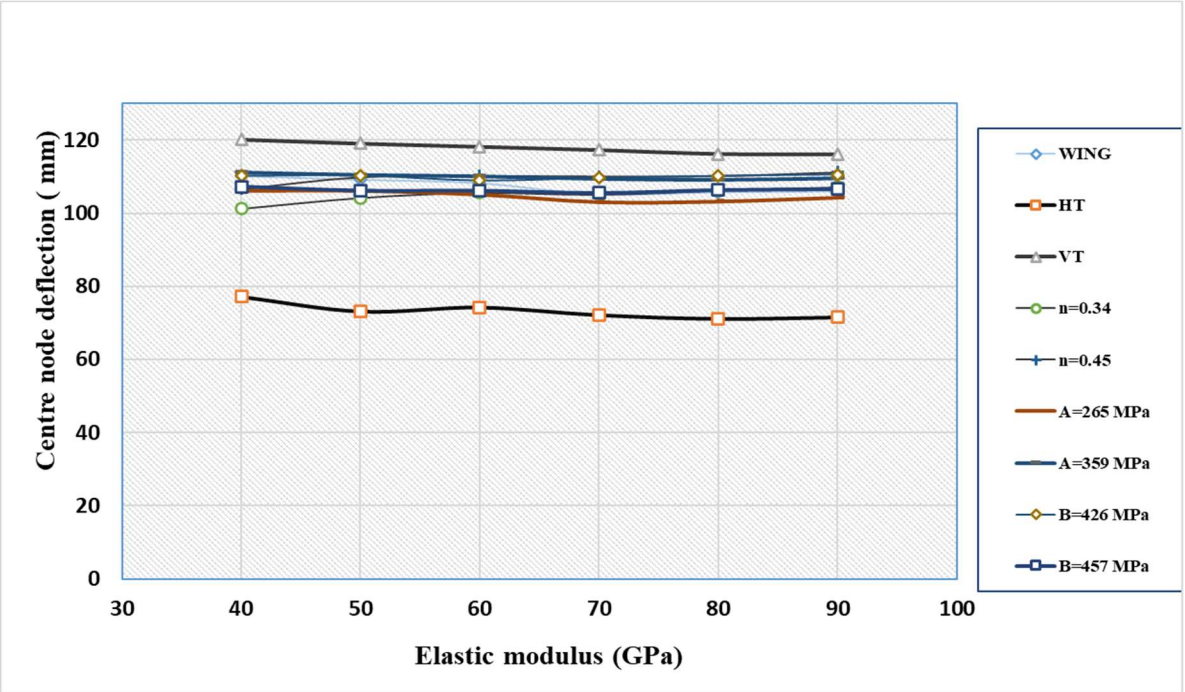

Fig 5.7 Variation of the and centre deflection with elastic modulus for different leading edge profiles and material parameters

5.3.2 Static yield limit

The results shown in **Fig 5.8** and **Fig 5.9** indicate that the static yield limit is an influencing parameter upon selected variables (***RF*** and ***U***) when subjected to soft body impact.In all the three profiles ,the reaction force has increased when the static yield limit increased. The two responses (***RF*** and ***U)*** showed an inverse relationship, while one response decreased the other response increased and vice versa. From cross-correlation study with other variables, it is concluded that the selected variables can reduce in variation with other parameters through an optimization study.

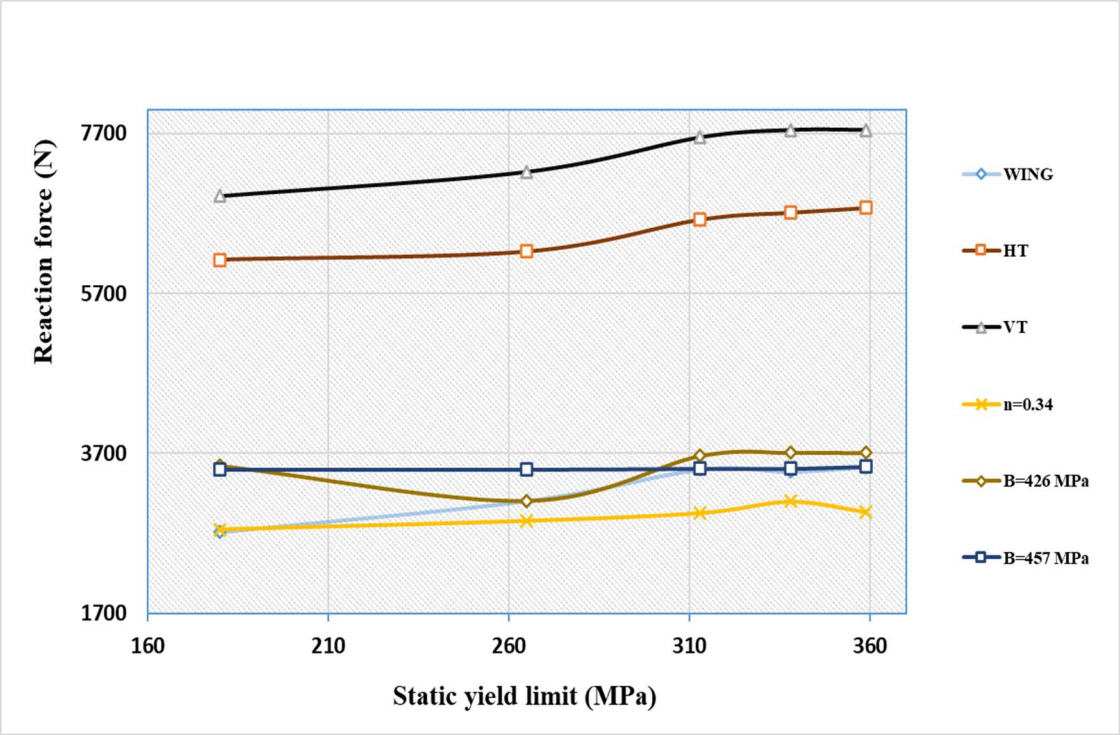

Fig 5.8 Variation of the reaction force with static yield limit for different leading edge profiles and material parameters

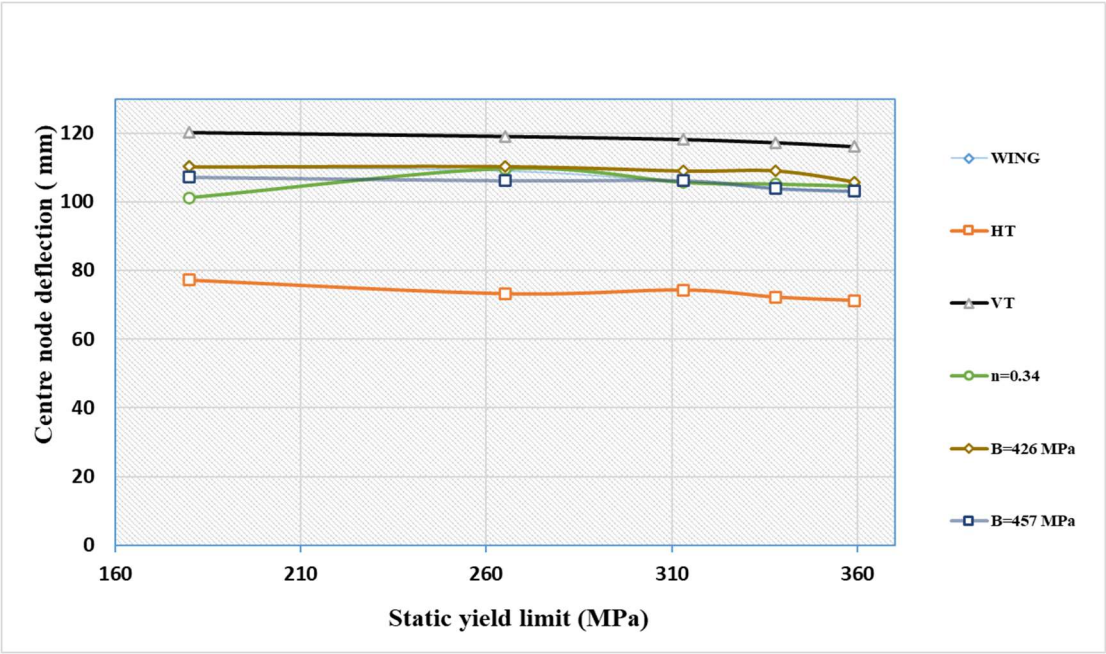

Fig 5.9 Variation of the centre deflection with static yield limit for different leading edge profiles and material parameters

5.3.3 Strain hardening modulus

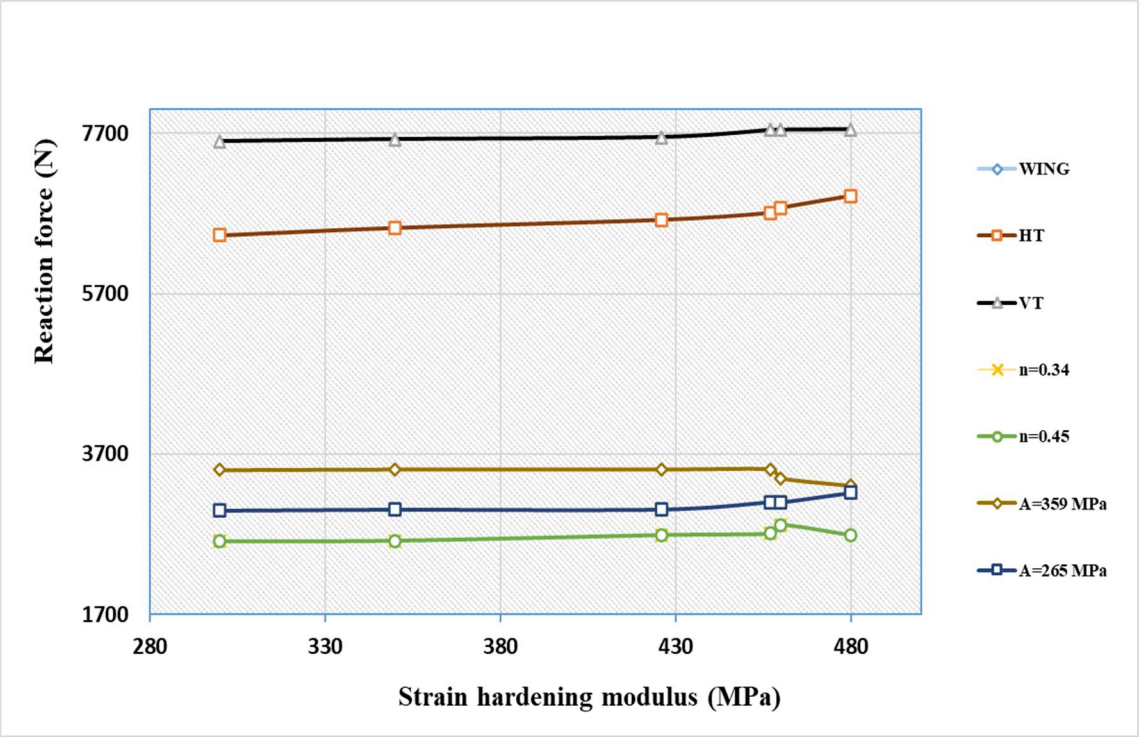

Fig 5.10 Variation of the reaction force with strain hardening modulus for different leading edge profiles and material parameters

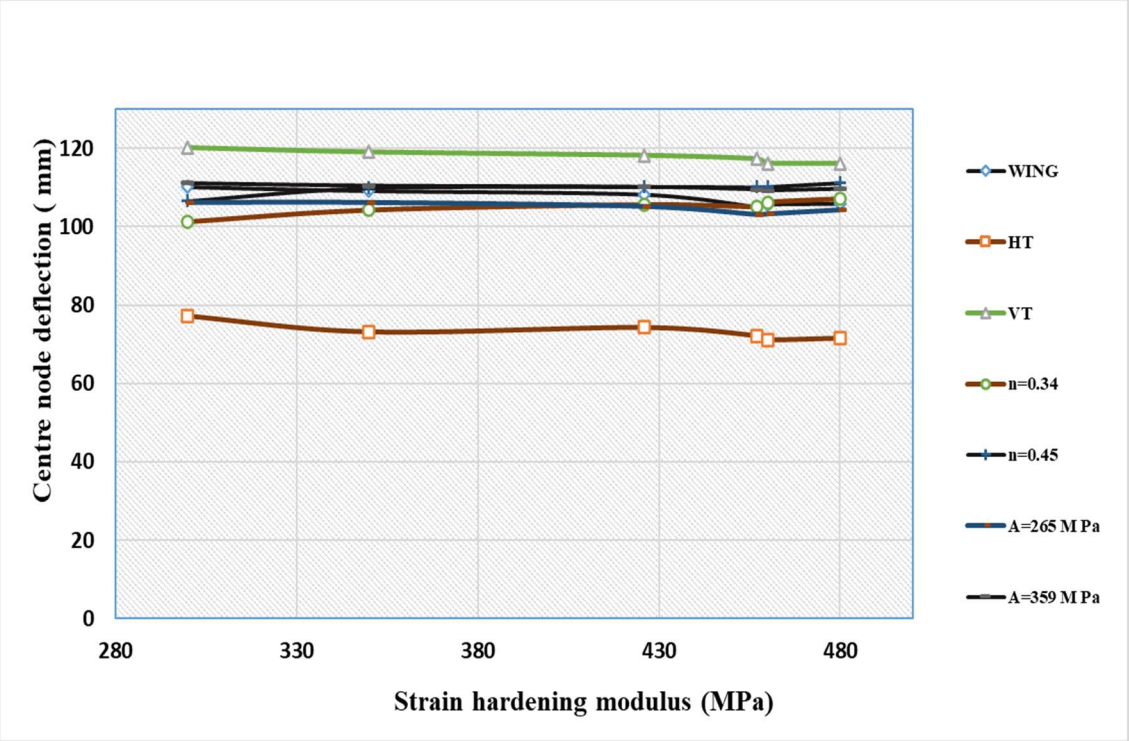

Fig 5.11 Variation of the centre deflection with strain hardening modulus for different leading edge profiles and material parameters

The effect of selected variables (***RF*** and ***U***) has been investigated on the variation of strain hardening modulus with different leading edges and material parameters, and the results are shown in **Fig 5.10** and **Fig 5.11.** The reaction force and centre displacement showed almost constant values up to 426 MPa. The reaction force has increased while the centre displacement has gradually decreased between the values of 426 MPa and 480 MPa. A variation in selected variables is reported around the strain hardening modulus value of 457 MPa on the variation of other material parameters.

5.3.4 Hardening exponent

From the results shown in **Fig 5.12** and **Fig 5.13**, it is clear that hardening exponent does not have much influence on selected variables on the variation of other material parameters. When the hardening exponent increased, the reaction force has also increased while the centre deformation decreased. The same result has been reported in all leading edge profiles.

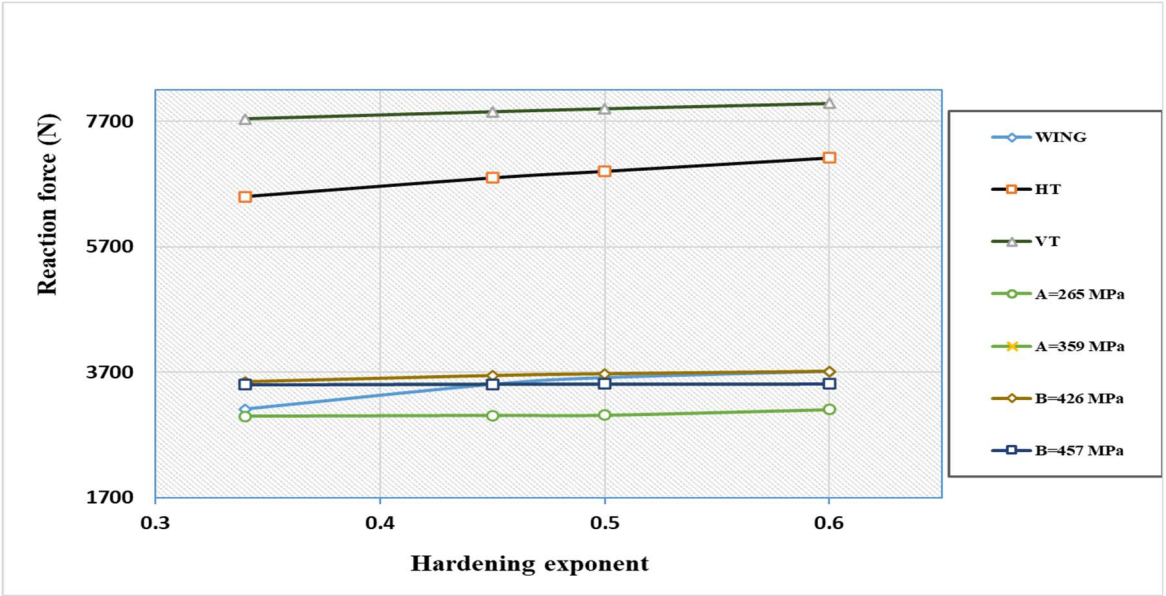

Fig 5.12 Variation of the reaction force with hardening exponent for different leading edge profiles and material parameters

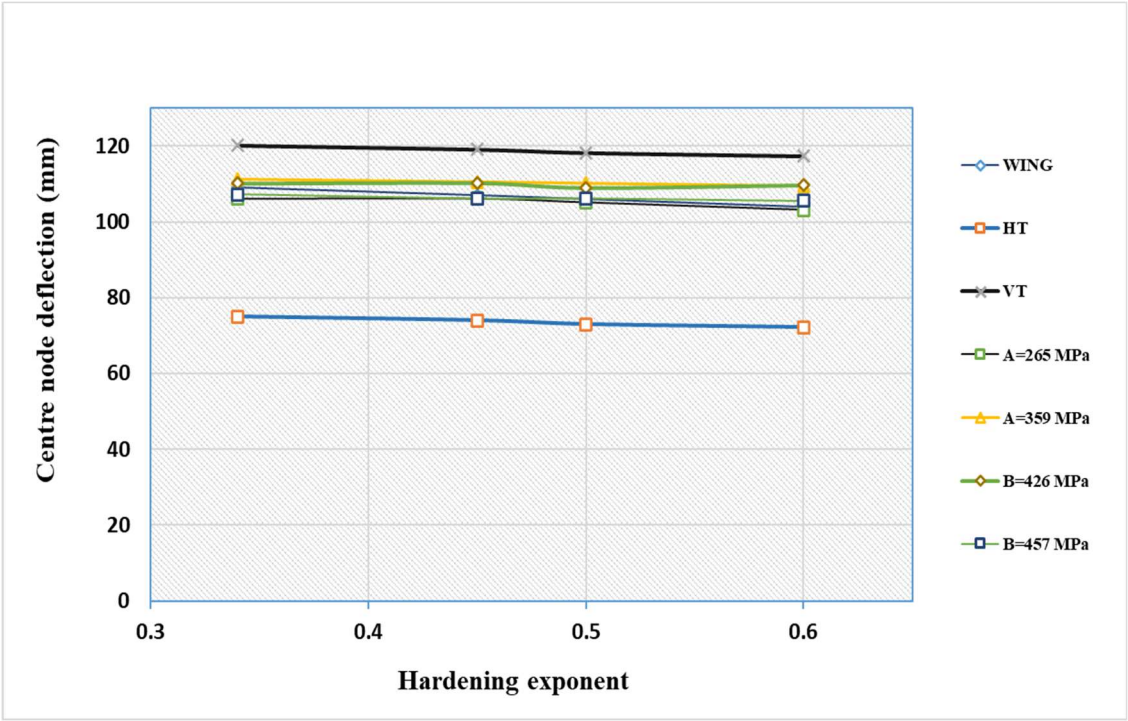

Fig 5.13 Variation of the centre deflection with hardening exponent for different leading edge profiles and material parameters

5.3.5 Poisson's ratio

The variation of Poisson's ratio didn't provide much influence on the selected variables, and the same pattern has shown in different leading edges as shown in **Fig 5.14** and **Fig 5.15.**

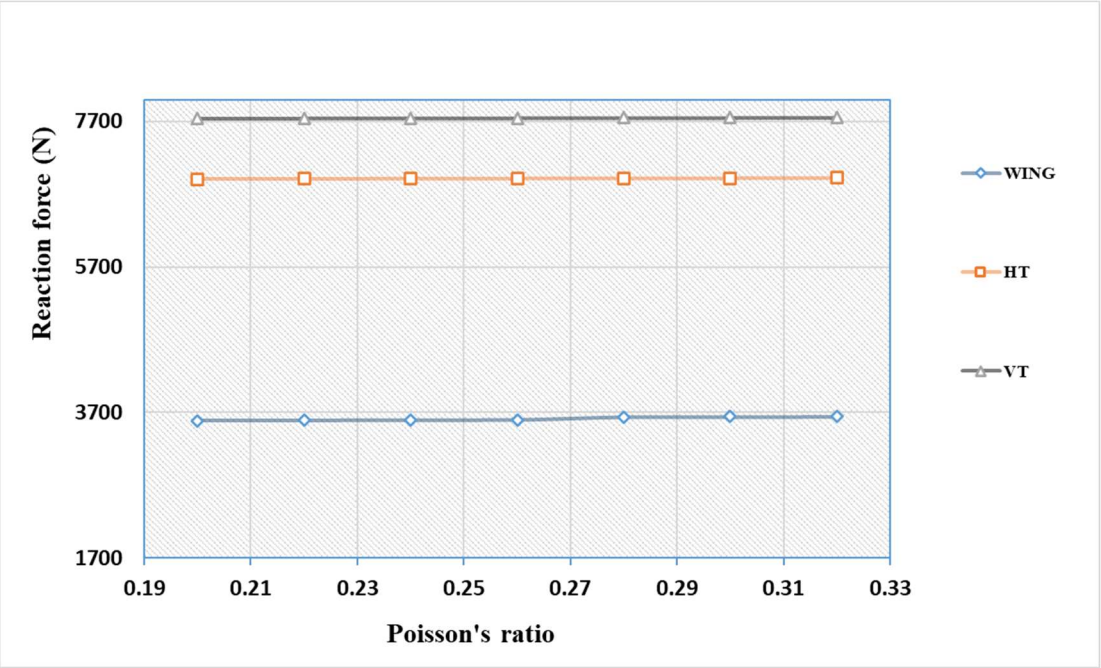

Fig 5.14 Variation of the reaction force with Poisson's ratio for different leading edge profiles and material parameters

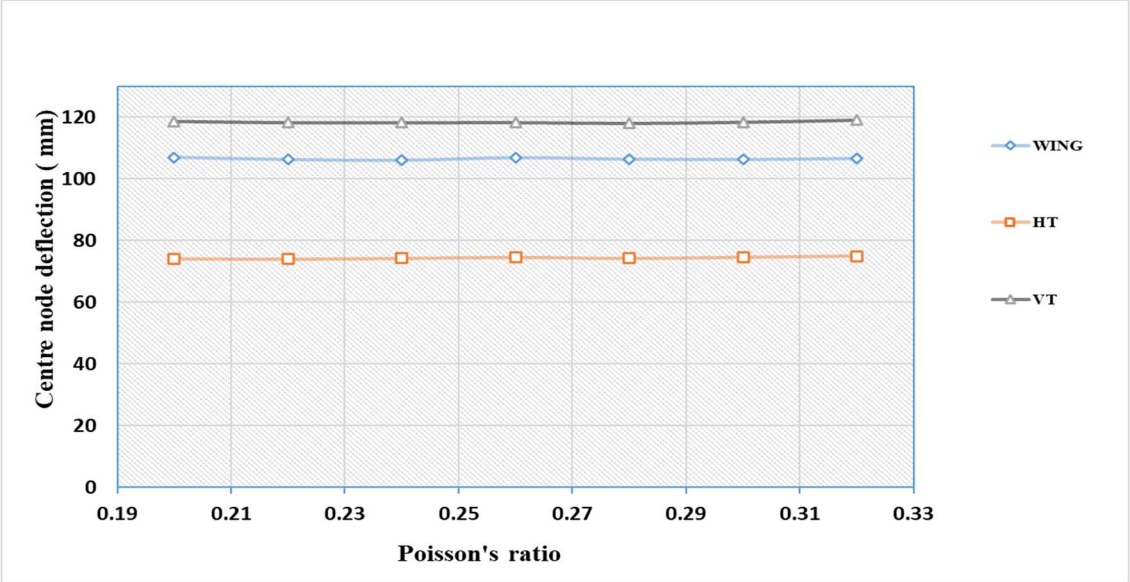

Fig 5.15 Variation of the centre deflection with Poisson's ratio for different leading edge profiles and material parameters

This chapter analysed the reaction force at support (***RF***) and centre node deflection (***U***) on the leading edges (HT, VT and wing) during soft body impact . The HT and VT profiles showed higher reaction forces than the wing leading edge profile. The highest and lowest centre displacement is reported on the VT and HT profiles, respectively. It has been found out that the elastic modulus, static yield limit, strain hardening modulus, and hardening exponent are the most influential parameters on the selected variables. The range of values for the multi-objective optimisation of the selected variables (***RF*** and ***U***) are also selcted from the parametric study results. The optimization of these material parameters for simultaneous reduction of reaction force and centre displacement are explained in the next chapter.

Chapter 6

Optimization of the material parameters of the aluminium alloy

6.1 Introduction

The parametric study done in the previous chapter helped in identifying the material parameters which influence the impact behaviour of the leading edges. Parametric analysis has been performed using different target material parameters and understanding its influence can be useful to tailor the aluminium alloy to improve its mechanical properties. From this study, it is understood that target deformation characteristics are mainly influenced by the material parameters *viz.,* elastic modulus, static yield limit, strain hardening modulus, and hardening exponent. In leading edges, careful design is vital that minimize centre displacement and maximize the energy absorption that must ensure the protection of internal sensitive components during an impact. Consequently, besides to the aerodynamic functions, a leading edge should safeguard the supporting spars and control surfaces from such impact damages. Therefore, a simultaneous reduction of reaction force and centre displacement is required to improve the energy absorbing characteristics of the material against soft body impact. Taguchi's design of experiments (DoE) with grey relational analysis is considered as an effective tool to do a multi objective optimisation. The statistical software Minitab® is used for this analysis

6.2 Optimization procedure

From the parametric study, it is understood that target deformation characteristics are primarily controlled by the parameters such as elastic modulus, static yield limit, strain hardening modulus, and hardening exponent. A series of tests is designed as per Taguchi's Design of Experiments (DoE) to optimize the above selected control parameters against

bird impact. The parameters studied are analysed for reaction force and the centre node deflection observed after complete impact. The contour plots of reaction force and displacement are shown in **Fig 6.1** and **Fig 6.2**. From the contour plots, it is clear that the reaction force varies with time of impact. When impact starts the maximum reaction force concentrates at the centre of the leading edge and with an increase in the time it starts to propagate from the centre to the edges and finally it will concentrate on the end nodes. Therefore, it is understood that after complete impact maximum reaction force observed at the end nodes. Here the soft body is impacting at the centre of the target and the maximum displacement occurs at the wing centre.

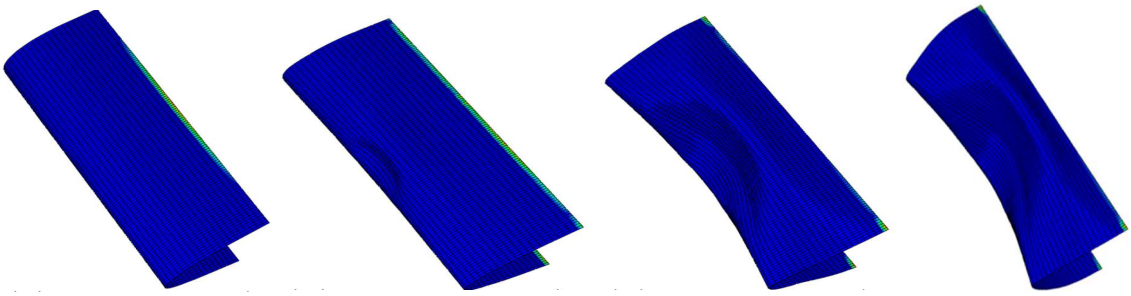

(a) t=0.0983 ms **(b) t=0.491 ms** **(c) t=1.47 ms** **(d) t=1.96 ms**

Fig 6.1 Reaction force contour plot of wing leading edge at different times

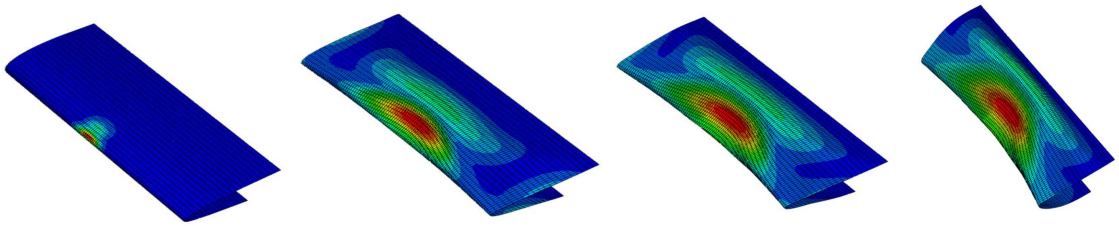

(a) t=0.0983 ms **(b) t=0.491 ms** **(c) t=1.47 ms** **(d) t=1.96 ms**

Fig 6.2 Centre displacement contour plot of wing leading edge at different times

Optimization of selected significant material parameters is done with simultaneous reduction of reaction force and centre displacement against bird impact. Taguchi's Design of Experiments (DoE) combined with grey relational analysis is a strong tool for multi-objective optimization and its procedure is explained below.

6.2.1 Design of Experiments

Taguchi's Design of Experiments (DoE) is used for the simultaneous study of several variables with a minimal number of experiments. The present study has three control parameters *viz.* elastic modulus, static yield limit, and strain hardening modulus that vary in four levels, and one parameter, the hardening exponent, varies in two levels as shown in **Table 6.1.** While considering the control parameters and their levels, the number of analyses required for the optimization study is very high. It is highly complicated and time consuming. Therefore, analysis is planned as per Taguchi L16 orthogonal array design as shown in **Table 6.2**. The results of each analysis, reaction force (***RF***) and centre displacement (***U***) occurred in the wing leading edge after complete impact is detailed in **Table 6.2**.

Table 6.1 Control parameters and their levels

Control parameters		Level 1	Level 2	Level 3	Level 4
Elastic modulus (GPa)	***E***	71	72	73	74
Static yield limit (MPa)	***A***	265	313	338	359
Strain hardening modulus (MPa)	***B***	426	457	460	480
Hardening exponent	***n***	0.34	0.45		

Table 6.2 Results for the reaction force and centre displacement of sixteen different soft body impact experiments.

	Material parameters				Results	
Exp. No.	Elastic modulus (GPa)	Static yield limit (MPa)	Strain hardening modulus (MPa)	Hardening exponent	Reaction force (N)	Centre displacement (mm)
1	71	265	426	0.34	3110	109.031
2	71	313	457	0.34	3502	105.788
3	71	338	460	0.45	3477	106.36
4	71	359	480	0.45	3532	105.008
5	72	265	457	0.45	2819	110.825
6	72	313	426	0.45	3241	107.935
7	72	338	480	0.34	3602	104.027
8	72	359	460	0.34	3662	103.115
9	73	265	460	0.34	3255	108.315
10	73	313	480	0.34	3615	105.136
11	73	338	426	0.45	3494	106.23
12	73	359	457	0.45	3592	104.794
13	74	265	480	0.45	2922	110.379
14	74	313	460	0.45	3346	107.38
15	74	338	457	0.34	3656	103.89
16	74	359	426	0.34	3706	103.073

6.2.2 Grey relational analysis

As the Taguchi method cannot use for multi-objective optimization, grey relational analysis is used to reduce multi-responses into a single response called single relational grade. The procedure is as follows:

1. The data first be normalized which is derived from the original value to make an array in the range between zero and one (Haq *et al.* 2007). It is desirable to minimize the responses, *viz.* the reaction force and displacement, then smaller the better characteristics are used for normalization by the following **equation (6.1)**

$$x_i^*(k) = \frac{max\, x_i(k) - x_i(k)}{max\, x_i(k) - min x_i(k)} \quad \textbf{(6.1)}$$

Where $x_i^*(k)$ are the normalised data, $x_i(k)$ are the result values, max $x_i(k)$ and min $x_i(k)$ are the highest and lowest values of $x_i(k)$ for the k^{th} response, i= 1–16 is the number of simulation experiments, and k = 1, 2 is the number of results or responses. The normalized data of reaction force and displacement are shown in **Table 6.3**.

2. Calculate Grey relational coefficient using the **equation (6.2)** (Haq *et al.* 2007).

$$\xi_i(k) = \frac{\Delta_{min} + \xi \Delta_{max}}{\Delta_{oi}(k) + \xi \Delta_{max}} \quad \textbf{(6.2)}$$

Where, Δ_{oi} is the deviation sequence of the reference sequence $x_o(k)$ and the comparability sequence $x_i(k)$,

$$\Delta_{oi} = \|x_o(k) - x_i(k)\| \quad \textbf{(6.3)}$$

Δ_{min} and Δ_{max} are the smallest and largest values of the absolute differences Δ_{oi} of all comparing sequences. ξ is the distinguishing coefficient and in the range between zero and one. The value of ξ is chosen as 0.5.

3. Grey relational grade (GRG) stands for the mean of grey relational coefficients corresponding to each result and is the overall representative of all the quality characteristics and is calculated by **equation (6.4)** (Haq *et al.* 2007).

$$\gamma_i = \frac{1}{m_t} \sum_{k=1}^{m} \xi_i(k) \quad \textbf{(6.4)}$$

Where, γ_i is the GRG for the i^{th} simulation experiment and m_t is the total number of response characteristics. The normalized values of reaction force and displacement, its grey relational coefficients, grey relational grade are calculated, which is presented in **Table 6.3**

Table 6.3 Grey relational grade table

Ex. No.	Normalized values		Grey relational coefficients		Grade
	RF	***U***	***RF***	***U***	
1	0.328	0.769	0.6038	0.3941	0.4990
2	0.770	0.350	0.3937	0.5881	0.4909
3	0.742	0.424	0.4026	0.5411	0.4719
4	0.804	0.250	0.3835	0.6670	0.5252
5	0.000	1.000	1.0000	0.3333	0.6667
6	0.476	0.627	0.5124	0.4436	0.4780
7	0.883	0.123	0.3616	0.8025	0.5820
8	0.950	0.005	0.3447	0.9893	0.6670
9	0.492	0.676	0.5043	0.4251	0.4647
10	0.897	0.266	0.3578	0.6526	0.5052
11	0.761	0.407	0.3965	0.5511	0.4738
12	0.871	0.222	0.3646	0.6925	0.5285
13	0.116	0.942	0.8115	0.3466	0.5791
14	0.594	0.556	0.4570	0.4737	0.4653
15	0.944	0.105	0.3463	0.8259	0.5861
16	1.000	0.000	0.3333	1.0000	0.6667

The effects of each material parameters at different levels are represented graphically as shown in **Fig 6.3** and mean grey relational grade shown in **Table 6.4**. The best material parametric combination is selected as higher the mean relational grade is the better from the **Table 6.4**.

Table 6.4 Main effects on mean grey relational grade

Parameter	Grey relational grade				Max-min
	Level 1	Level 2	Level 3	Level 4	
Elastic modulus	0.4967	0.5984	0.4931	0.5743	0.1054
Static yield limit	0.5524	0.4849	0.5285	0.5969	0.1120
Strain hardening modulus	0.5294	0.5681	0.5172	0.5479	0.0508
Hardening exponent	0.5577	0.5236	-	-	0.0341

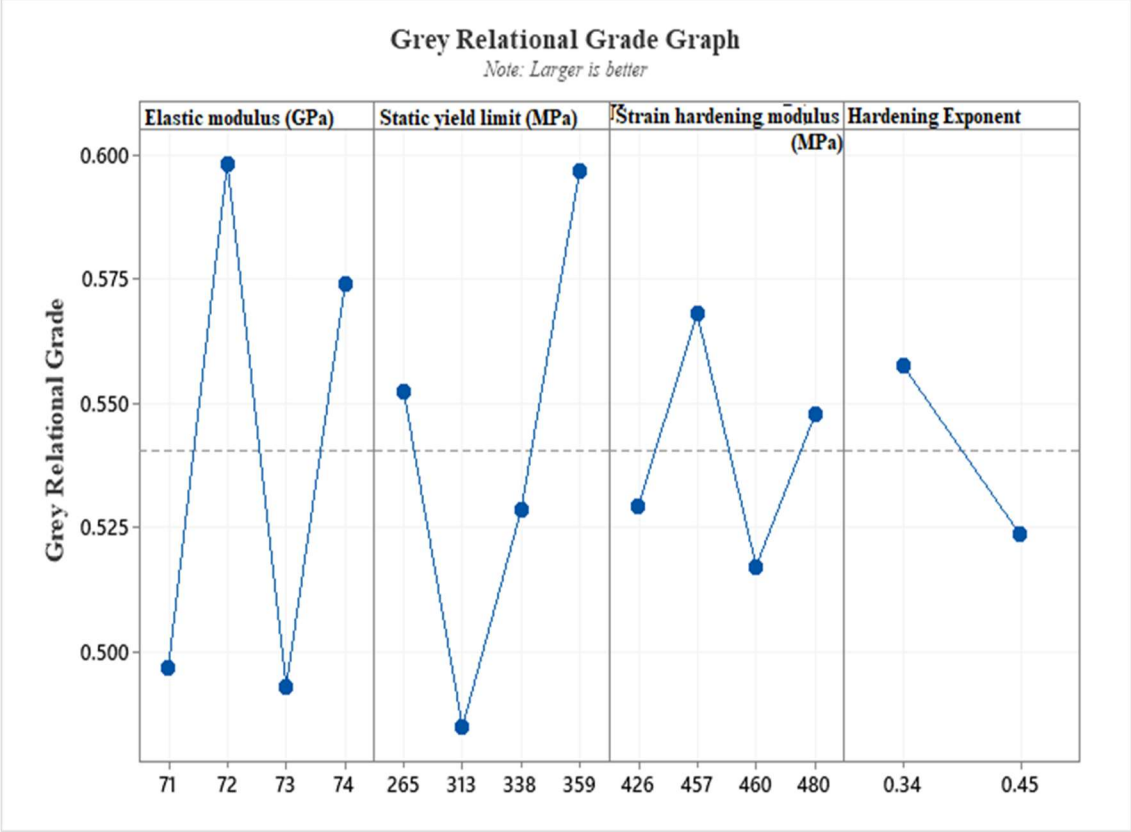

Fig 6.3 Grey relational grade graph

Thus, the optimal combination of material parameters for minimising the reaction force and maximum displacement simultaneously is ***E2A4B2n1***, *i.e.,* elastic modulus is 72 GPa, static yield limit is 359 MPa, strain hardening modulus is 457 MPa and hardening exponent is 0.34. The difference of maximum and minimum values of mean grey relational grade are 0.1054 for elastic modulus, 0.1120 for static yield limit,0.0508 for strain hardening modulus and 0.0341 for hardening exponent (**Table 6.4**). This result showed that the yield stress and elastic modulus are the most influencing parameters on results (***RF*** and ***U***) compared to other parameters. The sequence of importance of material parameters on multi-responses are static yield limit >elastic modulus > strain hardening modulus > hardening exponent.

6.2.3 Analysis of variance

When the optimum combination of parameters is selected, next is to carry out analysis of variance (ANOVA). It is a statistical technique for predicting the significant parameters that affects the multi-responses at 95% confidence level (Datta and Pal 2007). From ANOVA, it is understood that elastic modulus and static yield limit are the significant material parameters affecting multi responses because its p-values are 0.039 and 0.037, respectively which is less than 0.05 at 95% confidence level. But the parameters strain hardening modulus and hardening exponent do not show much significance on responses.

6.2.4 Confirmation test

Once the optimum combination of parameters was selected, a confirmation test is carried out to validate the improvement of grey relational grade (GRG). The predicted GRG at the optimal level ($\boldsymbol{\gamma_e}$) of the selected parameters can be calculated using the following equation (Kumar and Sahoo 2013).

$$\boldsymbol{\gamma_e = \gamma_m + \sum_{i=1}^{q}(\gamma_i - \gamma_m)} \qquad \textbf{(6.5)}$$

Where $\boldsymbol{\gamma_m}$ is the total mean grey relational grade, $\boldsymbol{q}$ is the number of parameters and $\boldsymbol{\gamma_i}$ is the mean grey relational grade at the optimal level of each parameter.

Table 6.5. Confirmation experiment

	Optimum factors	
	Prediction	Experiment
Level	E2A4B2n1	E2A4B2n1
Reaction force		3664
centre displacement		103.101
Grey relational grade	0.699	0.669

The predicted grey relational grade is calculated using **equation (6.5)** is 0.669. The grey relational grade obtained from the simulation done by optimum combination of parameters ***E2A4B2n1*** is also 0.669 is shown in **Table 6.5**.

6.3 Analysis of performance improvement for the optimized aluminium alloy

The mechanical property improvement of the optimized aluminium alloy is validated by a sequence of quasi-static tension test simulations carried out on specimens of optimized AA and AA 2024-T3. A fracture analysis is conducted to find the damage initiation and evolution parameters of the optimized aluminium alloy.

6.3.1 Quasi-static tension test

The mechanical property improvement of the optimized aluminium alloy is validated by a sequence of quasi-static tension tests have carried out on specimens of optimized aluminium alloy and AA 2024-T3. The material behaviour of the aluminum layer is incorporated through the Johnson-Cook material model (Johnson and Cook 1983). Johnson-Cook constitutive model combines strain hardening, temperature effects, and strain rate. The elastic stress is described with the parameters modulus of elasticity **(*E*)** and Poisson's ratio **(*ν*)** and flow stress was defined by the parameters shown in **equation (6.6)** (Johnson and Cook 1983).

In Johnson-Cook model equivalent the von Mises or flow stress $\bar{\sigma}$ is defined in the form.

$$\bar{\sigma} = \left(A + B\varepsilon_p^n\right)\left(1 + C ln\left(\frac{\dot{\varepsilon}_e}{\dot{\varepsilon}_0}\right)\right)\left(1 - \left(\overset{*}{T}\right)^m\right) \quad (6.6)$$

Where A is the static yield limit at the reference temperature, B is the strain hardening modulus, n is the strain hardening exponent, C is the dimensionless strain rate hardening coefficient, and m is the coefficient of temperature softening of the material can be attained from different tensile tests. ε_p is the effective plastic strain, $\dot{\varepsilon}_e$ is the effective plastic strain rate, $\dot{\varepsilon}_0$ is the reference plastic strain rate, and $\overset{*}{T}$ is the homologos temperature. The parameter values of elastic modulus, static yield limit, strain hardening modulus and strain hardening exponent are selected from the optimization study and given in **Table 6.7.** The material parameters of AA 2024-T3 are selected from the literature (Johnson and Cook 1983) as mentioned in **Table 4.1**.

Table 6.7. The material parameters of optimized aluminium alloy

ρ (Kg/m^3)	E (GPa)	v	A (MPa)	B (MPa)	n	m	C	T_r (K)	T_m (K)
2770	72	0.33	359	457	0.34	1	0.018	293	775

The tension test specimens are modelled according to E8/E8M-11 standards (**Fig 6.4**) and varying thicknesses from 0.2 mm to 0.6 mm. The test specimens are meshed with 8 node brick elements (C3D8R) with reduced integration and enhanced hourglass control. A mesh sensitivity analysis is conducted to validate the reliability of the results. The numerical convergence test is carried out to verify the accuracy of the elements in this specific case where the tension test specimen loaded quasi-statically with a controlled displacement rate of 1 mm/min. The tension test simulation model is discretized with C3D8R solid elements of different dimensions. These models are numerically analysed to verify the accuracy of the models with the experiment test. It is observed that the stress-strain curve came close to a particular value reported in the experiment test (Sharma *et al.* 2017) when total number of elements are selected to be 6174. The size of the elements of the test specimen in the gauge area and the excess area was 0.2×0.2×0.2 mm^3 and 0.4×0.4×0.4 mm^3, respectively, as shown in **Fig 6.5**. One end of the specimen is pinned with symmetric boundary conditions, and another end is provided with a controlled displacement rate of 1 mm/min, as shown in **Fig 6.5**. A time function with time step 0.01s is defined for the displacement (δ) to attain the stress-strain response. The finite element

model of the tension test simulation is validated by comparing the stress-strain curve obtained in the simulation and experiment test, as shown in **Fig 6.6** and **Fig 6.7**, respectively.

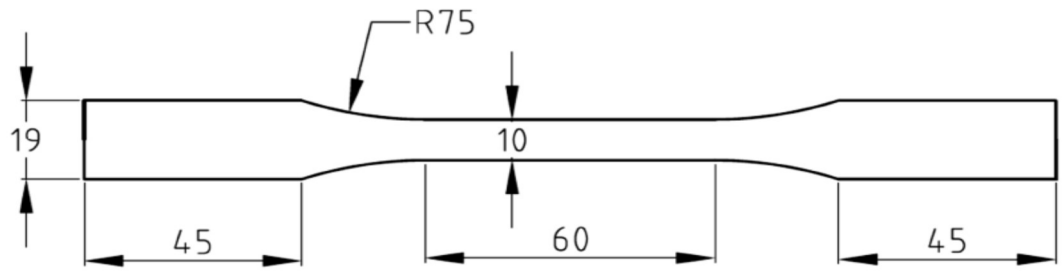

Fig 6.4 The geometry of tension test specimen as per E8/E8M-11 standards

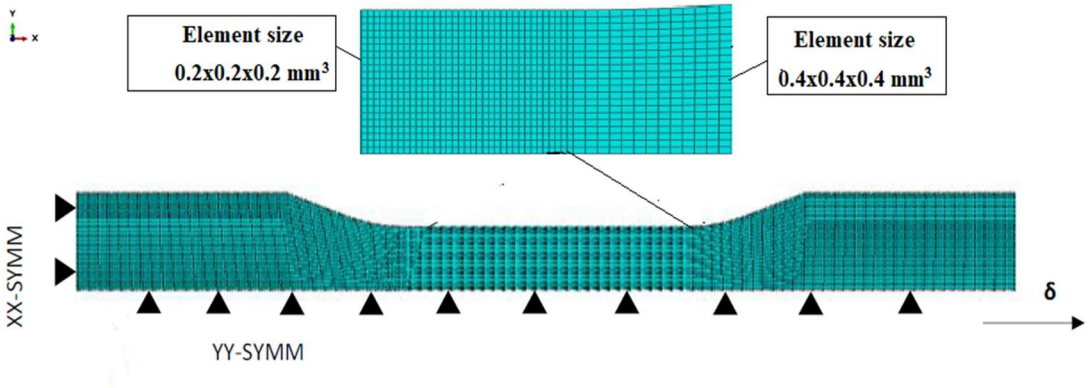

Fig 6.5 The tension test simulation model with mesh pattern, boundary and loading conditions

The stress-strain response of the optimized aluminium alloy and AA 2024-T3 obtained from the simulation test is shown in **Fig 6.6.** The mechanical properties calculated from stress-strain curves are detailed in **Table 6.8.** The stress-strain response of the improved aluminium alloy is compared with a simulation test on AA 2024-T3 and an experiment test conducted by Sharma *et al.* (2017) with the same geometry and testing conditions. The experiment test had done on a computer-controlled universal testing machine with a 25 kN load cell and deformation rate 1 mm /min. with the quasi-static loading condition**.** As shown in **Table 6.8** and **Fig 6.6**, compared with the AA 2024-T3 specimens, the ultimate strength, yield strength, and deformation energy of the optimized aluminium alloy specimen have improved simultaneously. The mechanical properties of

the test specimens with different thicknesses are analysed. It is observed that the geometry of the specimen depends on these property variations. When the thickness increased, the properties, *i.e.,* yield strength, tensile strength, and deformation energy got decreased. From this study, it could reasonably infer that the mechanical properties are inter-related to the material parameters and geometry of the specimen. From the stress-strain curve, it is clear that the strength of the optimized aluminium alloy has increased without sacrificing ductility. The optimized AA exhibited mechanical property improvement up to an average of 20.84% yield strength, 20% tensile strength, and 25% deformation energy compared to AA 2024-T3. The results showed that the optimized aluminium alloy exhibits high yield strength, ultimate tensile strength and tensile toughness compared to AA 2024-T3. This will helps improve the damage tolerance and strength to weight ratio of the structures. This enhancement in material properties ultimately helps to protect support structures and internal wing components.

Table 6.8 Mechanical properties comparison of optimized AA and AA 2024-T3

	Optimized aluminium alloy					Standard AA 2024-T3				
	0.2 mm	0.3 mm	0.4 mm	0.5 mm	0.6 mm	0.2 mm	0.3 mm	0.4 mm	0.5 mm	0.6 mm
Yield strength (MPa)	449.6	448.2	447.9	447.1	447.4	355.3	354.9	354.8	354.2	354.3
Tensile strength (MPa)	582.1	578	577.7	577.4	577.9	468.6	467.4	467.2	467.3	466
Deformation energy (J/mm^3)	65.76	64.99	63.6	63.31	62.13	49	48.22	47.93	47.94	46.94

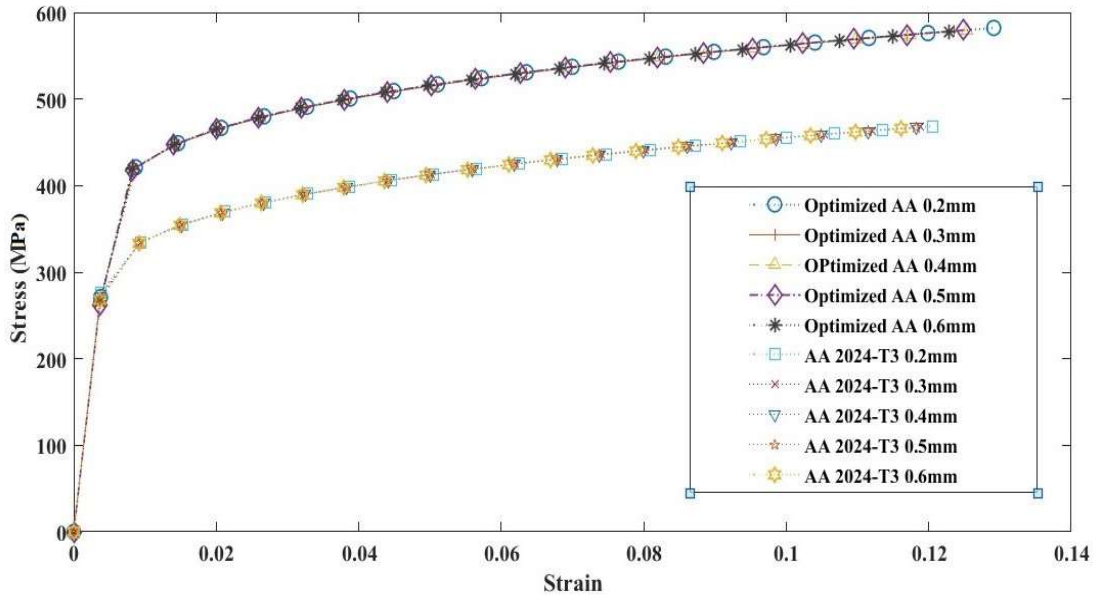

Fig 6.6 Stress-strain curve comparison of optimized AA and AA 2024-T3

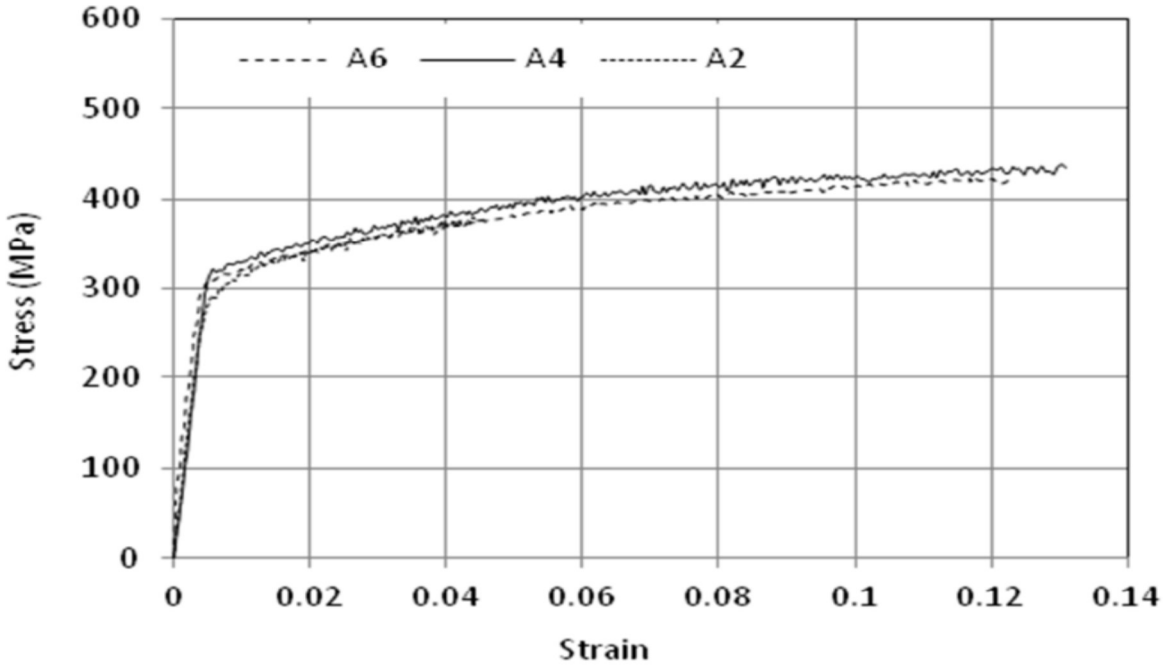

Fig 6.7 Stress-strain curve of aluminium alloy (AA 2024-T3) experiment test (A2-0.2 mm, A4- 0.4 mm, A6-0.6 mm)

[Reprinted from Composites Part B: Engineering, Vol. 125, Ankush P. Sharma, Sanan H. Khan, Venkitanarayanan Parameswaran, "Experimental and numerical investigation on the uni-axial tensile response and failure of fiber metal laminates," pp. 259-274, © 2017, with permission from Elsevier.]

Table 6.9 Isotropic hardening details of optimized aluminium alloy

Flow stress (MPa)	270	449	480	500	516	531	543	554	565	576	578
Plastic strain (%)	0	0.8	2	3.1	4.4	5.6	6.8	8.2	9.6	11.1	11.9

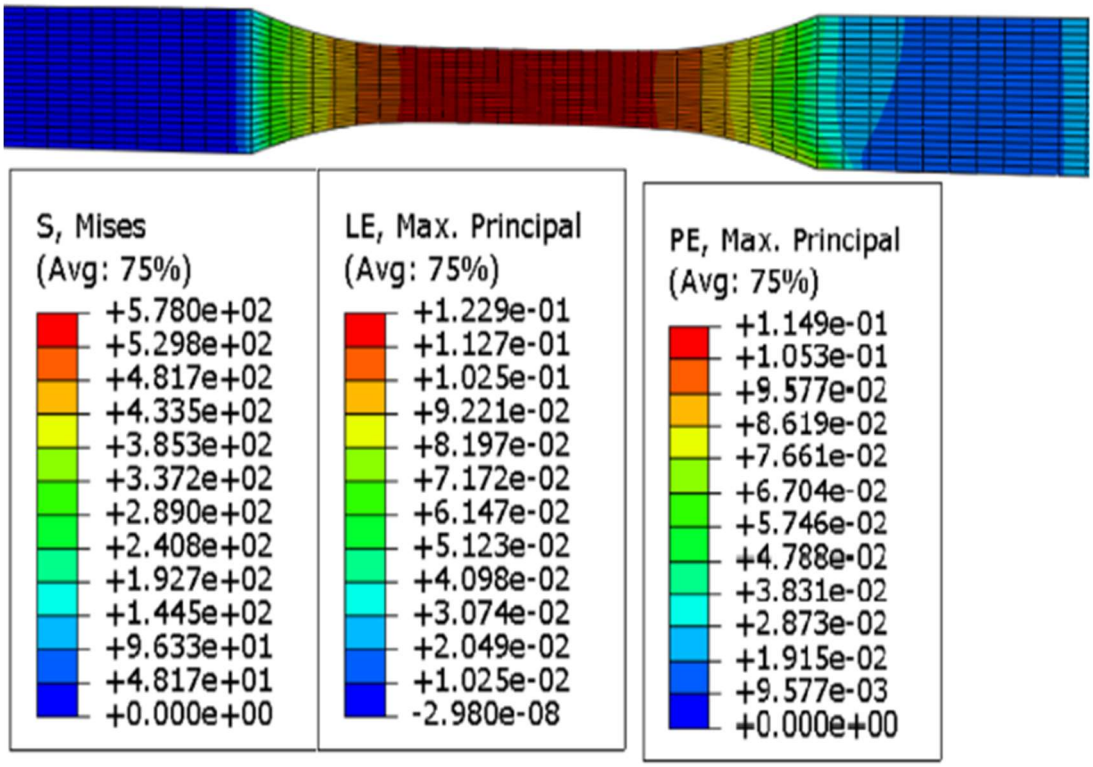

Fig 6.8 Stress-strain parameters of optimized aluminium alloy at ultimate stress point

6.3.2 Failure analysis of optimized aluminium alloy

Failure analysis is performed to find the damage initiation and evolution parameters of the optimized aluminium alloy. The isotropic hardening data for the optimized aluminium alloy and AA 2024-T3 are fetched from the tensile test results and is given in **Table 6.9**. The isotropic hardening data for AA 2024-T3 are in good agreement with experimental test results (Sharma *et al.* 2017) under the same specimen and loading conditions (**Table 6.10**). Flow stress and plastic strain define the plastic behaviour of the material. The test specimen of 2 mm thickness is loaded at a controlled displacement rate

up to the breaking point, and a sudden failure occurred after the ultimate stress point. The profile of the test specimens before and after impact is shown in **Fig 6.9**. The stress-strain curve of optimized aluminium alloy **(Fig 6.10)** showed significant improvement in energy absorption compared to AA 2024-T3. The optimized aluminium alloy and AA 2024-T3 showed ultimate stress values of 584.7 MPa and 469.4 MPa at corresponding strain values of 0.1256 and 0.1154, respectively. After failure, the stress of the optimized aluminium alloy reached 370.6 MPa, and the stress of AA 2024-T3 reached 170.8 MPa.

Table 6.10 The stress-strain data of AA 2024-T3 (experiment test and simulation), optimized aluminium alloy(simulation) (2 mm test specimen)

AA 2024-T3 (Experiment) (Sharma *et al.* 2017)		AA 2024-T3 (Simulation)		Optimized aluminium alloy	
Flow stress (MPa)	Plastic strain (%)	Flow stress (MPa)	Plastic strain (%)	Flow stress (MPa)	Plastic strain (%)
294	0	277	0	274	0
335	1.1	335	1.07	450	0.8
362	2.2	360	2.2	480	2.01
381	3.2	381	3.6	501	3.23
399	4.4	399	4.5	517	4.44
415	5.5	413	5.7	531	5.67
430	6.7	436	6.9	543	6.92
443	7.8	446	8.1	554	8.23
459	9.2	456	9.3	565	9.62
469	10.1	464	10.7	576	11.1
480	11.2	478	11.4	581	12.1

The plastic deformation failure model includes the product of failure strain, stress triaxiality, and strain rate. The damage initiation and evolution parameters of the optimized aluminium alloy are found out from the fracture analysis. Damage initiation parameters,

failure strain and stress triaxiality, are recorded directly from the ABAQUS output check card.

After damage initiation, an accurate representation of the stress-strain curve is very difficult in ductile materials. The ductile damage initiation failure model is the product of failure strain, stress triaxiality and strain rate (Seidt and Gilat 2013). The fracture energy is defined with the **equation (6.7)** suggested by Hillerborg (1985).

$$G_f = \int_0^{\bar{u}_f} \sigma_f d\bar{u} \qquad (6.7)$$

Where, σ_f is the ultimate stress and $\bar{u}_f$ is the plastic displacement at failure. The fracture energy of the optimized aluminum alloy is found out as 49.26 KJ/m^2. **Fig 6.7** shows the specimen at ultimate stress condition and at the breaking stress condition. The damage variables of the optimized aluminium alloy are shown in **Table 6.11.**

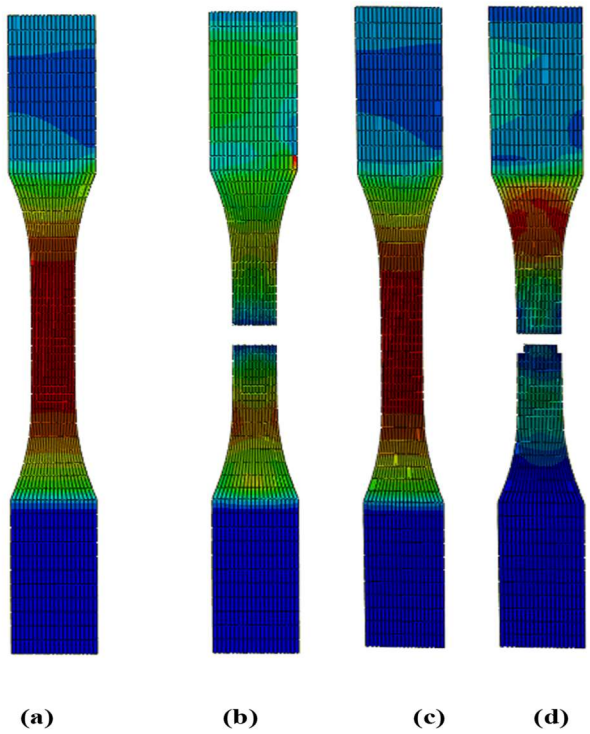

Fig 6.9. Test specimen models of 2mm thickness (a) AA 2024-T3 at ultimate stress point (b) AA 2024-T3 at breaking stress point (c) optimized aluminium alloy at ultimate stress point (d) optimized aluminium at breaking stress point

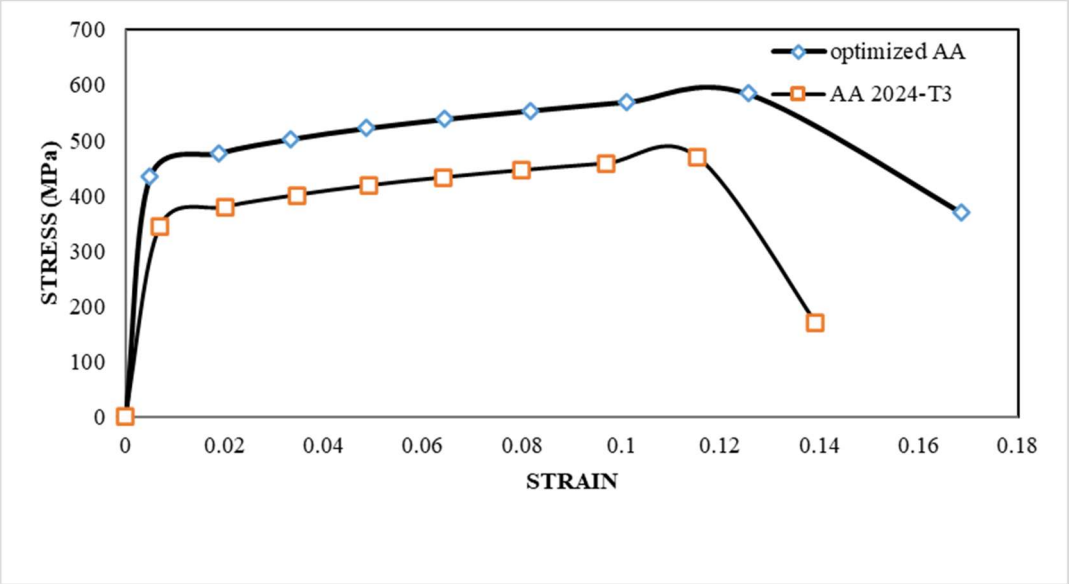

Fig 6.10 Stress-strain curve comparison of optimized AA and AA 2024-T3 (2 mm thickness specimen) till failure

Table 6.11 Damage parameters of the optimized aluminium alloy

Damage initiation			Damage evolution
Fracture strain	Stress triaxiality	Strain rate (/s)	Fracture energy (kJ/m^2)
0.1685	-1.307	0.0012	49.26

6.3.3 Impact analysis on optimized aluminium alloy

The response of the optimized aluminium alloy plate against soft body impact is investigated using the finite element software ABAQUS/Explicit. The geometric model of the soft body is modelled, as shown in **Fig 6.11**. The previously validated soft body model is used as the projectile. The aluminium alloy square plate of 200 mm is created in the ABAQUS part module. This model is meshed with C3D8R solid continuum elements, as shown in **Fig 6.11**. The impact velocity of 117 m/s is selected as per the certification requirements. The interaction between the soft body and the aluminium alloy plate is established as a general contact in a pure master-slave approach. This response helps to read the accurate results as the behaviour of the soft body is highly nonlinear. The edges of the aluminium plate are constrained with all degrees of freedom, as shown in **Fig 6.12**. The soft body is imparted on the 200 mm aluminium plate with an impact velocity of 117 m/s.

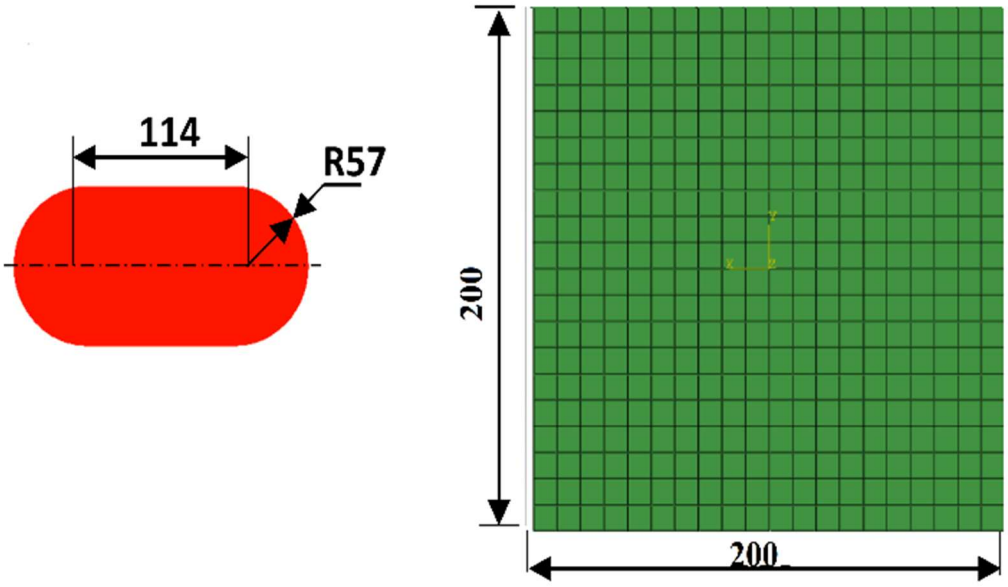

Fig 6.11 Model of soft body projectile and aluminium plate (All dimensions in mm)

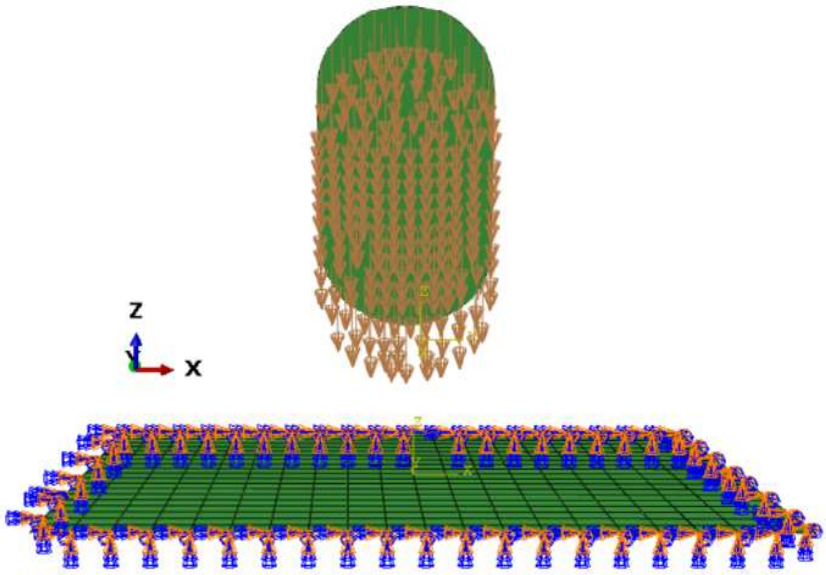

Fig 6.12 Loading and boundary conditions of soft body and aluminium plate

The trajectory of the reaction force versus displacement can be divided into three parts. At first, during impact with a velocity of 117 m/s, the front face of the soft body projectile is immediately brought to rest. As a result, a shock wave (called Hugoniot shock) is formed after the body strikes the target (**Fig 6.13**). There is a minor change in the reaction force values with displacement. At this point, the relationship between reaction force and displacement is linear. This response can be ascribed due to the prime contact between the

soft body and the plate. The particles at the end of the soft body meet with a high-pressure gradient because of the initial shock pressure.

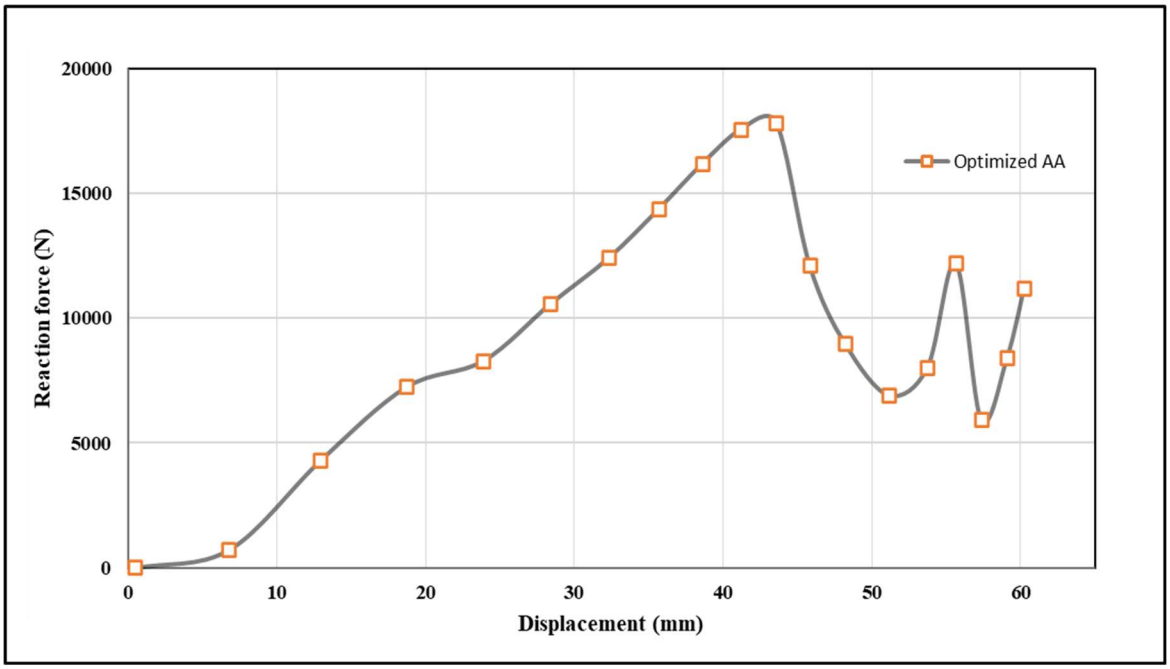

Fig 6.13 Reaction force versus displacement curve of optimized aluminium alloy

Owing to this high-pressure gradient soft body flows over the plate, and particles accelerate outwards to form a release wave. The release wave propagates towards the impact centre, which interacts with the shock wave. Then the reaction force value gradually increases with the displacement due to the film reaction of the aluminium alloy plate. At the shock decay stage, pressure decreases at the impact point due to the interaction between the shock wave and release wave. In the steady flow stage, the soft body starts to flow steadily after multiple interactions between the shock and release waves. The latter phase of impact is characterized by the decay of the impact forces and pressure exerted on the target. Pressure gradually decreases as the release waves interact with shock waves. The soft body flows completely radially at the point where steady flow is obtained, reaching a steady stagnation point. Once the reaction force value reaches a peak value, it gradually reduces as the projectile propagates through the area. **Fig 6.14** and **Fig 6.15** show the deformation pattern of the soft body and aluminium plate at different times.

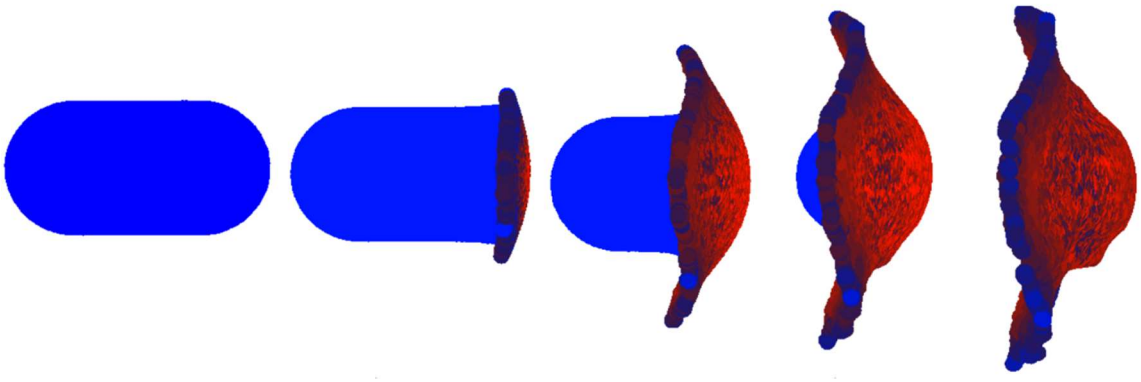

(a) t=0 ms (b) t=0.5ms (c) t=1 ms (d) t=1.5 ms (e) t=1.94ms.

Fig 6.14 Deformation pattern of the SPH soft body at different times when impacting on aluminium plate

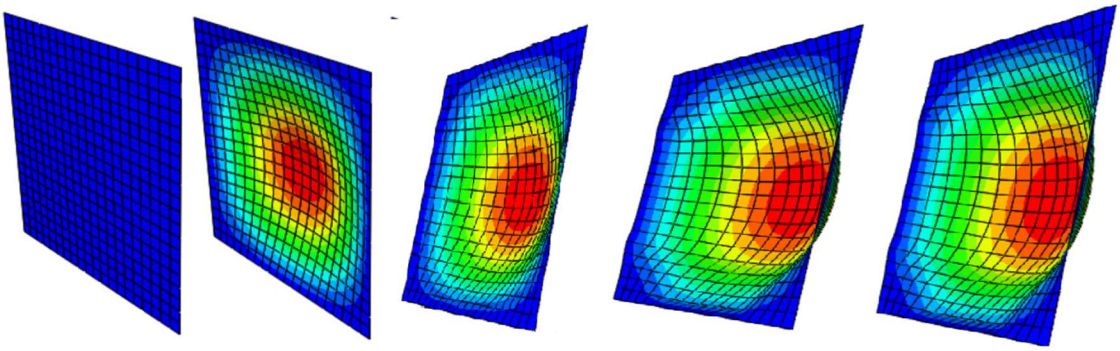

(a) t=0 ms (b) t=0.5 ms (c) t=1 ms (d) t=1.5 ms (e) t=1.94ms.

Fig 6.15 Deformation pattern of the aluminium plate at different times when impacted with a SPH soft body

This chapter concluded that the performance improvement of the optimized aluminium alloy helps protect the support structure and wing components. The optimized aluminium alloy showed higher energy absorption capacity and better resistance to a bird strike. The aluminium alloy skin must absorb most of the impact energy and transmit less load to the support components while reducing wing centre displacement to protect the inner wing components. Therefore, this optimized aluminium alloy can be used as an alternative material to fabricate the GLARE laminates for wing leading edges instead of AA 2024-T3 in conventional GLARE laminates.

Chapter 7

Analysis of performance improvement for fibre metal laminates

7.1 Introduction

Wing leading edges are fabricated using Glass Aluminium Reinforced Epoxy (GLARE) laminate which includes alternatively arranged aluminium alloy and glass fibre epoxy layers. These laminates exhibit excellent fatigue and impact resistance. The GLARE laminates also express strain rate dependency, and this property allows high energy absorption when experiencing a high-velocity impact (Volt 1996). The properties of different GLARE laminates are explained in the literature (Sinmazcelik *et al.* 2011; Sadighi *et al.* 2012; Botelho *et al.* 2006; Gunnink *et al.* 2002; Alderliesten *et al.* 2003). Of the available GLARE grades, GLARE 3 and GLARE 5 are specifically manufactured for impact resistance. In a coding system, a GLARE laminate is defined as GLARE 5-2/1-0.2 means that: GLARE 5- a glass-based laminate with [0/90/90/0] orientation of glass fibres, 2/1- one glass/ epoxy layer is bonded between two number of aluminium layers and 0.2- thickness of the aluminium alloy sheets. The studies to improve the properties of GLARE have been broadened due to its enriched impact and fatigue properties compared to other substitutes of equal areal density (Fatt *et al.* 2003).

The performance improvement of the fibre metal laminates tailored with optimized aluminium alloy is validated with the comparison of conventional GLARE laminates. Three GLARE laminates are tailored with glass fibre epoxy layers and optimized aluminium alloy layers. The improvement in mechanical properties of the GLARE laminates tailored with optimized aluminium alloy is verified by comparing their performance with GLARE laminates tailored with AA 2024-T3.

7.2 Fibre metal laminate modelling

The finite element software ABAQUS is used to generate numerical simulations to discover the nonlinear tensile response behaviour of GLARE laminates. The GLARE laminates are tailored with aluminium alloy layers and glass/epoxy prepreg layers. Glass/epoxy exhibits limited ductility before fracture, but the average strain to failure of the aluminium alloy is 13%. Owing to these different material properties, different material models are essential to represent their respective behaviour.

7.2.1 Composite material layer modelling

Intra laminar failure model

Hashin proposed (Hashin and Rotem 1973) and later modified (Hashin 1980) a failure criterion which is available in ABAQUS is used to predict the damage modes in the composite part of the tension test specimen. The four failure modes are given in **equations (7.1)** to **(7.4)**

Fibre tension ($\hat{\boldsymbol{\sigma}}_{\mathbf{11}} \geq \mathbf{0}$)

$$\boldsymbol{F_f^t} = \left(\frac{\hat{\sigma}_{11}}{X^t}\right)^2 + \boldsymbol{\alpha}\left(\frac{\hat{\sigma}_{12}}{S^L}\right)^2 \qquad \textbf{(7.1)}$$

Fibre compression($\hat{\boldsymbol{\sigma}}_{\mathbf{11}} \leq \mathbf{0}$)

$$\boldsymbol{F_f^c} = \left(\frac{\hat{\sigma}_{11}}{X^c}\right)^2 \qquad \textbf{(7.2)}$$

matrix tension ($\hat{\boldsymbol{\sigma}}_{\mathbf{22}} \geq \mathbf{0}$)

$$\boldsymbol{F_m^t} = \left(\frac{\hat{\sigma}_{22}}{Y^t}\right)^2 + \left(\frac{\hat{\sigma}_{12}}{S^L}\right)^2 \qquad \textbf{(7.3)}$$

Matrix compression ($\hat{\boldsymbol{\sigma}}_{\mathbf{22}} \leq \mathbf{0}$)

$$\boldsymbol{F_m^c} = \left(\frac{\hat{\sigma}_{22}}{2S^T}\right)^2 + \left[\left(\frac{Y^c}{2S^T}\right)^2 - \mathbf{1}\right]\left(\frac{\hat{\sigma}_{22}}{Y^c}\right) + \left(\frac{\hat{\sigma}_{12}}{S^L}\right)^2 \qquad \textbf{(7.4)}$$

Effective stress tensor components are $\hat{\sigma}_{ij}$ **(*i,j* = 1,2),** the tensile or compressive strength of fibre metal laminates in longitudinal and transverse directions denoted by $X^t(X^c)$ and $Y^t(Y^c)$ respectively. S^j **(*j* = *L*)** indicates in-plane shear strength and S^j **(*j* = *T*)** indicates out-of-plane shear strength. When F_i^j **(*i=f, m* and *j=c, t*)** meets unity it represents the failure has taken place in the equivalent mode (Hashin 1980).

When the damage norms have been fulfilled, the degradation of the material is represented using damage attributes d_m, d_f and d_s which defines the present condition of matrix damage, fibre damage and shear damage respectively. These parameters constantly modify from zero (undamaged state) to one (completely degraded material). The material behaviour is linearly elastic before failure initiates. When the relation between stress and strain is ***{σ}=[C]{ε},*** in which ***[C]*** represents elasticity matrix. When failure initiated ***[C]*** replaced to damaged elasticity matrix $[C_d]$ is shown in equation **(7.5)** (Lapczyk and Hurtado 2007)

$$(C_d)=\frac{1}{D}\begin{pmatrix} (1-d_f)E_1 & (1-d_f)(1-d_m)\nu_{21}E_1 & 0 \\ (1-d_f)(1-d_m)\nu_{12}E_2 & (1-d_m)E_2 & 0 \\ 0 & 0 & (1-d_s)G_{12}D \end{pmatrix} \quad (7.5)$$

Where $D= 1-(1-d_f)(1-d_m)\nu_{12}\nu_{21}$, E_1 and E_2 are the logtitudinal and transverse modulus, ν_{12} is the Poisson's ratio and G_{12} is the modulus of rigidity.

Table 7.1 The mechanical properties of S2 glass/epoxy

(Seo *et al.* 2010; Koohbor *et al.* 2014; Scalici *et al.* 2015)

E_1	E_2	ν_{12}	G_{12}	G_{23}	X^t	X^c	Y^t
30.5 GPa	4.03 GPa	0.29	2.08 GPa	1.44 GPa	700 MPa	350 MPa	39 MPa

Y^c	G_{1t}	G_{1c}	G_{2t}	G_{2c}	S_{12}
128 MPa	92 N/mm	79 N/mm	0.22 N/mm	0.61 N/mm	50 MPa

Inter-laminar failure model

The quadric traction behaviour between the cohesive surfaces is considered to capture the delamination between the laminate plies. This approach uses classical bilinear traction separation law between the surfaces. A traction displacement correlation is applied

between the common node of the interface. when the delamination initiates, the common node distorts and fails. The traction induced between the surfaces is described with a linear relationship in **equation (7.6).**

$$\hat{t}=\begin{Bmatrix} t_n \\ t_s \\ t_t \end{Bmatrix}=\begin{bmatrix} K_{nn} & 0 & 0 \\ 0 & K_{ss} & 0 \\ 0 & 0 & K_{tt} \end{bmatrix}\begin{Bmatrix} \delta_n \\ \delta_s \\ \delta_t \end{Bmatrix} \quad (7.6)$$

Where, t_i are the traction vectors, k_{ii} are the coefficients of stiffness and δ_i are relative displacements at contact point. The damage initiation is defined with the quadric nominal stress criterion for cohesive surfaces

$$\left\{\frac{\langle t_n \rangle}{t_n^0}\right\}^2+\left\{\frac{t_s}{t_s^0}\right\}^2+\left\{\frac{t_t}{t_t^0}\right\}^2=1 \quad (7.7)$$

where t_n^0 , t_s^0, t_t^0 are the strength attributes at interface and $\langle . \rangle$ is the Macaulay bracket. Benzeggagh-Kenane criterion (Benzeggagh and Kenane 1999) is used to define linear damage evolution. The G_{Ic}, G_{IIc} and G_{IIIc} are the failure energy at different modes. Delamination modelling have been explained in literature (Davila *et al.* 2001; Campilho *et al.* 2013) detailly.

Table 7.2 Material properties of epoxy layer

(Scalici *et al.* 2015)

K	t_n^0	t_s^0	t_t^0	G_{Ic}	G_{IIc}	G_{IIIc}	β
10^6 N/mm^3	39 MPa	50 MPa	50 MPa	0.22 N/mm	0.36 N/mm	0.36 N/mm	1.42

7.2.2 Metallic layer modelling

The material behaviour of the metallic layer is defined with Johnson Cook failure model as explained in section 6.2. The damage behaviour is defined with ductile damage model. The strength parameters of the optimized aluminium alloy are given in **Table 6.7**. The damage initiation and evolution parameters had obtained from the fracture analysis carried out on optimized aluminium alloy specimen and are detailed in **Table 6.11.**

7.3 Tension test analysis on fibre metal laminates

The tension test analysis is carried out to study the performance improvement of the GLARE laminates tailored with optimized aluminium alloy than conventional GLARE laminates. The improvement of the properties is investigated by analysing on damage (aluminium yielding, matrix failure, fibre failure and delamination) and strength properties (yield strength, tensile strength and deformation energy). The GLARE 5 and GLARE 3 are the laminates considered for this study mainly designed for impact resistance. Three GLARE laminates with different configurations also analysed to study the effect of thickness, metal stacking sequences and fibre orientations.

7.3.1 Finite element modelling procedure

The finite element model of the GLARE laminate specimen is validated with an experimental test done by Vlot and Gunnink (2001). For this purpose, tension test simulation is carried out on a GLARE 5-2/1 with [0/90/90/0] fibre-oriented glass epoxy prepreg layers stacked between layers of AA 2024-T3. The GLARE laminate specimen model is built in the pre-processing module of ABAQUS/CAE according to ASTM D-3039. The straight rectangular tension test specimen of length 305 mm and a width of 25.5 mm is modelled. The dimensions, boundary conditions, and loading directions are explained in **Fig 7.1**. Each layer of the GLARE laminate specimen is modelled separately, and the appropriate local orientation is applied. These metal and composite layers are then assembled into specific configurations. The tension test models are numerically analysed to verify the accuracy of the finite element model with the experimental test. It is observed that the stress-strain curve obtained in simulation have good agreement with experiment test (Vlot and Gunnink 2001) when the size of the elements is selected to be 0.2×0.2×0.2 mm^3, as shown in **Fig 7.1**. Each composite layer has meshed with 4576 continuum shell elements (SC8R), and the aluminium layer meshed with 4576 solid brick elements (C3D8R). Stiffness and enhanced hourglass controls are applied to continuum shell elements and solid continuum elements. Two elements are placed through the thickness of each layer to make the results are mesh independent. The coefficient of friction between the metal plies and composite plies is chosen as 0.3, while among composite plies, the value of 0.5 is selected based on a previous study (Shi *et al.* 2014). One end of the specimen is

constrained with all degrees of freedom, and the other gripped end is provided with a displacement of 1 mm/min.

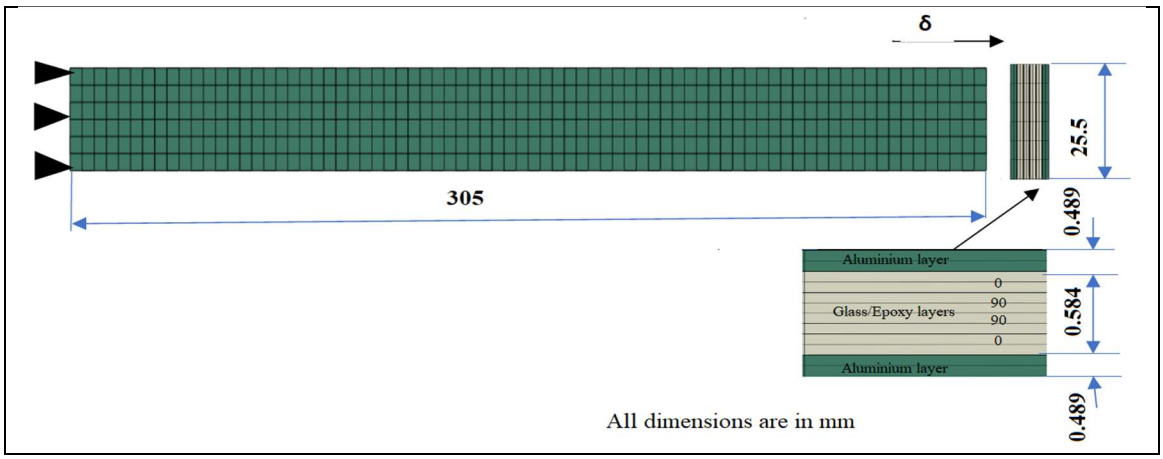

Fig 7.1 The tension test simulation model of GLARE 5-2/1 specimen with mesh pattern, boundary and loading conditions

After the validation of the GLARE laminate model, three GLARE laminates has been modelled with different stacking sequences and metal thicknesses while keeping the overall thickness the same. Then tension test simulations are carried out to compare the improvement of strength and damage properties of GLARE laminates tailored with optimized aluminium alloy compared to GLARE laminates tailored with AA 2024-T3. The details of GLARE laminates considered in this study are shown in **Table 7.3.**

Table 7.3 Details of GLARE laminates considered for tension test simulation

code	Lay-up sequence	Aluminium thickness (mm)	Total thickness (mm)
GLARE 5-2/1-0.2	A2/0/90/90/0/A2	0.2+0.2	1.7
GLARE 3-3/2-0.2	A2/0/90/A2/90/0/A2	0.2+0.2+0.2	1.7
GLARE 5-2/1-0.4	A4/0/90/90/0/A4	0.4+0.4	1.7

7.4 Results and discussion

7.4.1 Finite element model validation

To verify the finite element modelling approach used, the FE model is validated with the experimental results available in the literature (Vlot and Gunnink 2001). For validation, tension test simulations are carried out on a GLARE 5-2/1 with [0/90/90/0]

fibre-orientated glass epoxy prepreg layers stacked between layers of AA 2024-T3. The tensile specimen model was validated by comparing the stress-strain response of GLARE-5-2/1 obtained from experimental tests (Vlot and Gunnink 2001) and numerical simulations, as shown in **Fig. 7.2**. The stress-strain curve exhibited a linear behaviour up to the yield point. Until now, aluminium and composite layers are loaded by their elastic modulus. Stress-strain curves predicted from FEA are consistent with experimental tests under longitudinal tensile loading, validating the finite element modelling approach. It is seen that, in general, the model fits the experimental data fairly well, with some deviation at high stress. The ultimate strength of the GLARE laminate in finite element simulation is 719 MPa, While GLARE laminate specimens used for experimental testing were observed to be 696 MPa on average. However, in simulations and experimental tests, the failure strain of GLARE laminates is approximately 4%. This is typically the failure strain observed for the unidirectional S2 glass prepregs.

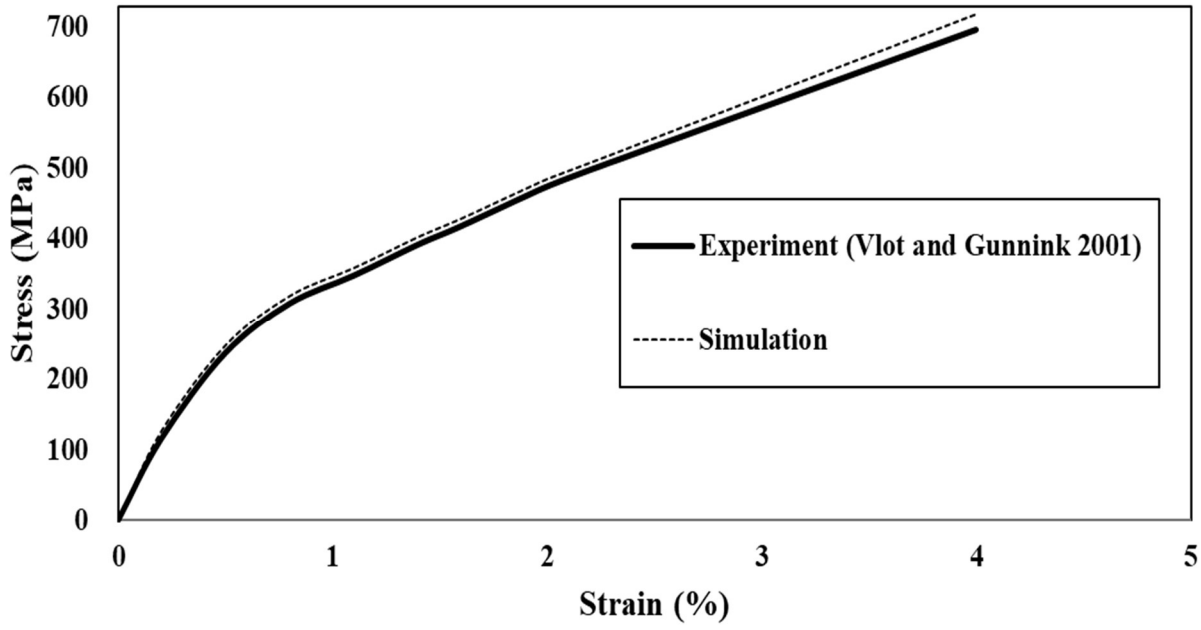

Fig. 7.2 FEM prediction of stress–strain curve for GLARE 5-2/1 compared to experimental results from Ref. (Vlot and Gunnink 2001)

While analysing the simulation results, the stress-strain curve exhibited a linear behaviour up to the yield point. Until this point, both aluminium and composite layers are loaded by their elastic modulus. When the stress reaches 296 MPa, the aluminium layer begins to yield, as shown in **Fig 7.3 (b)** and **Fig 7.3 (b1).** As a result, the load-carrying

capacity of aluminium decreased. But when the load increasing the stress increasing. This stress increase is due to the support by the composite layer to the fibre metal laminate. After yielding, the stress-strain curve exhibited nonlinear hardening behaviour until the ultimate stress is reached. As shown in **Fig 7.3 (c),** a side view of the specimen can be seen at the stress level of 339.5 MPa, where the matrix tension failure begins. The **Fig. 7.3 (d)** shows an edge view of the specimen visible at a stress level of 719 MPa, where fibre tensile failure begins, the ultimate stress level. The ultimate stress occurred at maximum in-plane strain of 4 %. After fibre failure, sudden stress drops to 700 MPa at a maximum in-plane strain of 4.5 %, as shown in **Fig 7.3 (d).**

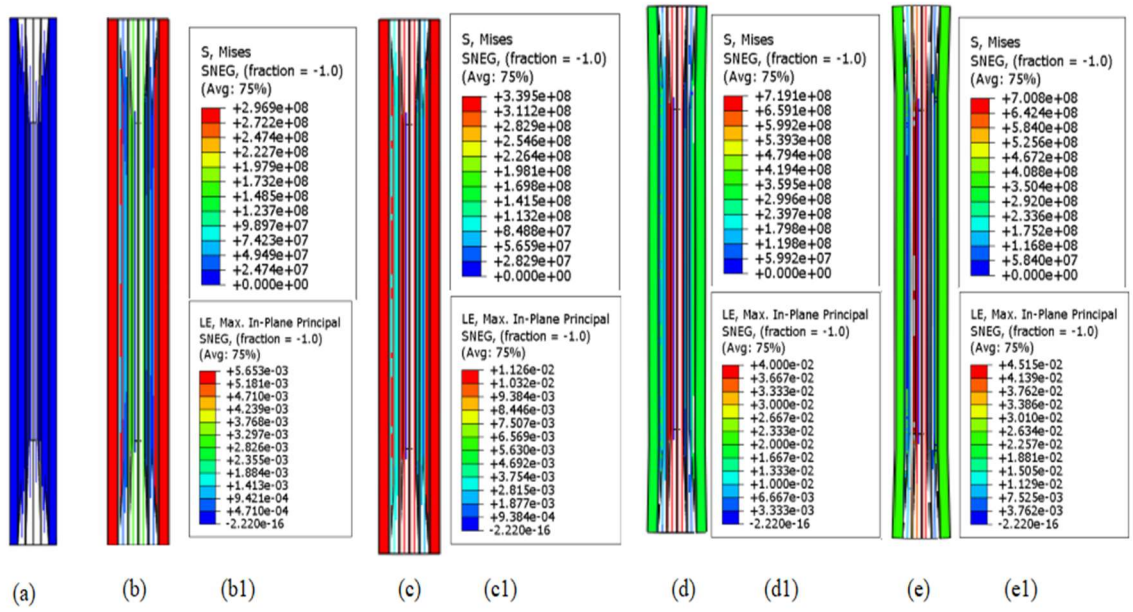

Fig 7.3 The edge view and stress-strain contours of the GLARE-5-2/1 laminate tailored with AA 2024-T3

7.4.2 Performance improvement study of the GLARE laminate with optimized aluminium alloy

A tension test simulation is carried out on the same finite element model of GLARE 5-2/1 with optimized aluminium alloy. The improvement of the mechanical properties during tension loading are analysed. The edge view and stress levels at different points are shown in **Fig 7.4**. Aluminium yields only when the stress level reached 384 MPa, as shown in **Fig 7.4 (b)** and **Fig 7.4 (b1)**. The stress point at which aluminium yields showed exhibited a significant improvement over that of the conventional GLARE laminates as in

Fig 7.3 (b) and **Fig 7.3 (b1)**. Matrix tension failure initiation is also observed in the increased stress level of 438.7 MPa, as displayed in **Fig 7.4 (c)** and **Fig 7.4 (c1).** However, fibre tension failure initiated at approximately the same stress-strain conditions in both GLARE laminates. After the matrix failure the composite layers become the main load carrying element. This is why the fibre tension failure initiated at same stress points in both GLARE laminates. Maximum in-plane strain increased slightly at ultimate stress and stress drop levels. In the side view of the test specimen displayed in **Fig 7.3 (d)** and **Fig 7.3 (e),** the aluminium layers are visible in green colour, while in **Fig 7.4 (d)** and Fig **7.4 (e),** the aluminium layers are visible in yellow colour. These stress profiles showed that the aluminium layer with optimized aluminium alloy achieves more energy absorption capacity than the AA 2024-T3 layer. Delamination is observed in all layers, but complete delamination has not occurred in both cases. The quadric traction for cohesive surfaces is more in between metallic to composite layers than composite to composite layers.

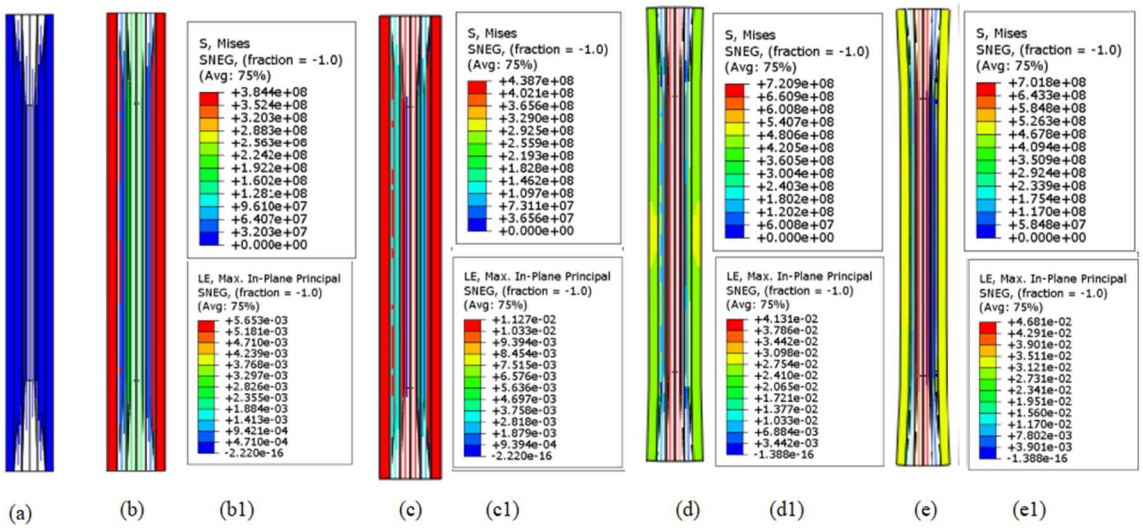

Fig 7.4 The edge view and stress-strain contours of the GLARE-5-2/1 laminate with optimized aluminium alloy

7.4.3 Comparison study of different GLARE laminates

In order to estimate the damage and strength properties of the GLARE laminates tailored with optimized aluminium alloy, three finite element models with different metal thickness and metal stacking sequences are correspondingly generated and compared with GLARE laminates tailored with AA 2024-T3. The performance of the GLARE laminates is compared based on damage variables, *i.e.,* yielding of aluminium, matrix tension failure,

fibre tension failure and delamination. The performance of the GLARE laminates also compared based strength attributes, *i.e.,* yield strength and deformation energy. The results of tension test simulations on these GLARE laminate configurations as mentioned in **Table 7.3** is described below

Response of GLARE 5-2/1-0.2 laminate

The stress-strain response of the 5-2/1-0.2 laminate is shown in **Fig 7.5**. When the tension loading increased in the first stage, a more or less similar slope is noticed in both GLARE laminates. After this, a change in slope is observed at 397 MPa and 316 MPa for GLARE laminate with optimized AA and AA 2024-T3, respectively. This change is accepted to be due to the yielding of aluminium alloy. A significant increase in the yield strength can be observed in the GLARE laminate tailored with optimized aluminium alloy. As the loading increased, the composite failure is initiated, and the matrix failure is the first incident to notice, as shown in **Fig 7.6 (b).** The **Fig 7.6 (b1)** shows a finite element analysis image of the corresponding stress level and the evolved Hashin damage variable indicating matrix tension failure. Fibre tension failure occurs at nearly the same ultimate stress level in both GLARE laminates. Finite element analysis does not show a fully developed delamination (CSQUADSCRT) variable at interface layers, *i.e.,* metallic to composite layers or composite to composite layers. Quadric traction behaviour between the cohesive surfaces is observed to be more between aluminium alloy to composite layer than between the other composite to composite layers, as shown in **Fig 7.6 (d)**, **(e)** and **(f).** In the aluminium alloy yielding event, a 20.4 % increase in yield strength is noted, while in matrix failure occasion, 21.6% growth in strength is observed in GLARE laminate tailored with optimized aluminium alloy when comparing both GLARE laminates.

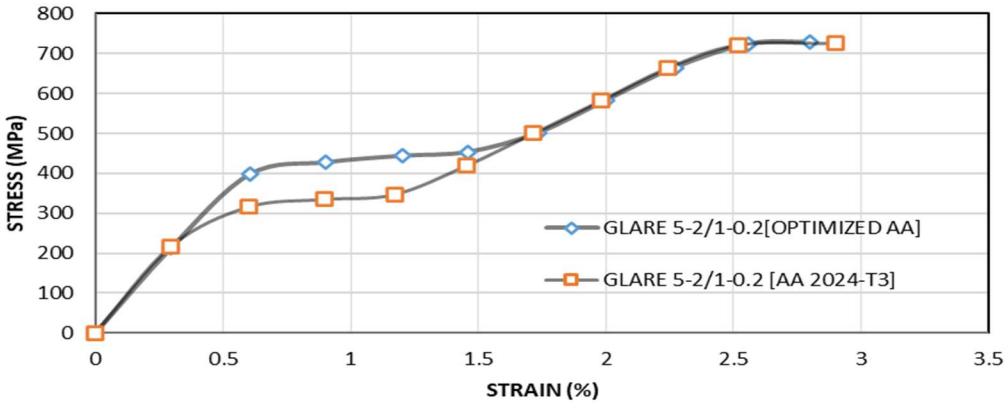

Fig 7.5 Stress-strain comparison curve of GLARE 5-2/1-0.2 laminate

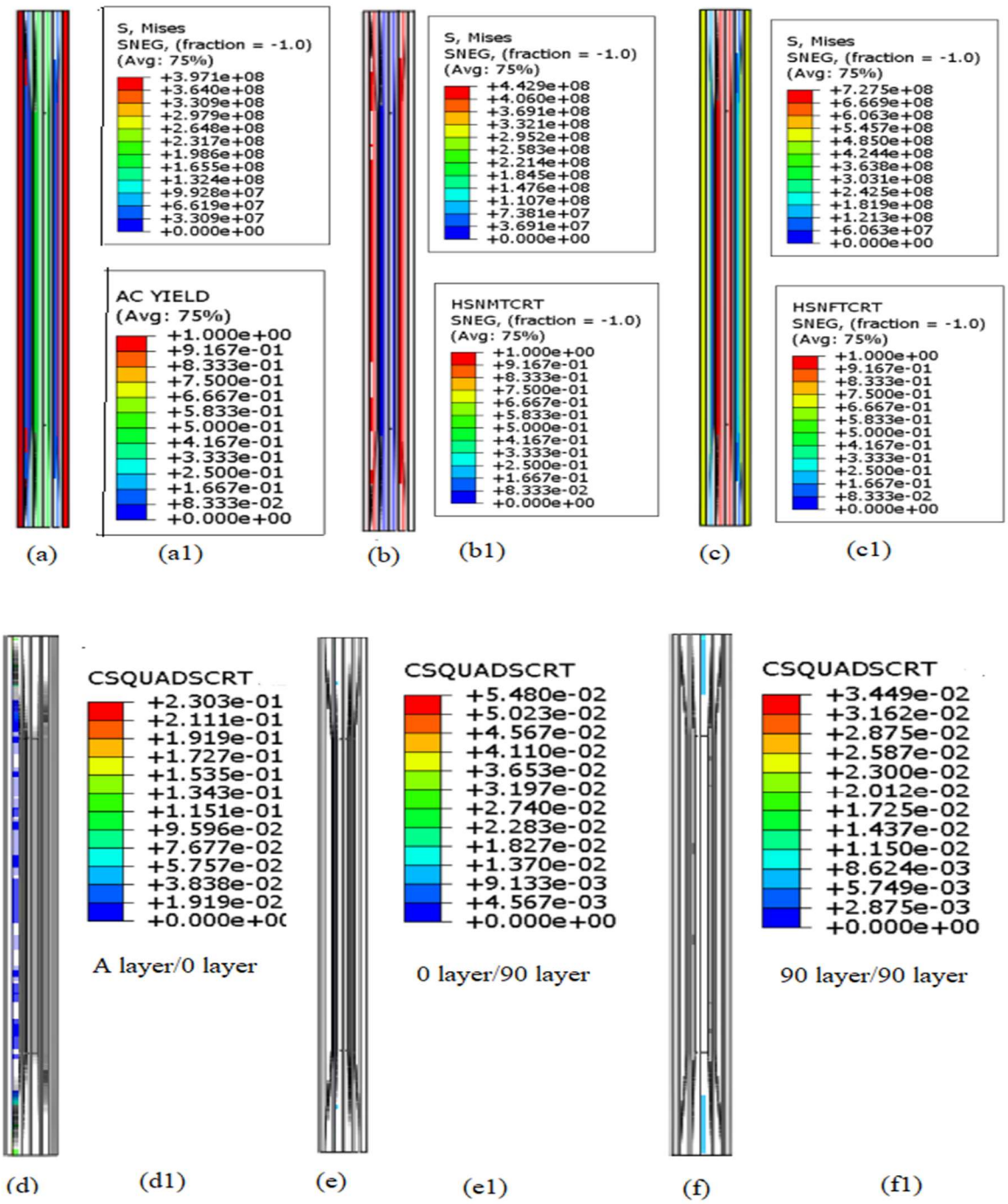

Fig 7.6 Failure events of GLARE 5-2/1-0.2 laminate (a) AA yielding (b) Matrix failure (c) Fibre failure (d) (e) and (f) delamination at different layers

Response of GLARE 3-3/2-0.2 laminate

The stress-strain plot for GLARE 3-3/2-0.2 laminates is shown in **Fig 7.7.** The stress-strain curve of both GLARE laminates exhibited a similar initial slope up to a point. However, after a point, the slope changes due to metal yielding. **Fig 7.8** shows different failure events for GLARE 3-3/2-0.2. The matrix tension damage initiation was the next

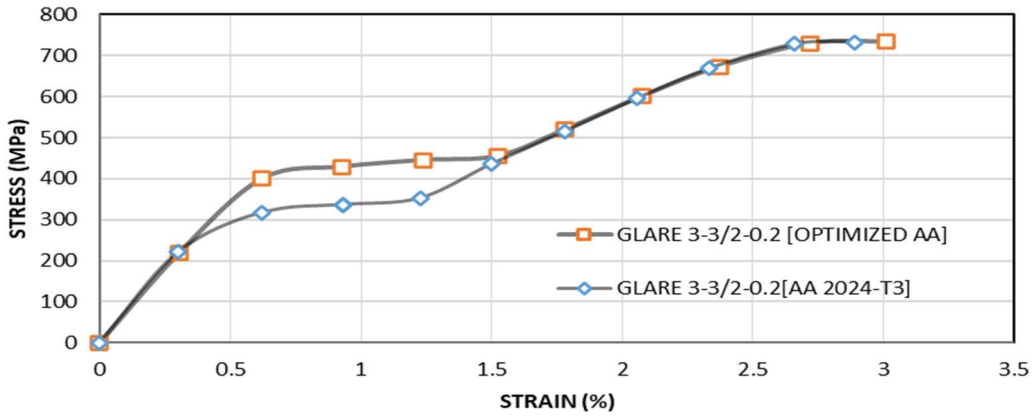

Fig 7.7 Stress-strain comparison curve of GLARE 3-3/2-0.2 laminate

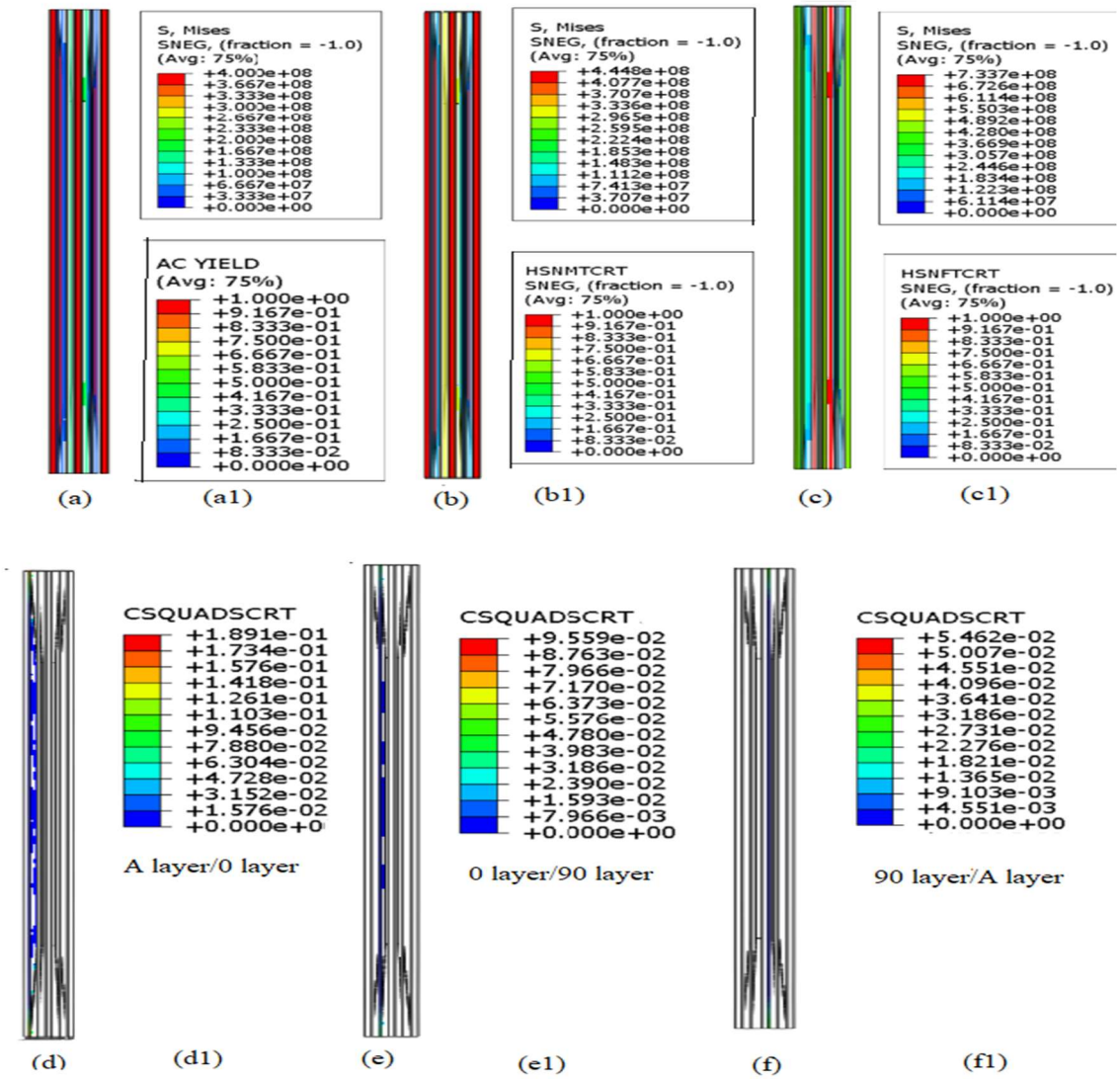

Fig 7.8 Failure events of GLARE 3-3/2-0.2 laminate (a) AA yielding (b) Matrix failure (c) Fibre failure (d), (e) and (f) delamination at different layers

event, as shown in **Fig 7.8 (b)**, followed by fibre tension failure, as shown in **Fig 7.8 (c).** Compared to conventional GLARE laminate, the matrix tension failure in new GLARE laminate occurred at a higher stress magnitude. As the matrix was not the principal load conveying element in the GLARE laminate, its damage is not indicated by an apparent shift in the stress-strain plot. The fibre tension failure is initiated when the ultimate strength of GLARE laminate has arrived. Quadric traction behaviour between the cohesive surfaces is observed to be more between Al to composite layer, as shown in **Fig 7.8 (d)**, and this value is noticed to be lower than GLARE 5-2/1-0.2 laminate. The delamination variable for cohesive surfaces between composite layers, as shown in **Fig 7.8 (e)**, is higher than for GLARE 5-2/1-0.2 laminate. In the yielding aluminium event, a 21.7 % increase in yield strength is noticed, while in matrix failure occasion, 18.4 % growth in strength has been observed in new GLARE laminates when comparing both GLARE laminates.

Response of GLARE 5-2/1-0.4 laminate

The stress-strain plot of GLARE 5-2/1-0.4 laminates is shown in **Fig 7.9**. Like the other two laminates, the point at which the aluminium layer yields exhibited a significant improvement from stress level 318 MPa to 400 MPa, followed by matrix failure at stress magnitude of 353 MPa to 445 MPa. Fibre failure initiated at almost the same ultimate stress values. GLARE 5-2/1-0.4 laminate displayed a different strain behaviour than the other two laminates. This laminate showed the maximum strain (5.4%) for the same displacement rate. Quadric traction behaviour between the cohesive surfaces is observed to be more between composite-to-composite layers than between aluminium to composite layers, as seen in **Fig 7.10 (d), (e)** and **(f).** The CSQUADSCRT variable displayed higher values between all interface layers than the other two laminates. But when subjected to impact, comparatively less delamination is observed in GLARE laminates having all composite layers arranged together. This is considered to be due to fibre bridging. In the yielding aluminium event, a 20.5 % increase in yield strength is noticed, while in the matrix failure incident 20.67 % rise in strength has observed when comparing both GLARE laminates. It has also been noted that the GLARE 5-2/1-0.4 shows a 49.6% improvement in tensile toughness or energy absorption capability till failure than the other two laminates for the same displacement rate. **Table 7.4** summarises the comparison of the failure events of the three different GLARE laminates, which are tailored with optimized AA and with AA 2024-T3.

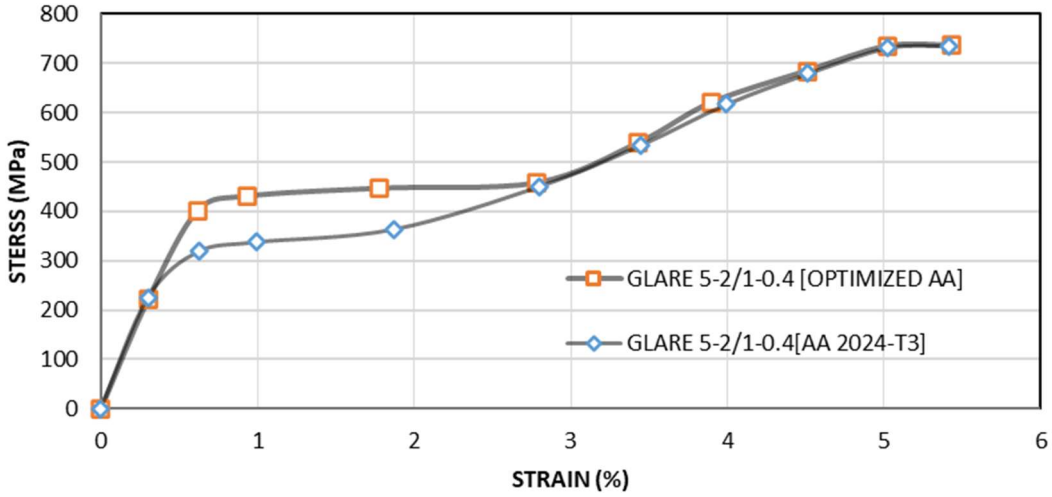

Fig 7.9 Stress-strain comparison curve GLARE 5-2/1-0.4 laminate

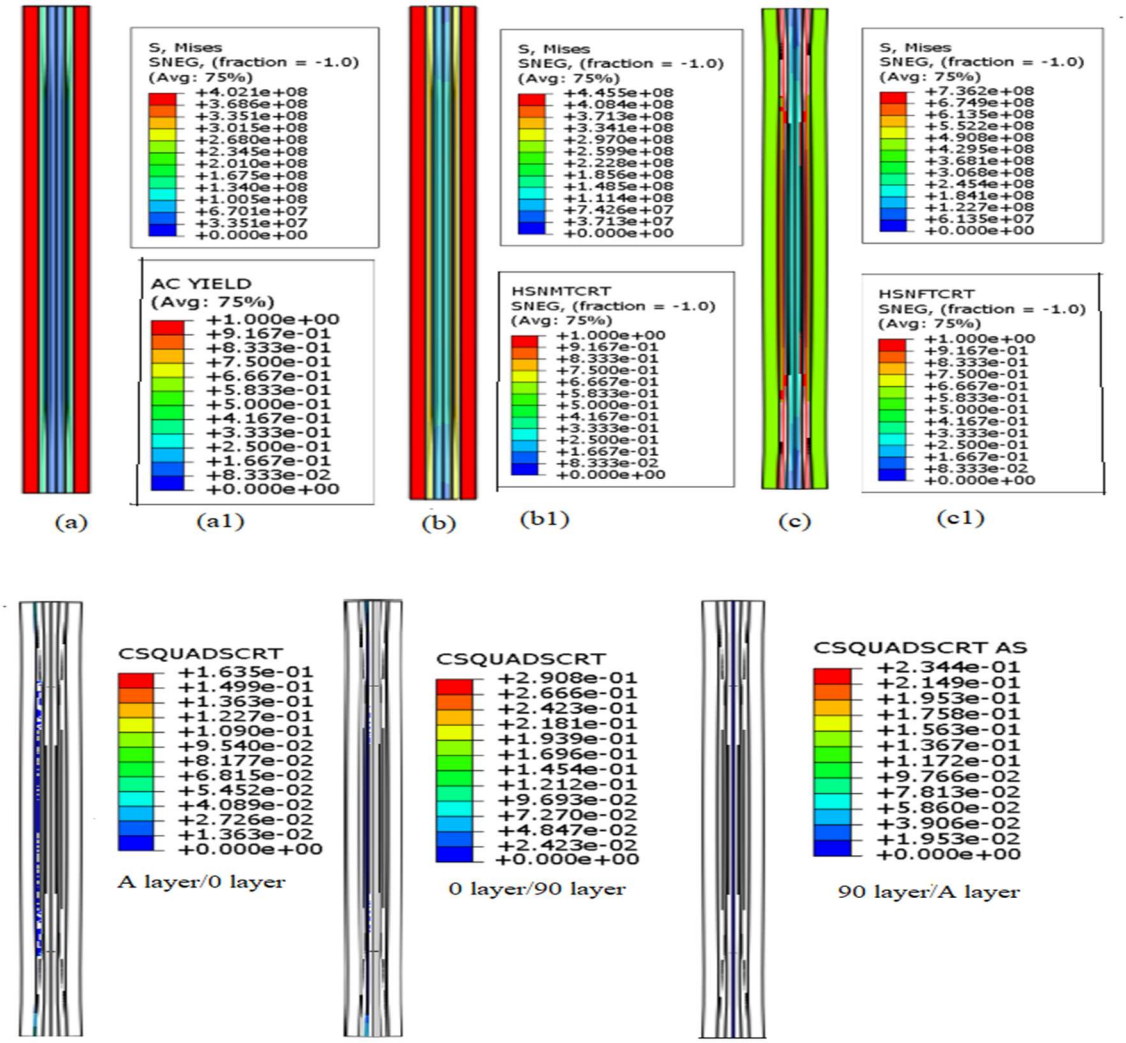

Fig 7.10 Failure events of GLARE 5-2/1-0.2 laminate (a) AA yielding (b) Matrix failure (c) Fibre failure (d), (e) and (f) delamination at different layers.

Table 7.4 Summary of the comparison of GLARE laminates

	GLARE 5-2/1-0.2 laminate		GLARE 3-3/2-0.2 laminate		GLARE 5-2/1-0.4 laminate	
	Optimized AA	AA 2024-T3	Optimized AA	AA 2024-T3	Optimized AA	AA 2024-T3
Stress at aluminium yields (MPa)	397	316	400	319	402	318
Stress at matrix failure (MPa)	443	347	442	364	446	353
Stress at fibre failure (MPa)	728	726	734	733	736	735
Strain at ultimate stress	0.028	0.0278	0.0301	0.0284	0.0543	0.0541

This chapter aimed to investigate the effect of optimized aluminium alloy material parameters on the properties of GLARE laminates. The tension test simulations verified the improvement of the energy absorption characteristics of the GLARE laminates tailored with the optimized aluminium alloy. GLARE laminates with different metal stacking sequences and metal thicknesses are tailored with optimized AA and conventional AA 2024-T3. A series of tension test simulations are conducted to examine the strength and damage behaviours of the GLARE laminates. After full loading, the GLARE laminates tailored with AA 2024-T3, *i.e.,* GLARE 5-2/1-0.2 laminate, GLARE 3-3/2-0.2 laminate and GLARE 5-2/1-0.4 laminate, showed percentage elongations of 2.78 %, 2.84 % and 5.41%, respectively. Whereas, the GLARE laminates tailored with optimized AA, *i.e.*, GLARE 5-2/1-0.2 laminate, GLARE 3-3/2-0.2 laminate and GLARE 5-2/1-0.4 laminate, showed elongations of 2.8 %, 3.01 % and 5.43 %, respectively. The GLARE laminate with a thicker metal layer showed a higher percentage of elongation. This response is considered to be due to higher metal yielding. The aluminium layer started yielding at stress levels that are 20.4 %, 21.7 % and 20.5 % higher in GLARE 5-2/1-0.2, GLARE 3-3/2-0.2 and GLARE 5-2/1-0.4, respectively while comparing the relative stress points noticed in GLARE laminates tailored with AA 2024-T3. The matrix tension failure event is originated at stress points that are 21.6%,18.4% and 20.67% higher in GLARE 5-2/1-0.2, GLARE 3-3/2-0.2 and GLARE 5-2/1-0.4 laminates when comparing the relative stress levels noticed in

conventional GLARE laminates. All GLARE laminates have nearly the same ultimate strength under fibre failure conditions, regardless of metal thickness, and stacking sequences. It has been observed that the GLARE 5-2/1-0.4 laminate with optimized AA showed a 49.6% improvement in tensile toughness or deformation energy than the other two laminates for the same displacement. Delamination started in all interface layers of GLARE laminates, but complete delamination is not seen between any layers in any laminates.

Fibre tension failure eventually occurred at the ultimate stress level, and the stress decreases after fibre breakage. It is essential to understand the behaviour of composite structures under soft body impact loading. The GLARE laminate with thicker metallic layer (GLARE 5-2/1-0.4 laminate) showed a different stress-strain curve compared to other two laminates. One more laminate (GLARE 5-2/1-0.6), which have more thickness in metal layer is selected to study the effect of metal thickness during soft body impact simulation, In the next chapter, soft body impact simulations have carried out on four different fibre metal laminates whose total metal layer thickness are same. Then observed the influence of metal thickness and stacking sequences on soft body impact response and damage behaviour of GLARE laminates.

Chapter 8

Soft body impact analysis on GLARE laminates

8.1 Introduction

This chapter investigate the strength and damage behaviour of different GLARE laminates subjected to soft body impact. The GLARE laminates have different metal thicknesses, fibre orientations, and stacking sequences, while total thickness remains same. The GLARE 5 and GLARE 3 are the laminates considered for this study which are designed for impact resistance. These configurations offer excellent energy absorption (Asundi and Choi 1997).), good out-of-plane impact resistance (Sadighi et al. 2012), and low manufacturing costs compared to the other GLARE laminates. Since soft body impact is a non-linear transient phenomenon. It is challenging to monitor experimentally, especially damage initiation and propagation in the laminates. Such internal cracks can grow severely as the structure becomes less solid and less stable. Hence, the damage due to soft-body impact on aircraft structure requires more observation and understanding to develop better impact-resistant materials. However, the researchers have not done a comparative study within the different GLARE laminates to study the interlayer failure and delamination in the laminates. Here, an attempt is made to investigate the damage resistance of GLARE laminates due to soft body impact. This study helps the design engineers to tailor the laminate configuration according to this particular loading requirements.

This study considered four GLARE laminates each have equal overall thickness as given in **Table 8.1**. The analysis compared the damage and strength behaviours between the four GLARE laminates. The GLARE laminates with aluminium alloy layers resist damage by dissipating energy due delamination at the metal/composite interface, frictional dissipation, metal plasticity, shear failure of the metal layers, fibre failure, matrix failure, etc. Damage energy studies is conducted to investigate the amount of energy dissipated for

various failure modes such as delamination, matrix cracking, fibre failure, etc. As the fibre metal laminate is designing for the wing leading edges, the reaction force at support and centre node deflection is also studied.

8.2 Finite element model validation procedure

Due to insufficient research reports on the effect of soft bodies on GLARE laminates, the GLARE laminate model is validated by the rigid body impact experimental test on the GLARE laminate by Khan *et al.* (2020). Rigid body and laminate layers are created in the ABAQUS part module. The finite element model of a GLARE 5-2/1 laminate and rigid body is shown in **Fig 8.1**. The GLARE considered has a configuration of GLARE 2/1-0.6 with a total thickness of 3.55 mm. The rigid body is modelled as shown in **Fig 8.1**. The mass (16.7 g) and inertia are applied to the reference point, and the location of the reference point is at centre of gravity of the rigid body, as shown in **Fig 8.1**. The GLARE laminates are modelled to be deformable, and local material orientations are applied to each layer. The material parameters of AA 2024-T3 are selected from the literature (Johnson and Cook 1983). The material parameters of AA 2024-T3 are given in the **Table 4.1**. The material parameters of S2 glass and epoxy layers are given in **Table 7.1** and **Table 7.2**, respectively. It is to be observed that as the GLARE laminates are symmetric. Therefore, the delamination nucleating between the interfaces shall be symmetric (Khan *et al.* 2020). Therefore, the quadric portion of the finite element model is adequate to analyse the impact response and damage behaviour of the laminate. Composite layers are discretised with SC8R continuum shell elements, and metal layers have discretised with C3D8R solid elements. The SC8R continuum shell element has the ability to numerically simulate systems that are globally three-dimensional but locally planar (Nguyen *et al.* 2005). The impact region of these layers is meshed with refined elements of size 0.2x0.2x0.2 mm^3, while the non-impact region has meshed with coarse size elements of size 0.5x0.5x0.5.mm^3. Two elements are applied in the thickness of each laminate layer to make the results to be mesh independent (Fan *et al.* 2011; Sadighi *et al.* 2012; Zhu and Chai 2012). The laminate boundary is then fixed with zero degrees of freedom with the encastre boundary condition offered by the finite element software ABAQUS/Explicit. The rigid body is assigned an initial velocity by placing it slightly away from the GLARE laminate to observe its first impact indentation. Hard contact is assigned to the impactor and top layer of the laminate to avoid penetration of the impactor to the target. The interaction

between the layers is achieved through general contact constraints with friction-based cohesive behaviour. Hard contact with pressure overclosure and a coefficient of friction of 0.3 is used between the rigid body and top surface of fibre metal laminates, while a coefficient of friction of 0.7 is applied between the composite plies in different orientations (Shi and Soutis 2014). The rigid body is impacted on the GLARE 5-2/1 laminate with layers of S2 glass/epoxy prepreg with [0/90/90/0] orientation stacked between layers of aluminium alloy (AA 2024-T3), with different impact energies.

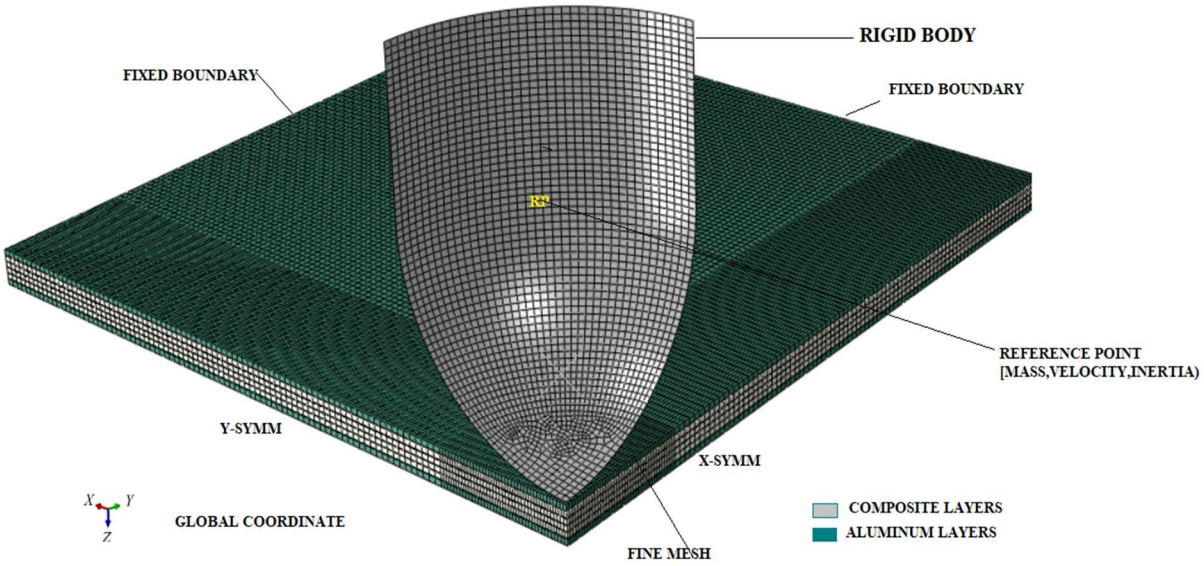

Fig 8.1 Finite element model of GLARE 5-2/1-0.2 laminate with rigid body

8.3 Comparison of soft body impact on GLARE laminates

With the validated soft body and GLARE laminate models, soft body impact analysis is performed on four GLARE laminates to compare their damage behaviours. GLARE laminates are modelled with different layup sequences and metal thicknesses while keeping the overall thickness the same. The details of GLARE laminates under consideration are listed in Table 8.1. The GLARE 5 and GLARE 3 are the laminates considered for this study which are particularly designed for impact resistance. The selected GLARE laminates are impacted with the validated soft body model at a velocity of 117 m/s.

Table 8.1 Details of GLARE laminates considered for impact analysis

Configuration	Lay-up sequence	Aluminium thickness (mm)	Total thickness (mm)
GLARE 5-2/1-0.2	A2/0/90/90/0/A2	0.2+0.2	1.7
GLARE 3-3/2-0.2	A2/0/90/A2/90/0/A2	0.2+0.2+0.2	1.7
GLARE 5-2/1-0.6	A6/0/90/90/0/A6	0.6+0.6	1.7
GLARE 5-2/1-0.4	A4/0/90/90/0/A4	0.4+0.4	1.7

8.4 Results and discussions

8.4.1 Finite element model validation

The GLARE laminate model is validated by comparing maximum centre node deformation on the rear face of the laminate obtained from both experiment tests [Khan *et al.* 2020] and numerical simulations, which are presented in **Table 8.2.** The failure of GLARE laminates is estimated by the failure of a centre node of the outer layer of the laminate. No such failures are detected in experimental tests and simulations. The deformation values are very close to the experiment test values, as shown in **Table 8.2**. The delamination propagation between the layers of the GLARE laminate at the 30 J impact energy level is shown in **Fig 8.2**. The delamination variable CSQUADSCRT evolved at the initial impact stage in both 30 J and 60 J impact energy levels. The interfacial delamination is also compared with the experimental tests by khan *et al.* (2020).

The fibre metal laminates show different failure modes like matrix tension failure, fibre tension failure, matrix compression failure and matrix tension failure. *etc*. The major failure modes *i.e.,* matrix tension failure (HSNMTCRT), fibre tension failure (HSNFTCRT), matrix compression failure (HSNMCCRT) and fibre compression failure (HSNFCCRT) are fully evolved during times of 1.5 ms,3 ms,1 ms,1.5 ms, respectively. The cross-sectioned images of GLARE 5- 2/1-0.6 laminates failure modes are shown in **Fig 8.3 (a, b, c and d)**. As seen in the **Fig 8.3 (a),** fibre compression damage is not intense

Table 8.2 Centre node displacement at rear face of the laminate at different impact energies

Impact energy	GLARE 5-2/1-0.6	
	Maximum deformation in mm	
	Experiment test (Khan *et al.* 2020)	Numerical analysis
30 J	4.82	4.87
60 J	7.56	7.82

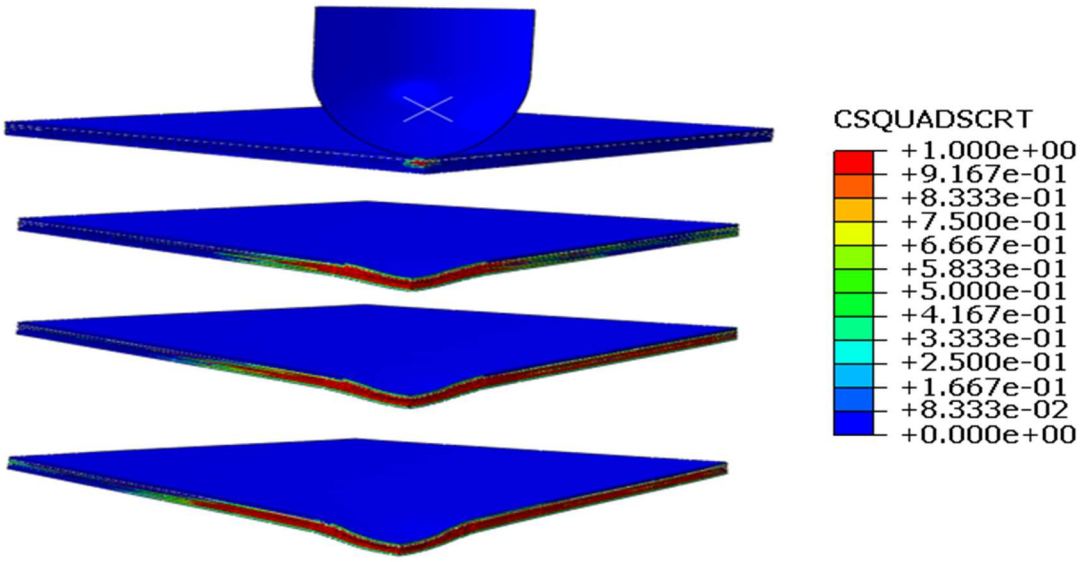

Fig 8.2 Delamination propagation between the laminate layers at 30 J impact

and does not propagate. Fibre tensile failure is more substantial than fibre compression failure, but only at the impact location. The matrix compression failure is propagating across the fibre direction. Matrix tension is considered the most severe failure, and it propagates in the fibre direction till support. The shear damage is fully evolved at 7 ms of the impact duration and is enclosed to the impact region only. Comparing failure modes and delamination for the two impact energy levels shows good agreement between

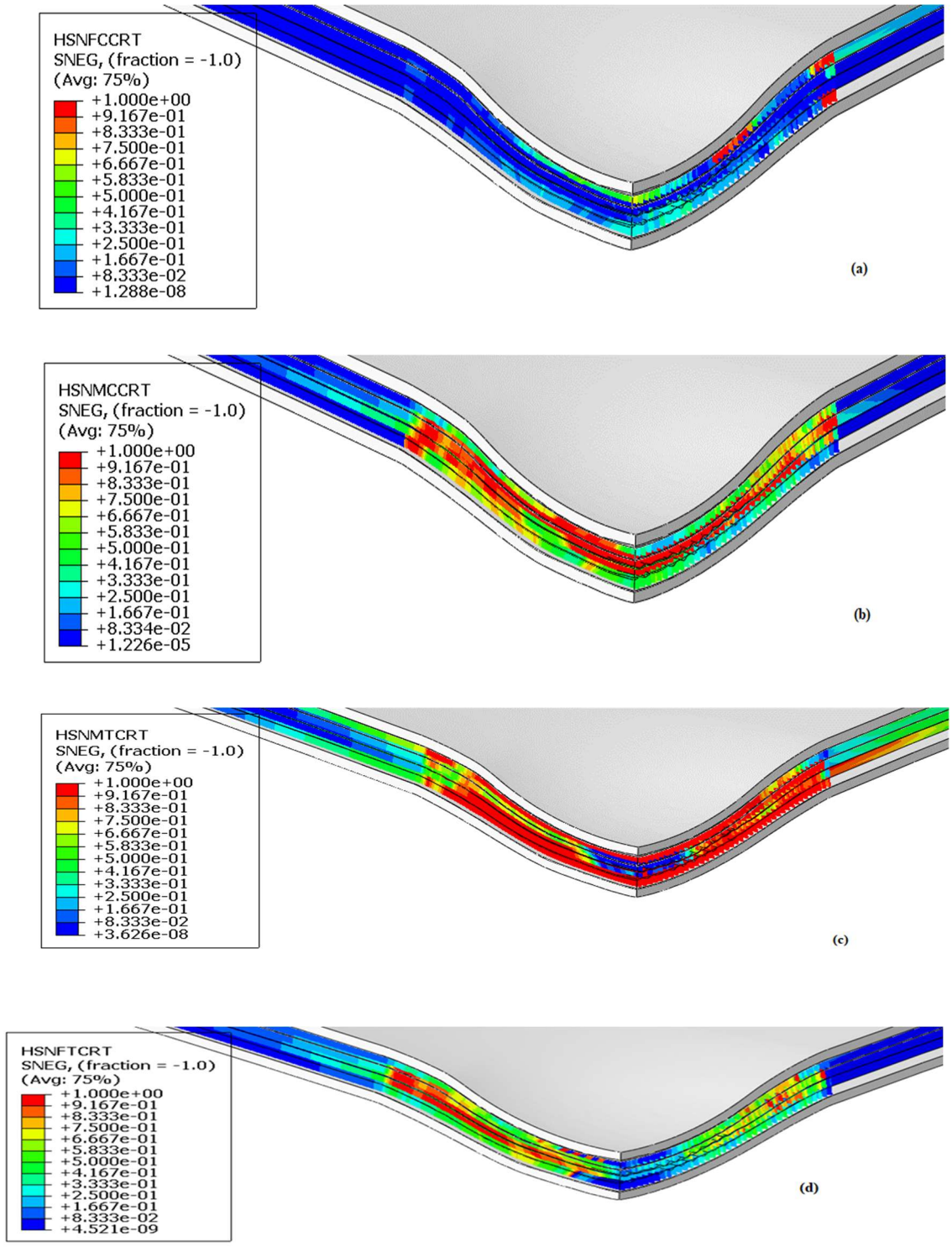

Fig 8.3 Failure modes in composite layers at 30 J impact (a) fibre compression failure (b) matrix compression failure (c) matrix tension failure (d) fibre tension failure.

simulation and experimental testing. The finite element model of GLARE laminates is therefore validated and selected for soft body impact analysis studies of different GLARE laminates.

8.4.2 Comparison of soft body impact analysis on GLARE laminates

The focus of the comparison of soft body impact analysis on GLARE laminates is to select a GLARE laminate specification for a leading edge with better energy absorption, which transmits smaller reaction forces to reinforce structures like spars. At the same time, the deformation of the centre of the wing must also be lowered to protect its internal components. The failures and delamination of the different GLARE laminates also must be considered for the selection of the laminate for the design of leading edges.

To analyse the effect of soft body impact on different GLARE laminates, the previously validated soft body model is impacted on the GLARE laminates with a velocity of 117 m/s. In soft body impact events, the main sources of energy dissipation are aluminium yielding, matrix damage, fibre damage, and delamination. These damage events ultimately reduce the additional load-carrying capacity of the laminate, so it is essential to analyse the growth of damage mechanisms to understand their onset and evolution under specific loading conditions. The study carefully analyses the damage behaviour of each impact event by examining dissipated energy, reaction forces at supports, centre displacement, matrix failure, fibre failure, delamination, and more.

Energy dissipation analysis

When the soft body impacts the target, it transfers all its energy to the target, and the target stretches with the soft body. An amount of energy transferred to the GLARE laminate is dissipated with different energy dissipation phenomena during the event i.e., damage dissipation energy, frictional dissipation energy, and plastic dissipation energy. This energy dissipation reduces the stiffness of the GLARE laminates, but it supports the laminates against sudden failure. Knowing the energy dissipation levels helps design engineers classify different GLARE laminates according to their requirements. Since each laminate layer is connected, it is complicated to scrutinise this energy dissipation through experimental testing. The finite element simulation helps to reveal the energy dissipation mechanisms which is helpful in gaining a deep understanding of the impact behaviour of the GLARE laminates.

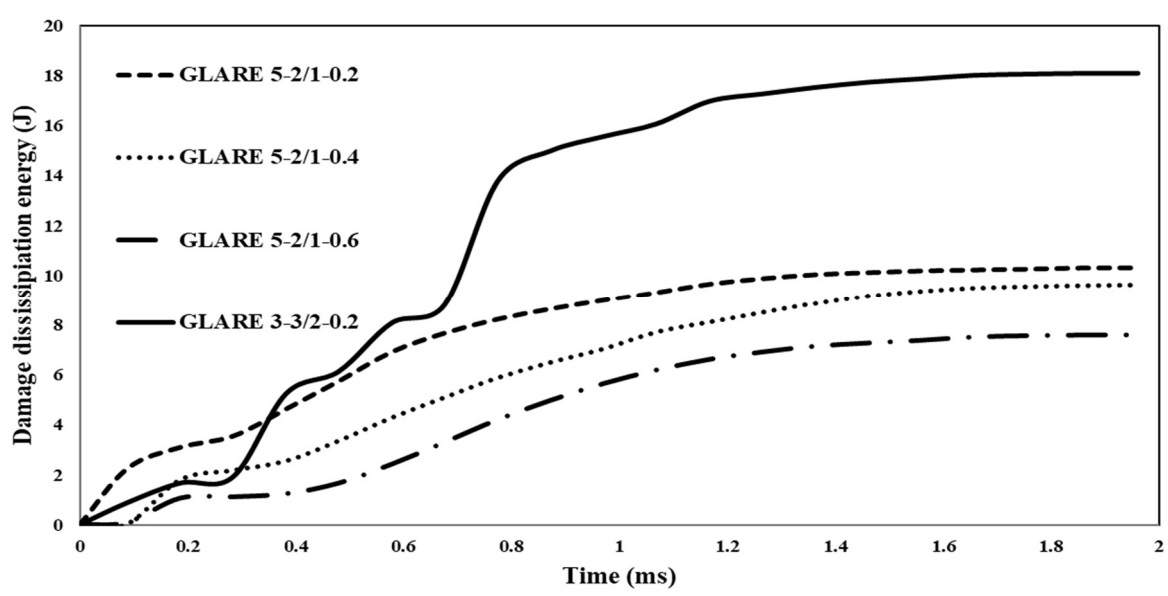

Fig. 8.4 Damage dissipation energy histories of different GLARE laminates

The energy dissipation due to damage in GLARE laminates is mainly due to metal layer cracking, fibre failure and matrix failure. In analysing the soft body impact results for the four GLARE laminates, it is understood that none of these laminates exhibited fully evolved metal layer or fibre failures. In all GLARE laminates, delamination is the main damage energy dissipation phenomenon, followed by matrix failure. The **Fig 8.4** shows the damage dissipation energy histories of GLARE laminates during soft-body impact. Maximum damage energy dissipation of GLARE 3-3/2-0.2 laminate, GLARE 5-2/1-0.2 laminate, GLARE 5-2/1-0.4 laminate and GLARE 5-2/1-0.6 laminate is 18.085 J,10.325 J,9.615 J and 7.605 respectively. The GLARE laminate tailored with a metallic layer inside (GLARE 3-3/2-0.2) showed a different dissipation energy pattern, while the other three laminates exhibited the same pattern. The GLARE 3-3/2-0.2 laminate showed the highest damage energy dissipation due to the higher volume fraction of the matrix, in the placement of the metal layer in between the composite layers. GLARE laminate with a thicker metallic layer (GLARE 5-2/1-0.6) showed the lowest damage energy dissipation, as the volume fraction of the matrix is lower than other laminates.

Reaction force versus time

The reaction force of all GLARE laminates is extracted from constrained nodes at support, and the results are plotted in **Fig 8.5.** The results show that GLARE 3/2-0.2, in which an aluminium alloy layer separates two adjacent glass/epoxy layers with different

fibre orientations, exhibits the highest reaction force, which is oscillatory at peak levels. This response may be due to the elastic recovery of the metal layers between the composite layers. GLARE 5-2/1-0.6 with glass/epoxy layers aligned together showed a lower reaction force than other GLARE laminates. All GLARE 5 configurations show the same reaction force pattern, while GLARE 3 shows a different pattern with higher oscillations. It is found that the placement of the thicker metal layer on top of the laminate minimizes the reaction force. When the thickness of the metal layer decreases, the reaction force at the support increases.

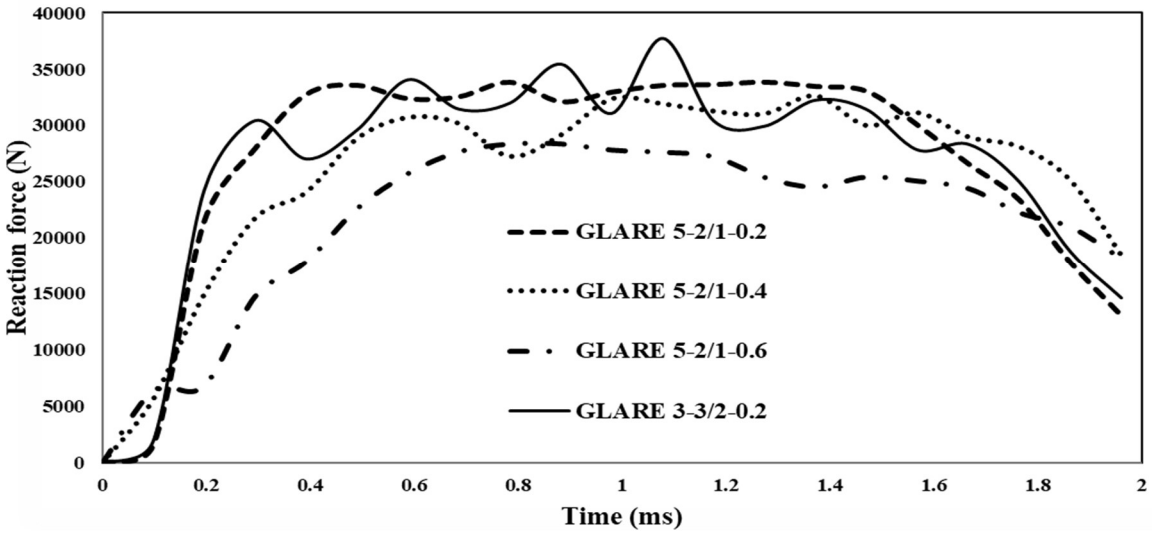

Fig 8.5 Reaction force variation of GLARE laminates at different times of soft body impact

Deflection versus time

The deflection of the centre node of the laminate is recorded from the displacement field variable of the output of ABAQUS/Explicit. The **Fig 8.6** shows the displacement plot of the GLARE laminates observed during soft body impact at a velocity of 117 m/s. This lower displacement shows applicability when comparing the four laminates. However, the displacement and reaction forces at high-speed soft body impact are more severe, making comparisons to GLARE laminates difficult. The **Fig 8.6** shows that the centre displacement increases in all cases, reach a maximum value, and then decreases. After full impact, GLARE 5-2/1-0.6 has the highest centre displacement. GLARE 5-2/1-0.2 and GLARE 3-3/3-0 showed the lowest and almost the same displacement. When comparing the reaction force and deflection, it is understood that the configuration, which exhibits the highest

reaction force showed the lowest displacement and vice versa. GLARE laminates with thicker metal layers exhibit higher centre displacement. This response may be due to higher metal plasticity**.**

The displacement contour plots of the soft body and the GLARE laminate after full impact are shown in **Figs 8.7 (a,b,c and d)**. In GLARE 3 3/2-0.2 laminate, the deformation of the top layer propagates to the supports. It can see that in **Fig 8.7 (d)** the corners of this laminate are deflected back and separated from the bottom layers. It can also observe from **Figs 8.7 (a), (b)** and **(c)** that the deformation increases when the thickness of the metallic layer increases. The area of deformation propagation of GLARE 5-2/1-0.4 and GLARE 5-2/1-0.6 laminate is higher than GLARE 5-2/1-0.2 laminate. Soft bodies spread more in laminates with the lower metal thickness (GLARE 5-2/1-0.2 and GLARE 3 3/2-0.2), as shown in **Figs 8.7 (a)** and **(d).** It can be inferred that thinner metal layers exhibit greater elastic recovery than thicker metal layers in soft body collisions.

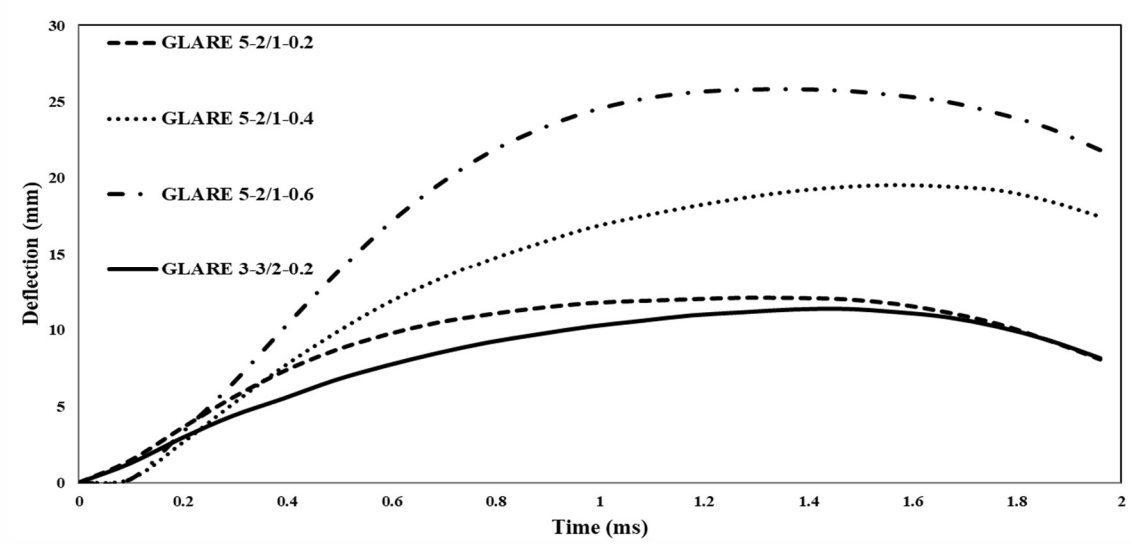

Fig 8.6 Displacement variation of GLARE laminates at different times of soft body impact

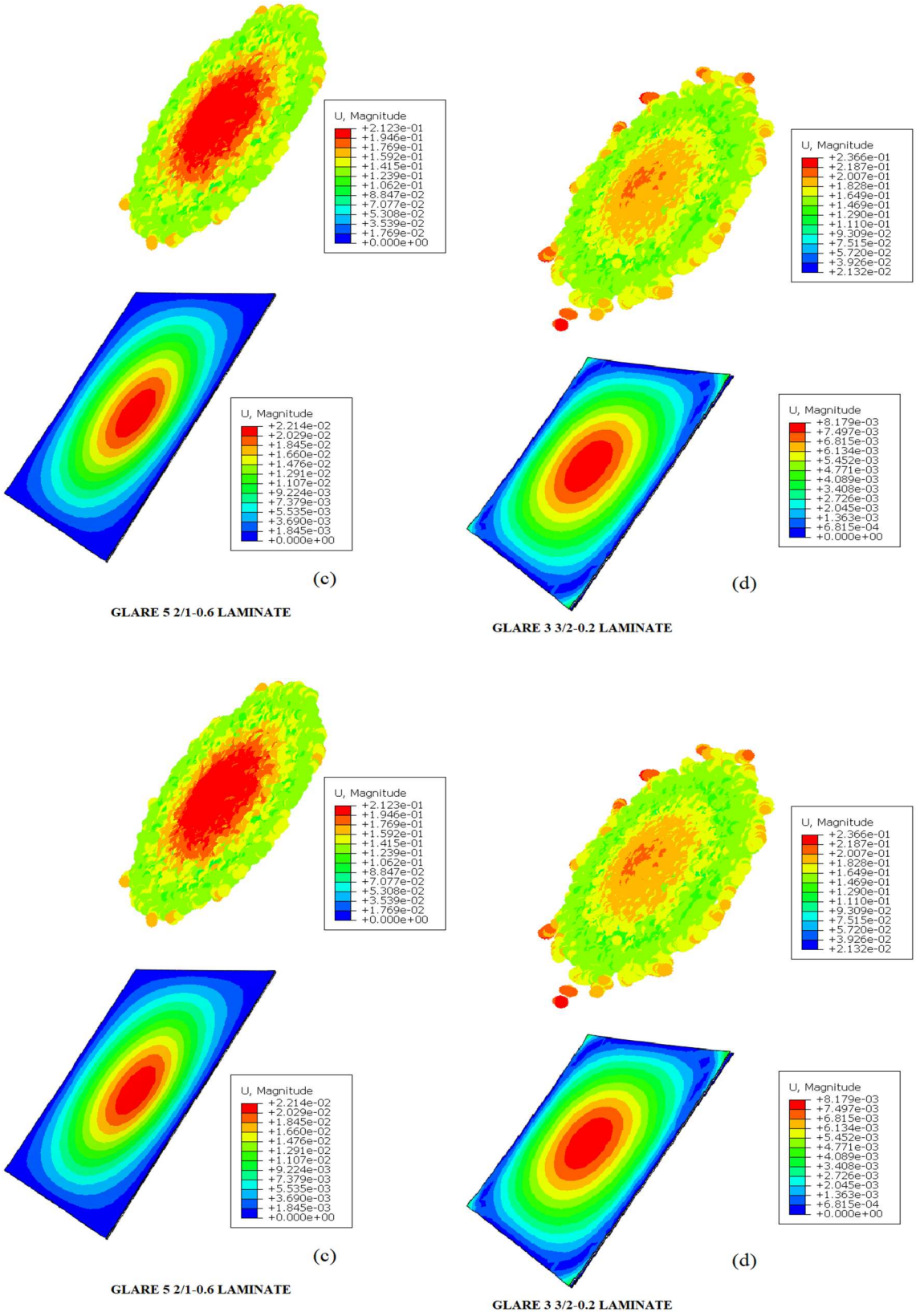

Fig 8.7 Deformation propagation of the soft body and (a) GLARE 5 2/1-0.2 (b) GLARE 5 2/1-0.4 (c) 5 2/1-0.6 (d) GLARE 3 3/2-0.2 laminates after complete impact.

Failure modes

GLARE laminates exhibit different failures during impact, such as metal failure, matrix failure, fibre failure, and delamination, which are discussed in this section. The Hashin failure criteria define composite failure modes as four failure indices *i.e.,* fibre tensile failure (HSNFTCRT), matrix tensile failure (HSNMTCRT), fibre compression failure (HSNFCCRT), and matrix compression failure (HSNMCCRT). The failure index varies from zero to one. In GLARE 5-2/1-0.2, the failure indices of HSNFTCRT, HSNFCCRT and HSNMCCRT varied from zero to 0.058,0.191 and 0.343 respectively. The matrix failure initiated at 0.098 ms,when the matrix tension stress exceeds its failure strength. In GLARE 3-3/2-0.2 laminate, the failure indices of HSNFTCRT and HSNFCCRT varied from zero to 0.967 and 0.383 respectively. The matrix failure initiated due to tension stress at 0.098 ms and compression stress at 0.98 ms. In this laminate, fibre failure is about to initiate as the fibre tension failure index is about to reach one. In GLARE 5-2/1-0.4 laminate, the failure indices of HSNFTCRT, HSNFCCRT and HSNMCCRT varied from zero to 0.161,0.207 and 0.372 respectively. In GLARE 5-2/1-0.6 laminate, the failure indices of HSNFTCRT, HSNFCCRT and HSNMCCRT varied from zero to 0.2386,0.185 and 0.343 respectively. A fully evolved damage variable for matrix tension failure (HSNMTCRT) is observed in all four GLARE laminates at the initial time of impact time of 0.098ms. GLARE 5-2/1-0.2 laminates showed all failure index values *i.e.*, fibre tensile failure, matrix tensile failure, fibre compression failure, and matrix compression failure, lower than the other three GLARE laminates considered.

The output of the delamination pattern is obtained through the CSQUADSCRT variable available in the output check card of ABAQUS/Explicit. During the initial impact time, the interfacial delamination variable evolved in all the considered GLARE laminates. In the GLARE 5-2/1-0.2 laminate, after full impact, delamination is observed between the centre and corners at top aluminium alloy layer and the glass/epoxy (A/0) interface. However, complete delamination is observed between the (0/90) and (90/0) composite interfaces. The onset of delamination is seen between the composite and the bottom metal layer (0/A) interface, at the centre only, which didn't propagate also, as shown in **Fig 8.8**. GLARE 5 2/1-0.4 laminate, complete delamination is seen between the (0/90) and (90/0) composite interfaces. At the bottom layer of the laminate, the corners of the aluminium layers are delaminated from composite layers, as shown in **Fig 8.9**. Severe delamination is detected between (A/0) interface of GLARE 5 2/1-0.6 laminates, However, complete

delamination is observed between the (0/90) and (90/0) composite interfaces, as shown in **Fig 8.10**. GLARE 3 laminates showed different delamination propagation than GLARE 5 laminates. Between the top aluminium alloy/composite interface, there is severe delamination at the centre and corners of the laminate. Complete delamination is observed between the 0/90 composite interface. The other four interfaces showed the same delamination pattern, and the separation of layers is observed only at the corners, as shown in **Fig 8.11**. In this laminate, the interlayer openings and their extent are severe at the corners.

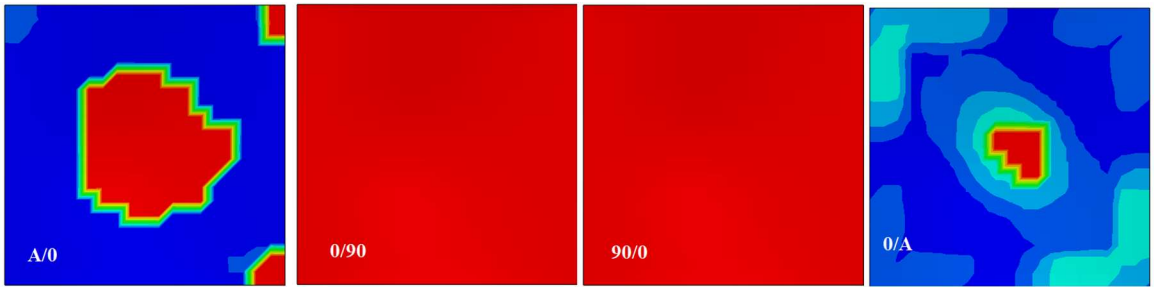

Fig 8.8 Delamination of GLARE 5-2/1-0.2 laminate layers after complete impact

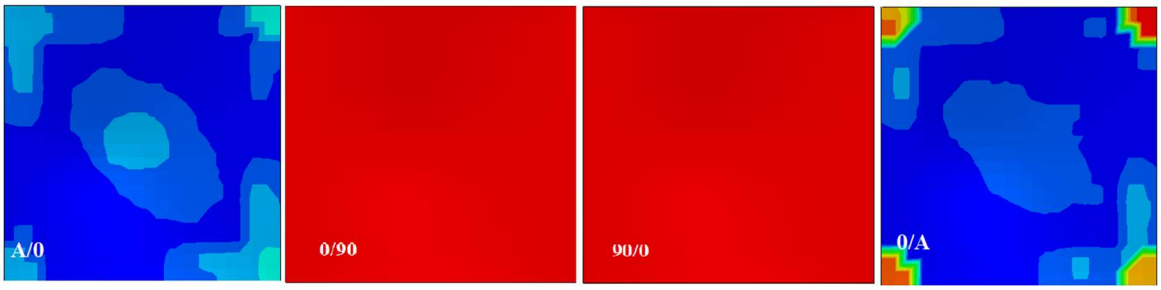

Fig 8.9 Delamination of GLARE 5-2/1-0.4 laminate layers after complete impact

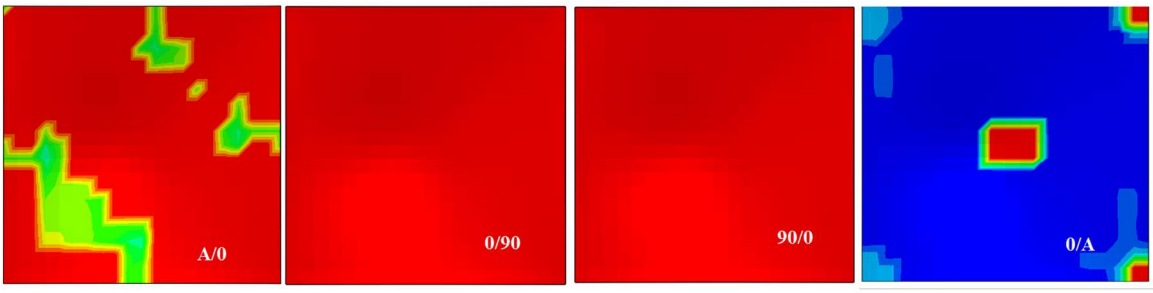

Fig 8.10 Delamination of GLARE 5-2/1-0.6 laminate layers after complete impact

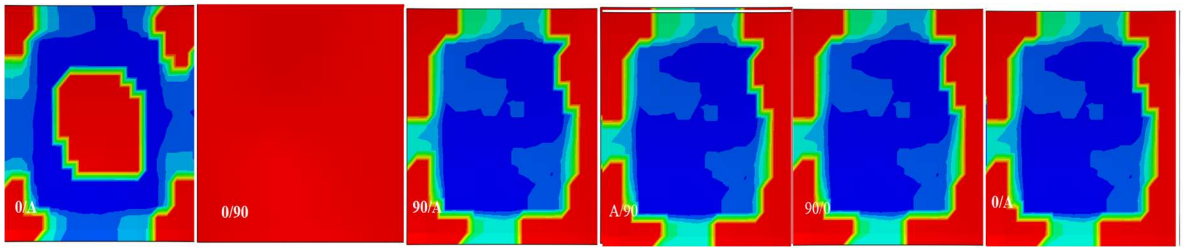

Fig 8.11 Delamination of GLARE 3-3/2-0.2 laminate layers after complete impact

In this chapter, four GLARE laminates subjected to high velocity soft body impact are analysed to predict their impact responses and damage behaviours. Four GLARE laminate specimens are selected with different metal thickness and stacking sequences, while keeping the total metal layer thickness as constant. The results concluded that the GLARE laminate with thicker metal layer exhibited the lowest reaction force but the highest deflection. This highest deflection is considered to be due to increased metal plasticity. The distribution of the metallic layer inside the layup reasons for oscillations at peak force. This response is considered to be due to the elastic recovery of the metallic layer between the composite layers. When comparing the result values of reaction force and centre deflection, it is understood that the GLARE laminate configuration which exhibits the highest reaction force showed the lowest displacement and vice versa. GLARE 5-2/1-0.2 laminates showed all failure index values *i.e.*, fibre tensile failure, matrix tensile failure, fibre compression failure, and matrix compression failure, lower than the other three GLARE laminates considered. It is found that the distribution of metal layer inside the layup lowers the impact resistance of GLARE 3-3/2-0.2. In this laminate, fibre failure is about to initiate as the fibre tension failure index is about to reach one. Moreover, the interlayer openings and their extent are severe at the corners. The results concluded that glass/epoxy layers aligned between relatively thin layers of aluminium alloys are best suited for designing leading edges.

Chapter 9

Summary and conclusions

9.1 Summary

The research is carried out to improve the properties of GLARE laminates used for wing leading edges to enhance their soft body impact resistance. An extensive literature survey assessed the progress of soft body impact analysis on aircraft structures over the past 45 years. The literature review concluded that researchers follow no homogeneity or uniformity in soft body modelling approaches. Based on the different finite element software and available modelling methods, researchers used different approaches for selecting material models, discretisation methods, contact formulation, impactor geometry and size. This fact underlines that each piece of literature about this research area has its value. This study analyses three different soft-body modelling methods using the finite element code ABAQUS/Explicit. The three finite element approaches *viz,* Lagrangian, Arbitrary Lagrangian-Eulerian and Smooth Particles Hydrodynamics are compared based on the set-up time, run time, deformation pattern and pressure distribution characteristics. It is understood that each method has its advantages, and none of these methods is free of disadvantages. However, it is concluded that the SPH method with the given equation of state material parameters provides the best correlation with the experimental test based on pressure distribution characteristics and deformation patterns. The Hugoniot and stagnation pressure determined from the SPH simulation is about 44.07 MPa and 6.63 MPa (with error ± 4%), respectively. The leading edges are modelled and meshed with finite element software Altair® Hyper Mesh®. Bird impact simulation on the wing leading edge is carried out with ABAQUS/ Explicit and validated with an soft body impact experimental test at GTRE, Bangalore. The permanent plastic deformation of the wing leading edge specimen without penetration of the impactor is observed both in experiment and simulation. After

the validation, a parametric study test matrix is prepared by varying material parameters of the leading edges: elastic modulus, static yield limit, strain hardening modulus, hardening exponent and Poisson's ratio. Python scripting algorithms are developed based on the parametric study test matrix to automate repetitive tasks. Then, performed soft-body impact simulations on the leading edges by varying the considered material parameters. The parametric study test results are compared based on the reaction force (***RF***) and central displacement (***U***) with varied material combinations. The results summarised that the elastic modulus, static yield limit, strain hardening modulus, and hardening exponent are the most influential parameters on the selected control variables (***RF*** and ***U***). Then, the selected material parameters are optimized and validated with soft body impact analysis on the wing leading edge based on Taguchi's L16 factorial design of experiments combined with grey relational analysis. The optimal combination of material parameters for minimising the reaction force and centre displacement simultaneously are found out as elastic modulus of 72 GPa, static yield limit of 359 MPa, strain hardening modulus of 457 MPa, and hardening exponent of 0.34. From ANOVA, it is understood that elastic modulus and static yield limit are the significant material parameters affecting multi responses because its P-values are 0.039 and 0.037 respectively which is less than 0.05 at a 95% confidence level. But P-values parameters strain hardening modulus and hardening exponent are above 0.05 and do not show much significance on responses. According to standard E8/E8M-11, created tension specimen models of different thicknesses from 0.2 to 0.6 mm. Then, carried out quasi-static tension test simulations, these specimens (optimized aluminium alloy and AA 2024-T3) using the finite element software ABAQUS/Explicit. Analysed the performance improvement of the optimized aluminium alloy by comparing the mechanical properties, *i.e.,* yield strength, ultimate tensile strength, and tensile toughness with aluminium alloy (AA 2024-T3). The optimized aluminium alloy exhibited mechanical property improvement up to an average of 20.84% yield strength, 20% tensile strength, and 25% deformation energy (tensile toughness) compared to AA 2024-T3. When the thickness of the specimen increased all the above properties got decreased. The failure analysis is carried out on the optimized aluminium alloy specimen and found out the ductile damage variables stress triaxiality, strain rate, failure strain and fracture energy from the results. The ductile damage initiation and evolution parameters for the optimized aluminium alloy is calculated from the failure analysis are the fracture strain of 0.1685, stress triaxiality of -1.307, the strain rate of 0.0012/s, and fracture energy of 49.26 kJ/m^2. Conducted tension test simulations on different fibre metal laminates tailored with

optimized aluminium alloy and glass/epoxy layers (GLARE 5-2/1-0.2, GLARE 3-3/2-0.2, GLARE 5-2/1-0.4). The performance of the GLARE laminates is compared with the stress point at the onset of damage (yielding of aluminium, matrix failure, fibre failure) to verify their superiority over GLARE laminates tailored with AA 2024-T3. The aluminium yielding and matrix tension failure occurred at a higher stress magnitude in the GLARE laminates tailored with optimized aluminium alloy compared to GLARE laminates tailored with AA 2024-T3. However, fibre tension failure initiated at approximately the same stress-strain conditions in both laminates. After the matrix failure, the composite layers become the main load-carrying element. Thus, the fibre tension failure initiated at the same stress points for all GLARE laminates in both conditions. The GLARE laminates with a thicker metal layer exhibited increased percentage strain for the same displacement rate as other GLARE laminates. This response is considered to be due to increased metal plasticity. The maximised energy absorption for the same displacement rate is good for the bird impact resistance of aircraft structures. The above property improvement helps to decelerate the soft body (bird) in a controlled motion and absorb the impact energy. But the GLARE laminate intends to be used in the fabrication of leading edges where the reduction of displacement is a major factor in protecting its internal components. Therefore, to analyse other factors that control the damage behaviour, performed soft body impact simulations on specimens with different GLARE laminates (GLARE 5-2/1-0.2, GLARE 3-3/2-0.2, GLARE 5-2/1-0.4, GLARE, 5-2/1-0.6). The influence of metal thickness and stacking sequences of GLARE laminates on soft body impact response are analysed based on reaction forces, centre deflection, damage dissipation energy, matrix failure, fibre failure, and delamination. The results concluded that the thicker metal layer exhibited the lowest reaction force but the highest displacement. This response is considered to be due to increased metal plasticity. The distribution of the metallic layer inside the layup reasons for oscillations at peak force. This response is considered to be due to the elastic recovery of the metallic layer between the composite layers. When comparing the result values of reaction force and centre deflection, it is understood that the GLARE laminate configuration which exhibits the highest reaction force showed the lowest displacement and vice versa. GLARE 5-2/1-0.2 laminates showed all failure index values i.e., fibre tensile failure, matrix tensile failure, fibre compression failure, and matrix compression failure, lower than the other three GLARE laminates considered. It is found that the distribution of metal layer inside the layup lowers the impact resistance of GLARE 3-3/2-0.2. In this laminate, fibre failure is about to initiate as the fibre tension failure index is

about to reach one. Moreover, the interlayer openings and their extent are severe at the corners. The results of soft body impact analysis concluded that glass/epoxy layers aligned between relatively thin layers of aluminium alloys are best suited for designing leading edges.

9.2 Conclusions

The conclusions arrived from the research are summarized below:

1 A comparative study of different soft body modelling methods concluded that the smooth particle hydrodynamics method using the selected Mie-Grüneisen equation of state parameters provided the best correlation with experimental tests based on pressure distribution characteristics and deformation behaviours.

2 A parametric study of the leading edge (HT, VT, and wing) concluded that the static yield limit, elastic modulus, strain hardening modulus, and strain hardening exponent influence the selected control variables (reaction force and centre displacement). The HT and VT profiles exhibit higher reaction forces than the wing leading edge profiles. The VT and HT profiles reported the highest and lowest centre displacements, respectively.

3 The multi-objective optimisation with Taguchi's Design of Experiments combined with grey relational analysis found out the order of the importance of material parameters to multiple responses is static yield limit > elastic modulus > strain hardening modulus > hardening exponent. The analysis of variance showed that the static yield limit and elastic modulus are the most influencing material parameters affecting the selected variables.

4 The optimal combination of material parameters for the simultaneous reduction of reaction force and the centre displacement obtained from the grey relational analysis is the elastic modulus of 72 GPa, static yield limit of 359 MPa, strain hardening modulus of 457 MPa, and hardening exponent of 0.34.

5 The optimized aluminium alloy showed property improvement up to an average of 20.84% in yield strength, 20% in tensile strength and 25% in deformation energy compared to standard AA 2024-T3.

6 The ductile damage initiation and evolution parameters of the optimized aluminium alloy calculated from failure analysis are failure strain of 0.1685, stress triaxiality of -1.307, strain rate of 0.0012 / s and fracture energy of 49.26 kJ/m^2.

7 The conclusions drawn from the simulation results of tensile tests of different fibre metal laminate configurations are summarised as follows:

a) The aluminium layer starts yielding at stress levels which are higher by 20.4%, 21.7% and 20.5% in GLARE 5-2/1-0.2, GLARE 3-3/2-0.2 and GLARE 5-2/1-0.4 laminates, respectively while comparing the relative stress points noticed in conventionally used GLARE laminates tailored with AA 2024-T3.

b) The matrix tension failure event originated at stress points that are higher by 21.6%, 18.4% and 20.67% in GLARE 5-2/1-0.2, GLARE 3-3/2-0.2 and GLARE 5-2/1-0.4 laminates,respectively when comparing the relative stress levels noticed in the conventional GLARE laminates.

c) All GLARE laminates have nearly the same ultimate strength under fibre failure conditions, regardless of metal thickness, stacking sequences, and fibre orientation.

d) It has been observed that GLARE 5-2/1-0.4 laminate with optimized AA has 49.6% improvement in tensile toughness (or deformation energy) over the other two laminates (GLARE 5-2/1-0.2, GLARE 3-3/2-0.2) at the same displacement rate.

e) Delamination started in all interface layers of the GLARE laminates, but complete delamination has not been observed in any layers in any of the laminates.

8 The conclusions drawn from the soft impact analysis of different GLARE laminates are summarised below.

a) The maximum energy dissipation due to different failure modes of GLARE 3-3/2-0.2, GLARE 5-2/1-0.2, GLARE 5-2/1-0.4 and GLARE 5-2/1-0.6 are 18.085 J, 10.325 J, 9.615 J, and 7.605 J, respectively.

b) The GLARE laminates, in which two adjacent glass/epoxy layers separate the aluminium alloy layers (GLARE 3-3/2-0.2), exhibited a higher reaction force at support. The placing of metal layers between the composite layers increases the vibrations at support due to the elastic recovery of the metal layer during impact. GLARE 5-2/1-0.6, the glass/epoxy layers aligned together between metal layers, showed the lowest reaction force than other GLARE laminates.

c) When the thickness of the metallic layer increases, the displacement also increases. This response is considered to be due to the increased metal plasticity. The GLARE laminate with the thinner metal layers (GLARE 5-2/1-0.2) showed the lowest displacement.

d) All GLARE laminates exhibited matrix tension failure at initial impact time itself. GLARE 3-3/2-0.2 laminate exhibited matrix tension and compression failure.

e) At the time of initial impact itself, delamination initiated in all laminates. In all GLARE 5 laminates, complete delamination is observed at the (0/90) and (90/0) composite interfaces. But in the GLARE 3 laminate, complete delamination is only observed at the (0/90) composite interface. All four interfaces below that showed the same delamination pattern which is severe at corners. In this laminate, the interlayer openings and their extent are severe at the corners.

The main design objective is to improve the mechanical properties of fibre metal laminates used for the leading edge of the wing to resist soft body impacts. The analysis is carried out in two parts: The first part of the study concluded that the aluminium alloys with optimized material parameters have significantly improved mechanical properties over conventional aluminium alloys (AA 2024-T3). The second part argued that glass/epoxy layers aligned between relatively thin layers of aluminium alloys are best suited for designing leading edges. The outcomes of the present study shall help the design engineers make an accurate decision on the choice of fibre metal laminate against soft body impact loading conditions.

9.3 Limitations of the research and scope for the future work

As the aerospace industry is a fast-growing field, the studies on the development of better resistance materials for aircraft have high demand. The aircrafts always fly with the risk of impacting foreign bodies such as birds. However, little research has been done on the effect of soft bodies on materials used in aircraft structures.

All researchers depend on Wilbeck's 45-year-old experiment test data for validation, which has many limitations. Some research laboratories have conducted experimental tests later, but it is not available to the public. Hence, it is recommended to

conduct a physical test by considering the factors developed by worldwide researchers, and it should be available to the researchers for future soft body impact analysis validations.

For composites, this study has utilized built-in Hashin two-dimensional failure criteria offered by ABAQUS to model the damage initiation in composites. The built-in failure criterion can be applied with continuum shell elements only. The study analysed only some of the available damage behaviours obtained from Hashin two-dimensional failure criteria. For observing through the thickness stress variations in impact a three-dimensional failure model with solid continuum elements is essential. Hence, a material model that consider the effect of out of plane loading conditions by using 3-D stress state is required. This material model is essential to accurately capture the damage behaviour of the composites when subjected to out of plane loads occurring in impact. The ABAQUS/ Explicit provides the facility of VUMAT subroutine through which the user can incorporate material models. It proposes to conduct soft body impact analysis on the fibre metal laminates using three-dimensional failure model with solid continuum elements. VUMAT subroutine also provides the options to read failure and delamination of each layer of the FML separately from the ABAQUS output check card.

Owing to computational limitations, the analysis has been conducted only in standard test specimens. It proposes to develop a full-scale leading-edge model with proposed GLARE laminate. Then, perform soft impact simulation to study its energy absorption characteristics

Appendix-I

Python scripting algorithm

Generated python code for elastic modulus variation

A 1.1 Python Code

- ##
  #
- # parametric study of impact with an elastic modulus with constant #
- # strain hardening modulus, hardening exponent, static yield limit and Poisson's ratio #
- # parameters used in the parametric study: #
- # strain hardening modulus: strain hardening modulus of wing #
- # static yield limit: static yield limit of wing
- # elastic modulus: elastic modulus of wing #
- # hardening exponent: hardening exponent of wing #
- # Poisson's ratio: Poisson's ratio of wing #
- ##
  ###
- # create the study

- wing = parStudy(par=(‘elastic modulus', ‘strain hardening modulus, ‘hardening exponent', ' static yield limit, ‘Poisons ratio’), directory=ON, verbose=ON)
- # DEFINE THE NAMES OF THE INPUT DECKS
- Input Files=('wing')
- # define the parameters
- wing.define(DISCRETE, par='elastic modulus', domain=(40000,50000,60000,70000,80000)
- wing.define(DISCRETE, par=' strain hardening modulus', domain=(426))
- wing.define(DISCRETE, par='hardening exponent', domain=(0.34))
- wing.define(DISCRETE, par=' static yield limit', domain=(265))
- wing.define(DISCRETE, par='Poisson’s ratio', domain=(0.33))
- # sample each parameter
- wing.sample(NUMBER, par='elastic modulus', number=5)
- wing.sample(NUMBER, par=' strain hardening modulus', number=1)
- wing.sample(INTERVAL, par='hardening exponent', interval=1)
- wing.sample(INTERVAL, par=' static yield limit', interval=1)
- wing.sample(INTERVAL, par='Poisson’s ratio', interval=1)
- # combine the samples into design points
- wing.combine(MESH)
- # generate analysis job data
- wing.generate(template='wing_discr')
- # execute all runs sequentially
- wing.execute(ALL)

- # parametric study output at end of step 1
- wing.output(step=1, file=ODB)
- # gather reation force results at node 3045
- wing.gather(results='o N3045_RF', variable='RF', node=3045)
- # screen report of RF2 rf results at node 3045
- wing.report(PRINT,par=('elastic modulus'),
- results=('o N3045_RF.2'), truncation=OFF)
- # for QA purposes
- wing.report(FILE, par=(),
- file='wing_discr.psr',
- results=('N3045_RF.2'))
- wing.report(FILE, par=(),
- file='wing_discr.psr',
- results=('o N3045_RF.2'))

Appendix-II

Practical applications

The present research discloses a method for designing aluminium alloy for a particular application and loading requirements to reduce research cost and time. The optimized 2xxx series aluminium alloy outperforms its 2024 alloy counterpart when used in leading edges of the wing and empennage structures skin materials —optimizing its material parameters against bird impact. The minimum weight and strength to weight ratio are the primary considerations in the material selection of aircraft wing leading edges. So, it is essential to improve the energy absorption ability of the material by reducing the materials involved in energy absorption. The design requirements of the leading edges are based on the critical loading condition, which is considered to be due to bird strikes. The study explains how to increase bird strike resistance to reduce the impact force, thereby increasing the energy absorption capability of the material. The main composition of the 2xxx series alloy is aluminium-copper and magnesium. The optimized material parameters can be attained through alloy compositions and controlled thermomechanical processing. The elastic stress parameter values can optimize through alloying in the fabrication. Other flow stress parameters can be optimized and controlled through thermomechanical processing. The addition of alloying elements is controlled so that the solid solubility limit for these contents in aluminium is not exceeded. The hardening adversely affects the energy absorbing capability of the material. So, in fabrication, careful attention must be provided to avoid any excess solute that puts up a second phase content of the material. Improvement in tensile strength properties and tensile toughness (deformation energy) improves the energy absorption, thereby reducing impact force.

List of References

Airoldi, A., and Cacchione, B. (2006). "Modelling of impact forces and pressures in Lagrangian bird strike analyses." *International Journal of Impact Engineering*, 32(10), 1651–1677.

Alderliesten, R. C., Hagenbeek, M., Homan, J. J., Hooijmeijer, P. A., de Vries, T. J., and Vermeeren, C. A. (2003). "Fatigue and Damage Tolerance of Glare." *Applied Composite Materials*, 10(4/5), 223–242.

Allan, J. (2006). "A heuristic risk assessment technique for Bird strike Management at airports." *Risk Analysis*, 26(3), 723–729.

Asundi, A., and Choi, A. Y. N. (1997). "Fiber Metal Laminates: An advanced material for future aircraft." *Journal of Materials Processing Technology*, 63(1-3), 384–394.

Benzeggagh, M. L., and Kenane, M. (1999). "Measurement of mixed-mode delamination fracture toughness of unidirectional glass/epoxy composites with mixed-mode bending apparatus." *Composites Science and Technology,* 56,439-449.

Botelho, E. C., Silva, R. A., Pardini, L. C., and Rezende, M. C. (2006). "A review on the development and properties of continuous fibre/epoxy/aluminum hybrid composites for aircraft structures." *Materials Research*, 9(3), 247–256.

Børvik, T., Hopperstad, O. S., Berstad, T., and Langseth, M. (2001). "A computational model of viscoplasticity and ductile damage for impact and penetration." European Journal of Mechanics - A/Solids, 20(5), 685–712.

Campilho, R., Moura, D., Gonçalves, D., Silva, J. F., Banea, M., and Silva, L. (2013). "Fracture toughness determination of adhesive and co-cured joints in natural fibre composites." *Composites Part B Engineering,* 50,120–126.

CASSENTI, B. (1979). "Hugoniot pressure loading in soft body impacts of aircraft." *20th Structures, Structural Dynamics, and Materials Conference*.

Chizari, M., Barrett, L. M., and Al-Hassani, S. T. S. (2008). "An explicit numerical modelling of the Water Jet Tube Forming." *Computational Materials Science*, 45,378–384.

Chowan, K. C. (2006). “Finite element analysis of bird strike on composite glass panels”, National University of Singapore.

Datta, S., Bandyopadhyay, A., and Pal, P. K. (2007). “Slag recycling in submerged arc welding and its influence on weld quality leading to parametric optimization.” *The International Journal of Advanced Manufacturing Technology*, 39(3-4), 229–238.

Davila, C., Camanho, P., and de Moura, M. (2001). “Mixed-mode decohesion elements for analyses of progressive delamination.” *19th AIAA Applied Aerodynamics Conference*.

Di Caprio, F., Cristillo, D., Saputo, S., Guida, M., and Riccio, A. (2019). “Crashworthiness of wing leading edges under bird impact event.” *Composite Structures*, 216, 39–52.

Dursun, T., and Soutis, C. (2014). “Recent developments in Advanced Aircraft Aluminium Alloys.” *Materials & Design,*56,862-871.

Ehrstroem, J. C., and Warner, T. (2000). “Metallurgical design of alloys for aerospace structures. “Materials Science Forum, Vols 331-337 (2000) pp 5-16 © (2000) Trans Tech Publications, Switzerland

Eschenfelder, P. F. (2005). “High Speed Flight at Low Altitude: Hazard to Commercial Aviation.” *International Bird Strike Committee Rept*. IBSC 27/WP I-3.

Fan, J., Guan, Z. W., and Cantwell, W. J. (2011). “Numerical modelling of perforation failure in fibre metal laminates subjected to low velocity impact loading.” *Composite Structures*, 93(9), 2430–2436.

Fatt, M. S., Lin, C., Revilock, D., and Hopkins, D. (2003). “Ballistic impact of Glare™ Fiber–Metal Laminates” *Composite Structures*,61,73-88.

Federal Aviation Administration (FAA). (2021). “Some significant wild life strikes to civil aircraft in the United States.” *Wildlife hazard mitigation*, FAA wild strike database and US department of Agriculture, <https://www.faa.gov/airports/airport_safety/wildlife/> (Apr. 5, 2022).

Federal Aviation Administration. (FAA). 2017 “Wildlife strikes to civil aircraft in the United States 1990–2017.” *FAA Wildlife Strike Database*, <https://wildlife.faa.gov/> (Apr. 5, 2022).

Georgiadis, S., Gunnion, A. J., Thomson, R. S., and Cartwright, B. K. (2008). “Bird-strike simulation for certification of the Boeing 787 composite moveable trailing edge.” *Composite Structures*, 86(1-3), 258–268.

Gingold, R. A., and Monaghan, J. J. (1977). “Smoothed particle hydrodynamics: Theory and application to non-spherical stars.” *Monthly Notices of the Royal Astronomical Society*, 181(3), 375–389.

Gouskov, A., Nikolaev, S., Kuts, V., Nizametdinov, F., Korovaitseva, E., and Yuan, S. (2017). “Analysis of displacement fields of particle shaping surface during nanoscale ductile mode cutting of Brittle Materials.” *The International Journal of Advanced Manufacturing Technology*, 95(5-8), 1911–1918.

Groenenboom, P. H. L. (1997). “Numerical simulation of 2D and 3D hypervelocity impact using the SPH option in Pam-Shock™.” *International Journal of Impact Engineering*, 20(1-5), 309–323.

Guida, M., Marulo, F., Polito, T., Meo, M., and Riccio, M. (2009). “Design and testing of a fibre-metal-laminate bird-strike-resistant leading edge.” *Journal of Aircraft*, 46(6), 2121–2129.

Gunnink, J., Vlot, A., Vries, T. J. de, and Hoeven, W. van der. (2022). “Glare Technology Development 1997–2000”. *Applied Composite Materials,* 9, 201–219.

Haq, A. N., Marimuthu, P., and Jeyapaul, R. (2007). “Multi response optimization of machining parameters of drilling al/sic metal matrix composite using Grey Relational Analysis in the Taguchi Method.” *The International Journal of Advanced Manufacturing Technology*, 37(3-4), 250–255.

Hashin, Z. (1980). “Failure criteria for unidirectional fibre composites.” *Journal of Applied Mechanics*, 47(2), 329–334.

Hashin, Z., and Rotem, A. (1973). “A fatigue failure criterion for fibre reinforced materials.” *Journal of Composite Materials*, 7(4), 448–464.

Hedayati, R., and Sadighi, M. (2016). “Effect of using an inner plate between two faces of a sandwich structure in resistance to bird-strike impact.” *Journal of Aerospace Engineering*, 29(1): 04015020.

Heimbs, S. (2011). “Computational methods for bird strike simulations: A Review.” *Computers & Structures*, 89(23-24), 2093–2112.

Hillerborg, A. (1985). “The theoretical basis of a method to determine the fracture energy of concrete.” *Materials and Structures*, 18(4), 291–296.

Hou, J. P., and Ruiz, C. (2007). “Soft body impact on laminated composite materials.” *Composites Part A: Applied Science and Manufacturing*, 38(2), 505–515.

Hou, N., Li, Y., and Liu, J. (2019). “Numerical simulation of bird impact on hollow blades of Titanium Fan Assembly.” *Journal of Aerospace Engineering*, 32(4), 04019044.

Iannucci, L. (2000). “Woven composite design for extreme events using a damage mechanics methodology.” *Proceedings of the Institution of Mechanical Engineers, Part L: Journal of Materials: Design and Applications*, 214(2), 99–111.

Ijaz, H., Zain-ul-abdein, M., Saleem, W., Asad, M., and Mabrouki, T. (2017). “Modified Johnson-cook plasticity model with damage evolution: Application to turning simulation of 2xxx Aluminium Alloy.” *Journal of Mechanics*, 33(6), 777–788.

Iqbal, M. A., Tiwari, G., Gupta, P. K., and Bhargava, P. (2015). “Ballistic performance and energy absorption characteristics of thin aluminium plates.” *International Journal of Impact Engineering*, 77, 1–15.

Jenq, S. T., Hsiao, F. B., Lin, I. C., Zimcik, D. G., and Ensan, M. N. (2007). “Simulation of a rigid plate hit by a cylindrical hemi-spherical tip-ended soft impactor.” *Computational Materials Science*, 39(3), 518–526.

Johnson, A. F., and Holzapfel, M. (2003). “Modelling soft body impact on composite structures.” *Composite Structures*, 61,103-113

Johnson, G. R., and Cook, W. 1983. “A constitutive model and data for metals subjected to large strains, high strain rates and high temperatures:” *Seventh International Symposium on Ballistics, The Hague, The Netherlands.*

Kamoulakos,A and Groenenboom P H L(1998). “Moving from FE to SPH for Space Debris Impact Simulations Experience with PAMSHOCK”, in *Proceedings of European Conference on Spacecraft Structures: Materials and Mechanical Testing*, Braunschweig, Germany

Kavitha mol, S., and Stanley, C. S. 2011. “Parametric studies on bird impact behavior of aircraft leading edges.” *nalir*, <https://nal-ir.nal.res.in/10488/> (Apr. 5, 2022).

Kermanidis, T., Labeas, G., Sunaric, M., and Ubels, L. (2005). “Development and validation of a novel bird strike resistant composite leading edge structure.” *Applied Composite Materials*, 12(6), 327–353.

Khan, S. H., and Sharma, A. P. (2020). “Influence of metal/composite interface on the damage behavior and energy absorption mechanisms of FMLS against projectile impact.” *Defence Technology*, 18(3), 441–456.

Khadyko, M., Myhr, O. R., and Hopperstad, O. S. (2019). “Work hardening and plastic anisotropy of naturally and artificially aged aluminium alloy AA6063.” Mechanics of Materials, 136, 103069.

Koohbor, B., Mallon, S., Kidane, A., and Sutton, M. A. (2014). “A DIC-based study of in-plane mechanical response and fracture of orthotropic carbon fiber reinforced composite.” *Composites Part B: Engineering*, 66, 388–399

Kumar Sahoo, A., and Sahoo, B. (2013). “Performance studies of multilayer hard surface coatings (tin/ticn/al2o3/tin) of indexable carbide inserts in hard machining: Part-II (RSM, grey relational and techno economical approach).” *Measurement*, 46(8), 2868–2884.

Lavoie, M. A., Gakwaya, A., Ensan, M. N., Zimcik, D. G., and Nandlall, D. (2009). “Bird's substitute tests results and evaluation of available Numerical Methods.” *International Journal of Impact Engineering*, 36(10-11), 1276–1287.

Lapczyk, I., and Hurtado, J. A. (2007). “Progressive damage modeling in fibre-reinforced materials.” *Composites Part A: Applied Science and Manufacturing,* 38(11),2333–2341.

Leseur, D. (1999). “Experimental investigations of material models for TI-6A1-4V and 2024-T3.”

Li, J., Lou, Y., Chai, X., Ma, Z., and Jin, X. (2021). “Numerical simulation of bird strike on jet engine considering bird ingestion requirements.” *Journal of Aircraft*, 1–13.

Liu, J., Li, Y., Shi, X., and Wang, W. (2014). “Dynamic response of bird strike on aluminum honeycomb-based sandwich panels.” *Journal of Aerospace Engineering*, 27(3), 520–528.

Lucy, L. B. (1977). “A numerical approach to the testing of the fission hypothesis.” *The Astronomical Journal*, 82, 1013.

Majzoobi, G. H., and Dehgolan, F. R. (2011). “Determination of the constants of Damage Models.” Procedia Engineering, 10, 764–773.

Mao, R. H., Meguid, S. A., and Ng, T. Y. (2008). “Transient three-dimensional finite element analysis of a bird striking a fan blade.” *International Journal of Mechanics and Materials in Design*, 4(1), 79–96.

Marulo, F., and Guida, M. (2014). “Design criteria for bird strike damage on windshield.” *Advances in aircraft and spacecraft science*, 1(2), 233–251.

McCarthy, M. A., Xiao, J. R., Petrinic, N., Kamoulakos, A., and Melito, V. (2004). “Modelling of bird strike on an aircraft wing leading edge made from fibre metal laminates – part 1: Material modelling.” *Applied Composite Materials*, 11(5), 295–315.

McCarthy, M. A., Xiao, J. R., McCarthy, C. T., Kamoulakos, A., Ramos, J., Gallard, J. P., and Melito, V. (2004). "Modelling of bird strike on an aircraft wing leading edge made from fibre metal laminates – part 2: Modelling of impact with SPH bird model." *Applied Composite Materials*, 11(5), 317–340.

McNaughtan, I. I. (1972). "The design of leading edge and intake wall structure to resist bird impact." *Royal Aircraft Establishment, Technical report 72056.*

Meguid, S. A., Mao, R. H., and Ng, T. Y. (2007). "Fe analysis of geometry effects of an artificial bird striking an aeroengine fan blade." *International Journal of Impact Engineering*, 35(6), 487–498.

Miller, G. H., and Puckett, E. G. (1996). "A high-order Godunov method for multiple condensed phases." *Journal of Computational Physics*, 128(1), 134–164.

Monaghan, J.J, (1992), "Smoothed Particle Hydrodynamics", *Annual Review of Astronomy and Astrophysics*,30,543–574.

Nguyen, M. Q., Elder, D. J., Bayandor, J., Thomson, R. S., and Scott, M. L. (2005). "A review of explicit finite element software for composite impact analysis." *Journal of Composite Materials*, 39(4), 375–386.

Nishikawa, M., Hemmi, K., and Takeda, N. (2011). "Finite-element simulation for modeling composite plates subjected to soft-body, high-velocity impact for application to bird-strike problem of composite fan blades." *Composite Structures*, 93(5), 1416–1423.

Nizampatnam, L., and Horn, W. (2008). "Investigation of equation of state models for predicting bird impact loads." *46th AIAA Aerospace Sciences Meeting and Exhibit*.

Dede,O. and Altan, K. (2015) "Investigation of effects of bird strike on wing leading edge by using explicit finite element method." *8th Ankara international conference*, Ankara, Turkey.

Orlando, S., Marulo, F., Guida, M., and Timbrato, F. (2017). "Bird strike assessment for a composite wing flap." *International Journal of Crashworthiness*, 23(2), 219–235.

Pahange, H., and Abolbashari, M. H. (2016). "Mass and performance optimization of an airplane wing leading edge structure against bird strike using Taguchi-based Grey Relational Analysis." *Chinese Journal of Aeronautics*, 29(4), 934–944.

Pantelakis, S. G., and Alexopoulos, N. D. (2006). "Assessment of the ability of conventional and advanced wrought aluminum alloys for mechanical performance in light-weight applications." *Materials & Design*, 29,80–91.

Qiu, J., Wang, D., Liu, C., Chen, L., Huang, H., and Sun, Q. (2020). “Dynamic response of bird strike on honeycomb-based sandwich panels of composite leading edge.” *International Journal of Crashworthiness*, 26(4), 424–437.

Reglero, J. A., Rodríguez-Pérez, M. A., Solórzano, E., and de Saja, J. A. (2011). “Aluminium foams as a filler for leading edges: Improvements in the mechanical behaviour under Bird Strike Impact tests.” *Materials & Design*, 32(2), 907–910.

Sadighi, M., Alderliesten, R. C., and Benedictus, R. (2012). “Impact resistance of fibre-metal laminates: A Review.” *International Journal of Impact Engineering*, 49, 77–90.

Sadighi, M., Pärnänen, T., Alderliesten, R. C., Sayeaftabi, M., and Benedictus, R. (2011). “Experimental and numerical investigation of metal type and thickness effects on the impact resistance of fiber metal laminates.” *Applied Composite Materials*, 19(3-4), 545–559.

Salehi, H., Ziaei-Rad, S., and Vaziri-Zanjani, M. A. (2010). “Bird impact effects on different types of aircraft bubble windows using numerical and experimental methods.” *International Journal of Crashworthiness*, 15(1), 93–106.

Scalici, T., Fiore, V., Orlando, G., and Valenza, A. (2015). “A DIC-based study of flexural behaviour of roving/mat/roving pultruded composites.” *Composite Structures*, 131, 82–89.

Seidt, J., and Gilat, A. (2013). “Plastic deformation of 2024-T351 aluminum plate over a wide range of loading conditions” *International Journal of Solids Structures,* 50,1781–1790.

Seo, H., Hundley, J., Hahn, H. T., and Yang, J.-M. (2010). “Numerical simulation of glass-fibre-reinforced aluminum laminates with diverse impact damage.” *AIAA Journal*, 48(3), 676–687.

Sharma, A. P., Khan, S. H., and Parameswaran, V. (2017). “Experimental and numerical investigation on the uni-axial tensile response and failure of fibre metal laminates.” *Composites Part B: Engineering*, 125, 259–274.

Sharma, A. P., and Khan, S. H. (2018). “Influence of metal layer distribution on the projectiles impact response of glass fibre reinforced aluminium laminates.” *Polymer Testing*, 70, 320–347.

Shi, Y., Pinna, C., and Soutis, C. (2014). “Modelling impact damage in composite laminates: A simulation of intra- and inter-laminar cracking.” *Composite Structures*, 114, 10–19.

Shyue, K.-M. ((2001). “A Fluid-Mixture Type Algorithm for Compressible Multicomponent Flow with Mie–Gruneisen Equation of State” *Journal of Computational Physics* 171,678–707

Sinha, S. K. 2021. “Transient vibratory response of turbofan engine rotor impacted by Bird Strike.” *Journal of Aerospace Engineering*, 34(4), 04021027.

Sınmazçelik, T., Avcu, E., Bora, M., and Çoban, O. (1970). “A review fibre metal laminates background bonding types and applied test methods.” *Materials &Design*, 32(7),3671–85.

Smojver, I., and Ivancevic, D. (2011). “Bird strike damage analysis in aircraft structures using ABAQUS /Explicit and coupled Eulerian Lagrangian approach” *Composites Science and Technology*, 71, 489–498.

Smojver, I., and Ivančević, D. (2010). “Numerical simulation of bird strike damage prediction in airplane flap structure.” *Composite Structures*, 92(9), 2016–2026.

Stanley, C. S., Kotresh, G. M., Gowda, M. N. N., and Ramesh, S.(2011). “Design and testing of wing leading edge of a light transport aircraft.” *NASAS*.

Starke, E. A., and Staley, J. T. (1999). “Application of modern aluminum alloys to aircraft.” *Progress in Aerospace Sciences*, 32,131–72.

Steinberg, D. J. (1987). “Spherical explosions and the equation of state of water.” Report No. UCID-20974, Lawrence Livermore National Laboratory, Livermore, CA. <https://www.osti.gov/servlets/purl/6766676> (Apr. 13, 2022).

Stoker, H.C. (1999). “Development of the Arbitrary Lagrangian-Eulerian method in nonlinear solid mechanics”. HC Stoker Enschedel, The Netherlands.

Stoll, F., Brockman, R., Stoll, F., and Brockman, R. (1997). “Finite element simulation of high-speed soft-body impacts.” *38th Structures, Structural Dynamics, and Materials Conference*.

Tho, C.-H., and Smith, M. R. (2011). “Accurate bird strike simulation methodology for ba609 tiltrotor.” *Journal of the American Helicopter Society*, 56(1), 12007–1200710.

Ubels, L. C., Johnson, A., Gallard, J., and Sunaric, M. (2003). “Design and testing of a composite bird strike resistant leading edge” *National Aerospace Laboratory, NLR*, 1-15

Vilamosa, V., Børvik, T., Hopperstad, O. S., and Clausen, A. H. (2015). “Behaviour and modelling of aluminium alloy AA6060 subjected to a wide range of strain rates and temperatures.” EPJ Web of Conferences, 94, 04018.

Vlot, A. (1996). “Impact loading on fibre metal laminates.” *International Journal of Impact Engineering*, 18(3), 291–307.

Vlot, A., and Gunnink, J. W. (2001). “Fibre Metal Laminates: An introduction.” ,Kluwer Academic Publishers.

Wang, F. S., and Yue, Z. F. (2010). “Numerical simulation of damage and failure in aircraft windshield structure against Bird Strike.” *Materials & Design*, 31(2), 687–695.

Wang, J. G., Sun, W., and Anand, S. (2009). “Numerical investigation on active isolation of ground shock by soft porous layers.” *Journal of Sound and Vibration*, 321(3-5), 492–509.

Wilbeck, J. S. (1977). “Impact behavior of low strength projectiles.” Rep.No. AFML-TR-77-34, Air Force Materials Laboratory, Air Force Wright Aeronautical Laboratory, Wright-Patterson Air Force Base, OH.

Wu, G., and Yang, J.-M. (2005). “Analytical modelling and numerical simulation of the nonlinear deformation of hybrid fibre–metal laminates.” *Modelling and Simulation in Materials Science and Engineering*, 13(3), 413–425.

Wu, Z., Zong, Z., and Sun, L. (2014). “A Mie-Grüneisen mixture Eulerian model for underwater explosion.” *Engineering Computations*, 31(3), 425–452.

Yu, Z., Xue, P., Yao, P., and Zahran, M. S. 2020. “Novel design of Wing Leading edge against Bird strike.” *Journal of Aerospace Engineering*, 33(3):04020009.

Zakir, S. M., and Li, Y. (2012). “Dynamic response of the leading edge wing under Soft body impact.” *International Journal of Crashworthiness*, 17(4), 357–376.

Zhu, S., and Chai, G. B. (2012). “Low-velocity impact response of fibre–metal laminates – experimental and finite element analysis.” *Composites Science and Technology*, 72(15), 1793–1802.

List of Publications

Peer reviewed journals

1. Kavitha Mol, S., and Sadiq, A. (2020) "Material parametric optimisation of wing leading edge profile against soft body impact", International Journal of Crashworthiness, 27:3, 677-687, Taylor and Francis. DOI: 10.1080/13588265.2020.1836841(SCI indexed) (impact factor 2.105)
2. Kavitha Mol, S., Stanley, C. S., and Sadiq, A. (2022) "Crashworthiness enhancement of aluminum alloy used for leading edges of wing and empennage structures", The journal of Aerospace engineering, American Society of Civil Engineers (ASCE Library). 10.1061/(ASCE)AS.1943-5525.0001477. (SCI indexed) (impact factor 2.055)
3. Kavitha Mol, S., and Sadiq, A. (2022) "Performance improvement studies of the aluminum alloy plate with optimized properties under soft body impact loading". SSRN. Elsevier. http://dx.doi.org/10.2139/ssrn.4057865.
4. Kavitha Mol, S., and Sadiq, A. (2022) "Influence of metal thickness and stacking sequences on soft body impact response and damage behaviour of GLARE laminates" International Journal of Impact engineering, Elsevier. (Revision submitted) (SCI indexed) (impact factor 4.592)
5. Kavitha Mol, S., and Sadiq, A. (2022) "Numerical simulation of the soft body impact with the different equation of state material models and finite element approaches", Proceedings of the Institution of Mechanical Engineers, Part G: Journal of Aerospace Engineering, Sage publications. (Revision to be submitted) (SCI indexed) (impact factor 1.283)
6. Kavitha Mol, S., and Sadiq, A. (2022) "Investigation to improve the mechanical properties of fibre metal laminates for wing leading edges", Thin-walled structures, Elsevier (Revision to be submitted) (SCI indexed) (impact factor 5.83)

Conferences

1. Kavitha Mol, S., and Sadiq, A. (2020) “Different Numerical Simulation Approaches for Soft Body Impact on Aircraft Structures”, *Proceedings of the10th International Conference on Recent Engineering and Technology*, 21st June 2020, Bangalore, India, ISBN 978-93-5406-579-8
2. Kavitha Mol, S., and Sadiq, A. (2021) “Performance improvement studies on aluminium alloy plate with optimized properties under soft body impact loading”, *Proceedings of the10th International Conference on Aerospace and Mechanical Engineering*, December 16-18 2021, Kerala, India